
THERMOMETRY OF ${}^9\text{Be}^+$ IONS
IN A CRYOGENIC PENNING TRAP

Von der QUEST-Leibniz-Forschungsschule
der Gottfried Wilhelm Leibniz Universität Hannover

zur Erlangung des akademischen Grades

Doktor der Naturwissenschaften
- Dr. rer. nat. -

genehmigte Dissertation von

Johannes Mielke, M.Sc.

2021

- 1. Gutachter:** Prof. Dr. Christian Ospelkaus
Institut für Quantenoptik
Leibniz Universität Hannover
 - 2. Gutachter:** Prof. Dr. Carsten Klempt
Institut für Quantenoptik
Leibniz Universität Hannover
 - 3. Gutachter:** Prof. Richard Charles Thompson MA DPhil
Imperial College London
- Tag der Promotion:** 07.10.2021

Abstract

High precision comparisons of the proton and antiproton g -factor enable stringent tests of CPT symmetry in the baryonic sector. However, current measurement routines suffer from long preparation times and high particle temperatures, which complicate the increase of the precision beyond the parts per billion regime. As a solution, new sympathetic cooling schemes based on co-trapped laser-cooled ions may be used to cool (anti-)protons to the ground state of motion and to significantly decrease particle preparation times. In addition, motional coupling to an auxiliary ion in a double-well potential can be used for the implementation of new readout schemes based on quantum logic spectroscopy for the spin-state of the (anti-)protons.

This thesis describes a cryogenic Penning trap system for ground state cooling of single ${}^9\text{Be}^+$ ions, which represents the latest development of the BASE experiment in Hannover towards the implementation of sympathetic cooling schemes and quantum logic spectroscopy of single (anti-)protons. Furthermore, the setup and implementation of lasers systems at 313 nm for Doppler cooling, repumping and Raman interactions are described. To this end, an optical platform for laser beam delivery to the vacuum system and an optical phase-locked loop for the stabilization of the relative phase of two lasers at 313 nm are presented.

In this work, the laser systems are used for measurements of the optical resonance frequencies for cooling, probing and repumping of ${}^9\text{Be}^+$ ions. In addition, stimulated Raman transitions are demonstrated using two phase-locked lasers at 313 nm. In the following, this technique is used for high-precision measurements of the qubit frequency and the magnetic field, as well as thermometry measurements with ${}^9\text{Be}^+$ ions. The temperature of the ions after Doppler cooling is measured as a function of the cooling laser parameters and a minimal axial mode temperature of 1.77(10) mK is obtained.

The results of this thesis pave the way for sideband spectroscopy and ground state cooling of single ${}^9\text{Be}^+$ ions in Penning traps, which is an essential prerequisite for sympathetic ground state cooling of single (anti-)protons and the application of quantum logic spectroscopy to (anti-)proton g -factor measurements in the future.

Keywords: Penning traps, laser cooling, stimulated Raman transitions

Contents

1	Introduction	1
1.1	Outline	4
2	Theoretical principles	5
2.1	Single particles in Penning traps	5
2.1.1	The ideal Penning trap	5
2.1.2	Cylindrical Penning traps with open-endcap electrodes	7
2.2	Ion plasmas and Coulomb crystals	10
2.3	Doppler cooling in Penning traps	11
2.4	Motional sideband spectroscopy	14
3	Overview of the experimental setup	17
3.1	The beryllium ion	17
3.1.1	Electronic level structure	18
3.2	Penning trap stack	19
3.2.1	The beryllium trap	21
3.2.2	Other traps	22
3.3	Cryo-mechanical setup	22
3.4	Optical Subsystems	24
3.4.1	Ablation laser	24
3.4.2	UV laser systems	25
3.4.3	Laser beam delivery platform	29
3.4.4	Phase-lock for the Raman laser system	32
3.4.5	Imaging and detection system	37
3.5	Experiment control	38
4	Particle preparation	41
4.1	Loading procedure	41
4.2	Particle ejection	43
4.3	Cleaning methods	46
4.4	Measurement of the trap frequencies	47
5	Measurements of optical resonance frequencies	53
5.1	The cooling transition	53

5.2	Double-resonance measurements	55
5.3	Triple-resonance measurements	60
5.4	Summary of the measured transition frequencies	62
6	Stimulated Raman transitions and thermometry of $^9\text{Be}^+$	65
6.1	Measurements with co-propagating Raman laser beams	65
6.1.1	Qubit frequency	66
6.1.2	Coherence time	67
6.1.3	Conclusion for the magnetic field	69
6.2	Measurements with crossed Raman laser beams	69
6.2.1	Axial thermometry measurements	70
6.2.2	Influence of the cooling laser parameters	71
7	Summary and Outlook	73
7.1	Summary	73
7.2	Outlook	74
7.2.1	Measurements with single ions	74
7.2.2	Sideband spectroscopy and ground state cooling of $^9\text{Be}^+$	75
7.2.3	Sympathetic cooling of protons	76
7.2.4	Quantum logic spectroscopy with protons	77
7.2.5	Measurement of the proton g -factor	77
A	Calculation of the transition frequencies	79
B	Rendered image of the experimental setup	83
C	Recipe for UV fiber production	85
	Bibliography	87

CHAPTER 1

Introduction

The Standard Model of particle physics is today's theoretical framework for the description of all known elementary particles and the fundamental interactions between them. These are electromagnetism, the weak interaction and the strong interaction. Its great success is based on the large number of successful predictions and explanations of a wide range of experimental data based on its fundamental principles.

Still, the Standard Model remains incomplete. On the one hand, it does not include a unified description of gravity. On the other hand, it lacks explanations for phenomena such as dark matter and dark energy as well as the imbalance of baryonic and antibaryonic matter in the observable universe [1, 2]. This contradiction between the success of the past and the unsolved problems of the present motivates the search for physics beyond the Standard Model. As part of this search, high-precision experiments looking for violations of the so-called charge-parity-time (CPT) symmetry have emerged in recent decades.

Within local Lorentz-invariant quantum field theories such as the Standard Model, CPT symmetry is a fundamental property that requires physics to remain unchanged under the simultaneous application of charge conjugation, parity inversion and time reversal [3]. As a consequence, intrinsic properties of particles and antiparticles such as their mass, lifetime, charge and magnetic moment must be equal in magnitude and, in case of the charge and magnetic moment, their sign must be flipped [4]. Thus, high-precision comparisons of these properties allow for a stringent test of CPT symmetry. Examples are given in terms of comparisons of the electron and positron g -factor in the case of leptons [5] and measurements of the mass differences between the neutral kaon and antikaon in the case of mesons [6]. In the baryonic sector, in particular the Baryon Antibaryon Symmetry Experiment (BASE) collaboration [7] at CERN (the European Organization for Nuclear Research) has produced a number of groundbreaking results, including the high precision comparisons of the charge-to-mass-ratio of the proton and the antiproton [8] as well as high precision measurements of the proton and antiproton g -factor [9, 10].

The BASE collaboration's high-precision measurements with (anti-)protons are carried out in Penning traps. These devices provide a well-isolated environment

for charged particles with low disturbances and long storage times, as for example confirmed through the storage of a cloud of antiprotons for more than a year [11]. Sophisticated experimental techniques are key ingredients for the measurements. Especially in the case of (anti-)proton g -factor measurements, an important tool is the so-called double trap technique [12]. Here, the idea is to split the measurement procedure into different sequences which are carried out in dedicated traps. One sequence is carried out exclusively in the “precision trap”, which provides a highly homogeneous magnetic field, in which the motional frequencies of a trapped particle can be measured using cryogenic tank circuits for induced image charge detection [13]. The knowledge of these frequencies allows to determine the free cyclotron frequency ν_c with high precision. The other sequence is partly carried out in the “analysis trap”, which provides a magnetic field with a strong curvature. In this case, a spectroscopy pulse is applied to the particle in the precision trap and the spin-state is subsequently readout in the analysis trap using the continuous Stern-Gerlach effect [14]. With this procedure, the spin-flip probability and thus the particle’s Larmor frequency ν_L can be measured with high precision as well. The g -factor can then be determined via the relation

$$g = 2 \frac{\nu_L}{\nu_c}. \quad (1.1)$$

Using this technique, the BASE collaboration was able to measure the proton g -factor with a fractional precision of 0.3 parts per billion (ppb) [9] and the (anti-)proton g -factor with a fractional precision of 1.5 ppb [10]. However, no violation of CPT symmetry was observed so far.

Nevertheless, the efforts of the BASE collaboration continue with an ongoing strive for higher precision [15]. The struggle against particle temperature represents one of the biggest challenges of the future. This can be understood by looking at current readout schemes for the (anti-)proton’s spin state based on the continuous Stern-Gerlach effect, which rely on the coupling between the axial motion and the spin state. The coupling introduces a small shift to the axial frequency, which depends on the orientation of the spin and therefore can be used for state detection. However, at the same time additional shifts are introduced, which for example depend on the quantum state of the cyclotron motion [16]. Thus, it is necessary to discriminate shifts due to a change of the spin-state from shifts due a cyclotron quantum jump. Since the rate of the latter decreases with the particle’s temperature, cooling to low temperatures simplifies the readout of the spin.

As a consequence, current experiments are implementing elaborate preparation routines based on resistive cooling mediated through cryogenic tank-circuits and additional statistical routines for the measurement of the spin state [17]. With these techniques, the preparation of a particle takes several minutes and a single data point for a g -factor resonance measurement on average requires about an hour of measurement time [9]. Thus, speeding up the preparation and readout routines is the key to faster experiment cycle times, which in turn allow for improved statistics and reduced systematic errors.

A solution to this problem can be found in atomic physics. For decades, fast laser-based cooling and detection schemes [18] have been used for precision measurements, with atoms routinely cooled to the ground state of motion [19]. The proton, however, lacks optical transitions for laser cooling, and as a pure 2-level system, direct state detection via radiation is not possible.

An idea to overcome this limitation was proposed by Heinzen and Wineland in 1990, which today is known as quantum logic spectroscopy [20, 21]. In their method, a co-trapped “logic” ion with a suitable cooling transition is used for sympathetic cooling of the “spectroscopy” ion. In addition, the common motion of both particles is used as a quantum bus to transfer the spin state information from the spectroscopy ion to the logic ion, from which it can be read out using fluorescence detection. In recent years, quantum logic spectroscopy has been demonstrated in radio frequency (RF) traps with applications in ion clocks [22], precision spectroscopy of molecular ions [23, 24] and highly charged ions [25].

Although ground state cooling of single ions in Penning traps has been demonstrated in recent years as well [26, 27], the demonstration of quantum logic spectroscopy in Penning traps is still pending. Difficulties are caused by the comparatively low trap frequencies, more complex laser cooling schemes and the more difficult optical access in comparison with RF traps. For these reasons, concepts in the context of Penning traps were proposed first and foremost with only sympathetic cooling of the spectroscopy ion in mind. For example, it was proposed to enable the coupling of both ions via a common electrode [28, 29] and the feasibility of coupling through a common cryogenic resonator was recently demonstrated at the BASE experiment in Mainz [30]. These setups allow for sympathetic laser cooling of the respective spectroscopy ion to temperatures of a few mK and have the potential to speed up preparation routines in Penning traps significantly.

A variation of the concept of Heinzen and Wineland, also aimed at quantum logic spectroscopy, has been proposed by Wineland *et al.* in 1998 [31]. In order to allow for sympathetic ground state cooling of a particle, direct free space coupling of the logic and spectroscopy ion in a double-well potential is envisioned. The feasibility of this technique was already demonstrated with identical ions in RF traps [32, 33].

The BASE experiment in Hannover was started in order to develop new methods for g -factor measurements within the BASE collaboration and in particular to show the viability of quantum logic spectroscopy of (anti-)protons in Penning traps [34]. To this end, the experiment aims for the implementation of sympathetic laser cooling of (anti-)protons using single ${}^9\text{Be}^+$ ions co-trapped in an engineered double-well potential, following the Wineland proposal from 1998. The double-well potential will be generated with a micro-fabricated Penning trap [35]. Ground state cooling could be implemented using stimulated Raman transitions [36, 37] and a dedicated sideband trap [38] for the implementation of the required sideband pulses for the (anti-)proton will be implemented for quantum logic spectroscopy. Drastically reduced experiment cycle times are anticipated, which would to study potential sidereal oscillations of the measured quantities [34].

In order to achieve these ambitious goals, BASE Hannover has designed and set up

an experimental apparatus with a Penning trap stack for step-by-step implementation of the required tools [39]. The latest achievements include the demonstration of production, trapping and Doppler cooling of beryllium ions [40] as well as fast adiabatic transport of particles along the trap stack [41]. In this thesis, the current setup was used for the first demonstration of stimulated Raman transitions and thermometry of ${}^9\text{Be}^+$ ions.

1.1 Outline

The outline of this thesis is as follows. In chapter 2 the **theoretical principles** of the concepts and techniques used in this work are introduced. In particular, the motion of single particles and particle ensembles in Penning traps as well as techniques for laser cooling and sideband spectroscopy are described. The **experimental setup** for the measurements is presented in chapter 3. Special attention is paid to the optical subsystems, which were developed during the course of this work, such as laser systems and the optical platform for beam delivery. Techniques for **particle preparation** are shown in chapter 4. In this context, concepts for loading and cleaning of the traps are introduced and precision measurements of the trap frequencies are presented. In chapter 5, the results of **measurements of optical resonance frequencies** are shown. To this end, more advanced measurement methods based on resonance measurements with multiple laser are introduced. Evidence for **stimulated Raman transitions and thermometry measurements with ${}^9\text{Be}^+$ ions** are presented in chapter 6. These measurements show the functionality of a new continuous wave (cw) Raman laser system and allow to measure the qubit frequency of the beryllium ions and the magnetic field with high precision. Finally, a **summary and outlook** is given in chapter 7, where the results of this thesis will be recapped and possibilities for future improvements and upgrades on the way towards sympathetic laser cooling and QLS of (anti-)protons are described.

CHAPTER 2

Theoretical principles

This chapter introduces the fundamental concepts and experimental techniques that will be used within this work. It starts with an overview of the motion of a single particle in a Penning trap, with special emphasis on the case of a cylindrical design (section 2.1). The concepts are extended in section 2.2 for the case of ion ensembles, such as ion plasmas and Coulomb crystals. Furthermore, Doppler cooling in the context of Penning traps is introduced (section 2.3). Finally, the chapter finishes with a section on sideband spectroscopy and its adaption for thermometry measurements within this thesis (section 2.4).

2.1 Single particles in Penning traps

Earnshaw's theorem states that trapping of charged particles is not possible using only electrostatic fields [42]. However, oscillating electric fields or a combination of electro- and magnetostatic fields can be used to generate a confining potential. A RF trap makes use of the first possibility, while a Penning trap is based on the second one. In the following, the basic concept of a Penning trap is introduced.

2.1.1 The ideal Penning trap

The motion of a single charged particle in an idealized Penning trap is derived in many textbooks and a detailed description is given for example in reference [43]. The following section summarizes the main ideas.

The Penning trap requires a quadrupole electric field \vec{E} , that confines the particle along one direction, which we assume to point along \vec{e}_z and to which we refer as the trap axis. In addition, a uniform magnetic field $\vec{B} = B\vec{e}_z$ is superimposed, which confines the particle in the directions perpendicular to this axis. Figure 2.1 shows a setup with hyperbolic electrodes, which can be used to generate the required electrostatic potential described by the equation

$$U = \frac{U_0}{d_0^2}(2z^2 - x^2 - y^2), \quad (2.1)$$

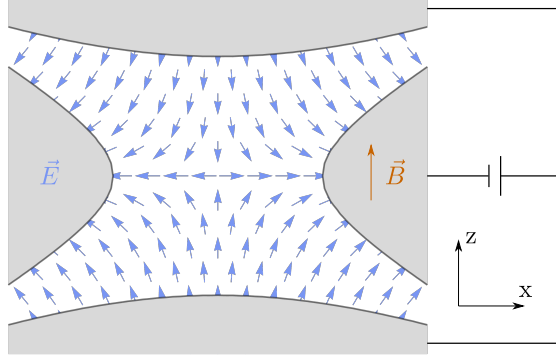


Figure 2.1: Cross-section of an ideal Penning trap consisting of one ring electrode and two endcap electrodes. The three-dimensional shape of the electrodes corresponds to a rotation of the surfaces around the trap axis \vec{e}_z . Both endcaps are connected to each other and a direct current (DC) potential is applied between the ring electrode and the endcaps. The hyperbolic shape of the electrodes produces a quadrupole electric field \vec{E} . A uniform magnetic field \vec{B} is added to confine the particles perpendicular to the trap axis.

where x , y and z are Cartesian coordinates, U_0 is the applied trap potential and d_0 is a characteristic parameter related to the trap dimensions. Due to the Lorentz force

$$\vec{F} = q\vec{E} + q\vec{v} \times \vec{B}, \quad (2.2)$$

this field configuration gives rise to the following set of differential equations,

$$\ddot{x} = \omega_c \dot{y} + \frac{\omega_z^2}{2} x; \quad \ddot{y} = -\omega_c \dot{x} + \frac{\omega_z^2}{2} y; \quad \ddot{z} = -\omega_z^2 z, \quad (2.3)$$

where we introduced two characteristic eigenfrequencies of the particle, namely the free cyclotron frequency ω_c and the axial frequency ω_z . The free cyclotron frequency is defined solely by the particle's charge-to-mass ratio q/m and the magnetic field,

$$\omega_c = \frac{q}{m} B, \quad (2.4)$$

and it is independent of the electric field. In contrast, the axial frequency is independent of the magnetic field and does only depend on the charge-to-mass ratio, the electrostatic potential and the characteristic size of the trap:

$$\omega_z = \sqrt{\frac{qU_0}{md_0^2}}. \quad (2.5)$$

We can see from equation 2.3 that the axial motion corresponds to a harmonic oscillation with frequency ω_z , which is independent of the motion in the other direc-

tions. On the other hand, the motions in the x - and y -directions are interconnected. By introducing the complex variable $u = x + iy$, this set of coupled differential equations can be combined to a single equation,

$$\ddot{u} - i\omega_c \dot{u} - \frac{\omega_z^2}{2}u = 0. \quad (2.6)$$

The solution of this radial equation of motion gives rise to two superimposed circular motions [44] with corresponding frequencies

$$\omega_+ = \frac{\omega_c}{2} + \sqrt{\frac{\omega_c^2}{4} - \omega_z^2} \quad (2.7)$$

and

$$\omega_- = \frac{\omega_c}{2} - \sqrt{\frac{\omega_c^2}{4} - \omega_z^2}. \quad (2.8)$$

We call them the modified cyclotron frequency ω_+ and the magnetron frequency ω_- . As they correspond to two circular motions in the x - y -plane, we also refer to them as the radial eigenfrequencies of the trapped particle. Typically, Penning traps are operated in a regime where the frequency hierarchy

$$\omega_- \ll \omega_z \ll \omega_+ \quad (2.9)$$

applies.

In practice, deviations from the ideal Penning trap geometry and thus deviations from the potential described by equation 2.1 can occur. In this case, we will still be able to observe the described oscillatory motions of the particle, but in general the frequency relations given by equations 2.7 and 2.8 are not valid any more. In the case of ellipticities of the electrostatic potential and/or a relative tilt with respect to the magnetic field, we can instead make use of the more robust equation

$$\omega_c^2 = \omega_+^2 + \omega_-^2 + \omega_z^2, \quad (2.10)$$

which is derived in reference [13]. It is called the ‘‘invariance theorem’’, because it describes the fact that imperfections can affect the individual trap frequencies, but leave the above equation unaffected. Still, certain effects such as an imperfect quadrupolar potential due to higher order multipole terms are not covered by this theorem and thus need to be taken into account in the design of a Penning trap.

2.1.2 Cylindrical Penning traps with open-endcap electrodes

In a real Penning trap it is necessary to use electrode geometries that differ from the ideal hyperbolic shape, as the trap electrodes must come with finite dimensions

and are subject to machining tolerances. In practice, many Penning traps come in a cylindrical design with open-endcap electrodes [45]. It simplifies the machining effort for the individual electrodes and allows for a better access of the trap center, which may be required for particle transport, laser access or fluorescence imaging.

In this design the electrodes are machined as rings with equal inner radius but different axial extent and are separated from each other by additional isolating spacers between them. It can be shown that, in order to compensate for the deviations from the ideal Penning trap geometry, additional ‘compensation electrodes’ can be introduced between the central ring electrode and the endcap, so that the potential shape can be optimized through careful tuning of the voltages applied to these electrodes [46].

All measurements presented in this thesis have been carried out in a cylindrical five-pole Penning trap, consisting of a central ring electrode, two neighboring compensation electrodes and two open-endcap electrodes. A sketch of the trap geometry is shown in figure 2.2. A detailed derivation of the trapping potential is described in reference [16] and is summarized here.

For Laplace’s equation in cylindrical coordinates (ρ, φ, z) [42],

$$\frac{\partial^2 \Phi}{\partial \rho^2} + \frac{1}{\rho} \frac{\partial \Phi}{\partial \rho} + \frac{1}{\rho^2} \frac{\partial^2 \Phi}{\partial \varphi^2} + \frac{\partial^2 \Phi}{\partial z^2} = 0, \quad (2.11)$$

we can find a solution based on a series expansion of the potential in Bessel functions and trigonometric functions, that harnesses the design’s inherent radial symmetries. Boundary conditions are thereby introduced through the voltages V_i applied to the

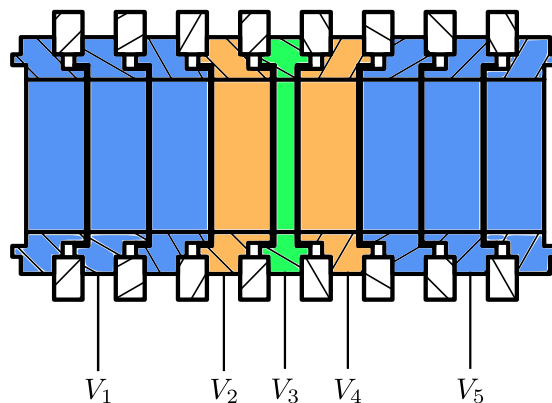


Figure 2.2: Cross-section of a cylindrical Penning trap with five electrodes. The figure shows the ring electrode (green), correction electrodes (orange), endcap electrodes (blue) and sapphire spacers (white). The endcaps are divided into three segments, which are advantageous for particle transport. For the generation of a static harmonic potential, the segments of the endcap are kept at the same voltage. The labels V_i denote the voltages that are applied to the respective electrodes. Figure taken from reference [41].

individual trap electrodes. For the five-pole Penning trap we obtain the solution

$$\begin{aligned} \Phi(\rho, z, V_i) = & \frac{2}{\Lambda} \sum_{n=1}^{\infty} \left[\frac{V_1 \cos(k_n z_0) - V_5 \cos(k_n \Lambda)}{k_n} \right. \\ & \left. + \sum_{i=2}^5 \frac{V_i - V_{i-1}}{k_n^2 d} (\sin(k_n z_{2i}) - \sin(k_n z_{2i-1})) \right] \\ & \times \frac{I_0(k_n \rho)}{I_0(k_n r_0)} \sin \left(k_n \left(z + \frac{\Lambda}{2} \right) \right), \end{aligned} \quad (2.12)$$

where the i -th electrode is parameterized by its start coordinate z_{2i} , stop coordinate z_{2i-1} and the common electrode radius r_0 . The parameter d describes the spacing between adjacent electrodes. Furthermore the total trap length Λ is comprised in the discrete frequencies $k_n = n\pi/\Lambda$ of the trigonometric functions and I_0 represents the zero-order modified Bessel function of the first kind.

For a more handy representation we may also expand the potential in powers of z and normalize it to the voltage V_R applied to the central ring electrode. On the trap axis ($\rho = 0$) we can then write it as

$$\Phi(0, z) = V_R \sum_{j=0}^n C_j z^j, \quad (2.13)$$

where we introduced the C_j parameters, which contain the information about the trap geometry. Comparing with equation 2.12, we find that the individual C_j are given by

$$\begin{aligned} C_j = & \frac{1}{j! \Lambda V_R} \sum_{n=1}^{\infty} \left[\frac{V_1 \cos(k_n z_0) - V_5 \cos(k_n \Lambda)}{k_n} \right. \\ & \left. + \sum_{i=2}^5 \frac{V_i - V_{i-1}}{k_n^2 d} (\sin(k_n z_{2i}) - \sin(k_n z_{2i-1})) \right] \\ & \times \left(\frac{n\pi}{\Lambda} \right)^j \frac{1}{I_0(k_n r_0)} \sin \left(\frac{\pi}{2} (n + j) \right). \end{aligned} \quad (2.14)$$

Throughout this thesis a symmetric set of voltages is used, i.e. $V_1 = V_5 = V_{EC}$ for the endcap electrodes, $V_2 = V_4 = V_{CE}$ for the correction electrodes and $V_3 = V_R$ for the ring electrode. This additional symmetry allows us to rewrite the C_j parameters in terms of the tuning ratio V_{CE}/V_R as

$$C_j = E_j + \frac{V_{CE}}{V_R} D_j, \quad (2.15)$$

where we introduced the new parameters E_j and D_j , which are defined by the dimensions of the electrodes. When designing a trap to approximate a quadrupole

potential as well as possible, one aims for an “orthogonal” trap, i.e. $D_2 = 0$, and for the possibility to “compensate” the trap, i.e. to set $C_4 = C_6 = 0$ with a suitable tuning ratio [45]. In an orthogonal trap, the axial frequency is independent of the tuning ratio, while in a compensated trap the axial frequency does not suffer from energy dependent shifts due to higher order multipole contributions from the potential. For a compensated and orthogonal trap, the axial frequency is then given by [16]

$$\omega_z = \sqrt{\frac{2qV_R}{m}C_2}, \quad (2.16)$$

which corresponds to equation 2.5 with a characteristic trap dimension $d_0 = (2C_2)^{-2}$.

2.2 Ion plasmas and Coulomb crystals

If we want to describe the motion of many particles confined simultaneously in a Penning trap, we must consider their mutual interaction and collective effects. For the situation of two or three particles trapped together, there exists an analytical solution [47], but the approach becomes tedious for an increasing number of particles. A solution to this problem is to treat the particles as a whole and to describe them by ensemble properties.

In the language of plasma physics an ensemble of trapped charged particles of a single species is known as single component non-neutral ion plasma [48]. It is non-neutral as it is composed of charges with the same sign only. A useful parameter for the characterization of the nature of interactions within the plasma is given by the plasma parameter Γ , which measures the Coulomb energy between ions relative to their thermal energy:

$$\Gamma = \frac{q^2}{4\pi\epsilon_0 a_S k_B T}. \quad (2.17)$$

Here q is the ion charge, ϵ_0 is the vacuum permittivity, k_B is the Boltzmann constant, T is the ensemble temperature and a_S the Wigner-Seitz radius, which describes the effective ion-ion distance at a given ion number density n :

$$a_S = (4/3\pi n)^{1/3}. \quad (2.18)$$

In contrast to the classical idea of a plasma being a hot gaseous cloud, ion clouds trapped in Penning traps may also appear in liquid or solid phases. When the ions are cooled such that the average kinetic energy of the ions becomes much smaller than the Coulomb barrier from individual ions, i.e. Γ becomes large, they are not able to swap positions any more and a Coulomb crystal is formed [49]. It can be shown that for a sufficiently large plasma a transition to the solid phase occurs at $\Gamma \approx 170$ [50, 51].

As there is no particular distinguished orientation in the radial plane, a Coulomb crystal rotates in the Penning trap. In general the rotation frequency Ω takes values in the range $\omega_m < \Omega < \omega_c$, where values for the magnetron and modified cyclotron frequency correspond to the case of a single ion of the same species trapped within the same electric and magnetic fields as the crystal [52]. For cold ion clouds in Penning traps (such as Coulomb crystals) we can link the rotation frequency to the plasma density according to

$$n = \frac{m\Omega(\omega_c - \Omega)}{2\pi q^2}, \quad (2.19)$$

with a maximum density in the case of $\Omega = \omega_c/2$ [53]. In an experiment we can thus determine the plasma parameter through a measurement of the cloud's rotation frequency.

Typically, the cloud rotation will approach a steady state, which is dependent on the external torque on the ion cloud. The torque might be mediated through a ‘rotating wall’ drive [54, 55], which locks the rotation frequency to an external oscillating quadrupole field or by a laser-induced torque, which can be implemented using a non-uniform laser beam [53]. In the case of laser cooled ions, the same laser that is used for cooling can be used to generate the torque. The details of this technique are described in the next section.

2.3 Doppler cooling in Penning traps

The term ‘laser cooling’ refers to techniques that make use of radiation pressure in order to decelerate a particle’s motion. In the context of ion traps, laser cooling can be considered in two regimes: the “weak binding regime”, where the natural linewidth of the particle’s cooling transition is much bigger than the involved trapping frequencies ($\Gamma \gg \omega$), and the “strong binding” regime, where the trapping frequencies are much bigger than the natural linewidth ($\Gamma \ll \omega$).

In the weak binding regime scattering events happen on a timescale much shorter than an oscillation period and laser cooling might be treated as for the case of a free atom [18]. We usually refer to laser cooling in the weak binding regime as Doppler cooling, as it makes use of a laser beam that is tuned below the cooling resonance and preferably scatters photons when a particle moves towards it, thus shifting its frequency into resonance due to the Doppler effect [56]. Because the absorption process is connected with a change of momentum opposite to the propagation direction of the laser beam and subsequent spontaneous emission is isotropic in the general case, the net force averaged over many scattering events will be directed opposite to the direction of the particle’s motion. Therefore this cooling technique reduces the particle’s kinetic energy and the associated temperature is lowered. Typical temperatures achieved with Doppler cooling are on the order of a mK.

In Penning traps, Doppler cooling may be used to cool the axial and modified

cyclotron motion, but the nature of the magnetron motion, which comes with a negative total energy, requires a modification of the conventional approach. We can understand this by looking at the total energy of a single particle trapped in a Penning trap as derived in [57]:

$$E = \frac{1}{2}mr_z^2\omega_z^2 + \frac{1}{2}m(\omega_+ - \omega_-)(\omega_+r_+^2 - \omega_-r_-^2). \quad (2.20)$$

We see that it is dependent on the motional amplitudes r_i of the axial, modified cyclotron and magnetron motion. More specifically, an increase of the magnetron radius r_- corresponds to a decrease of the total energy. This somewhat surprising result is explained by the anti-confining behavior of the quadrupole potential in the radial direction. In order to decrease the magnetron radius, a particle has to climb up the radial potential hill. This increases its potential energy, which in turn represents the largest contribution to the total energy of the magnetron motion. For this reason, we will refer to ‘‘cooling’’ as ‘‘reducing the motional amplitudes’’ (i.e. reducing the particle’s kinetic energy) in the following. Since conventional Doppler cooling is a dissipative process that will reduce the total energy, we have to modify the technique in order to cool the magnetron mode as well.

The solution to this problem is called ‘gradient cooling’ and requires a nonuniform laser beam across the radial motion. To this end, we will assume a Gaussian laser beam propagating parallel to the x - z plane with an offset y_0 in the y -direction and an angle θ relative to the z -axis, as displayed in figure 2.3. The offset is chosen such that the magnetron motion is copropagating with the laser beam’s radial projection in the region where the intensity is maximal. Since more photons are scattered where the intensity is larger, the laser exerts a torque on the particle. This increases the total energy of the magnetron motion and the particle moves towards the trap center.

A detailed analysis of the gradient cooling technique is given in [57] and a compact summary is presented in the following for the assumptions made above. An important result is that simultaneous cooling of the modified cyclotron and magnetron motion is possible as long as the inequality

$$\omega_- < \frac{(\Gamma/2)^2 + \delta^2}{2ky_0\delta} < \omega_+ \quad (2.21)$$

is fulfilled. Here $\delta = \omega_0 - \omega_L$ corresponds to the detuning of the laser frequency from the resonance frequency of the cooling transition and $k = k_0 \sin(\theta)$ is the projection of the laser beam’s wavevector in the radial plane. In order to fulfill this condition, we may vary the trap frequencies through an adjustment of the trap voltages. In practice, however, we also need to vary the detuning and the offset of the laser beam in order to balance the Doppler cooling related and the intensity cooling related share of the cooling mechanism for the modified cyclotron and the magnetron motion.

In the case where the Doppler cooling rate is higher than the intensity cooling rate for the cyclotron motion and the Doppler cooling rate is less than and not too close to the intensity cooling rate for magnetron motion, the kinetic energies for the axial

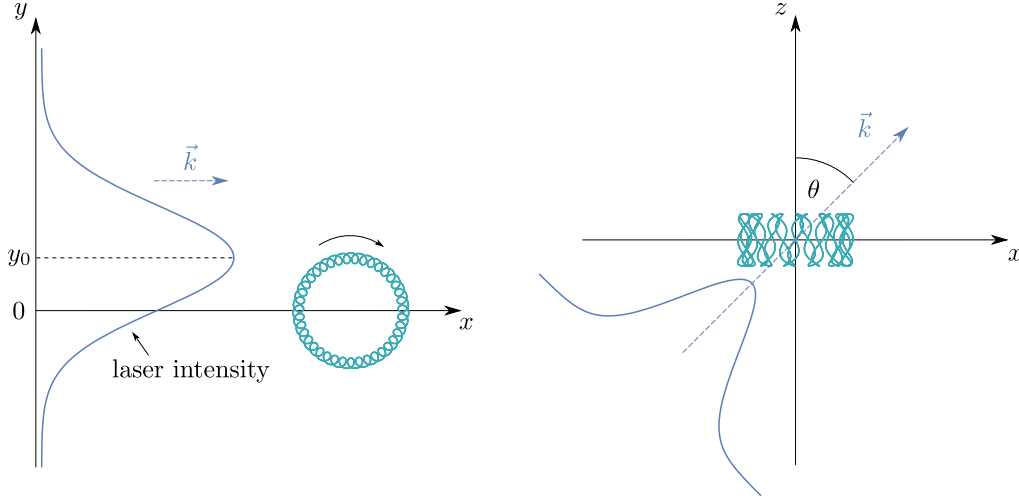


Figure 2.3: Schematic diagrams showing the cooling beam relative to the ion trajectory in the trap. Ion trajectories are exaggerated for clarity. Left: Projection of the cooling beam and the ion trajectory in the x - y plane. The offset y_0 determines the intensity gradient along the radial trajectory. Right: Projection of the cooling beam and the ion trajectory in the x - z plane. The angle θ determines the distribution of the scattered photons and thus the cooling rates in the radial and axial directions.

and modified cyclotron motion are given by the equations

$$E_z = \hbar[1 + f_{sz}/\cos^2(\theta)]\frac{(\Gamma/2)^2 + \delta^2}{8\delta}, \quad (2.22)$$

$$E_c \simeq \hbar[1 + (f_{sx} + f_{sy})/\sin^2(\theta)]\frac{(\Gamma/2)^2 + \delta^2}{4\delta}, \quad (2.23)$$

whereas the kinetic energy of the magnetron motion becomes neglectable. Here, the parameters f_{si} represent a dependency on the angular distribution of the photons scattered in the x , y and z direction. If the cooling transition corresponds to an electric dipole transition and comes with a change of the magnetic quantum number of $|\Delta m| = 1$ (which will be the case within this thesis) we need to set $f_{sx} + f_{sy} = 3/5$ and $f_{sz} = 2/5$ [57, 58].

The kinetic energy of both motions can be minimized by choosing a detuning $\delta = \Gamma/2$. For the setup of this thesis, we chose an angle of $\theta = 45^\circ$, with which we obtain the following intensity gradient cooling limits:

$$E_z = \frac{9}{40}\hbar\Gamma \equiv \frac{1}{2}k_B T_z, \quad (2.24)$$

$$E_c \simeq \frac{11}{20}\hbar\Gamma \equiv k_B T_c, \quad (2.25)$$

where we also define the equivalent one-particle-temperatures T_z and T_c for the axial and cyclotron motion, respectively. The corresponding cooling limit of the

conventional Doppler cooling technique applied to a free atom is

$$E_{\text{kin}} = \frac{1}{4}\hbar\Gamma \equiv \frac{1}{2}k_{\text{B}}T_{\text{D}}, \quad (2.26)$$

with the associated Doppler temperature $T_{\text{D}} = \hbar\Gamma/2k_{\text{B}}$ [56]. In comparison with this ‘standard’ Doppler limit, we see that the gradient cooling technique introduces a 10 % correction towards lower temperatures for the axial motion and a 10 % correction towards higher temperatures for the cyclotron motion.

In the measurements presented in this thesis, we often cannot distinguish between the temperature of the axial and the radial motion and an average must be assumed. In the cases where we are able to distinguish, the correction will be on the order or below typical measurement uncertainties. Therefore, in the following I will always refer to the cooling limit given by equation 2.26. When applying the gradient cooling technique, we aim to bring the ions as close as possible to this limit and thus measured temperatures will be compared with this value.

2.4 Motional sideband spectroscopy

If we look at the strong binding regime in ion traps, new cases of laser-ion interaction need to be considered. These introduce additional sidebands in the spectroscopy signal, which stem from a modulation of the original signal due to the ion motion [18]. The observation of sidebands is often associated with sideband cooling, which is a laser cooling technique that can be used to cool an ion to the quantum mechanical ground state of motion. In this thesis, however, we are not going to deal with sideband cooling, but will focus on spectroscopy of the motional sidebands instead. This technique will allow us to determine the temperature of a single ion or of an ensemble thereof and to distinguish the temperature of the axial motion from the temperature of the radial motions.

In the following we will introduce the basic principles of motional sideband spectroscopy for a trapped ion, recapping the arguments in reference [31]. Therefore we will restrict the interaction with the motion to the harmonic oscillation in the axial direction z , which in the experiment can be realized through an approximate choice of the laser beam alignment in the trap.

An important parameter for the description of the sideband interaction is the Lamb-Dicke-parameter η , which is a measure of how strong the ion motion is affected by the recoil of a single photon:

$$\eta = \sqrt{\frac{\omega_{\text{R}}}{\omega_z}}. \quad (2.27)$$

It relates the recoil frequency $\omega_{\text{R}} = \hbar k^2/2m$, with wavevector $k = 2\pi/\lambda$ and particle mass m , to the trap frequency ω_z . Consequently, $\eta > 1$ describes the situation, where a single recoil likely adds or removes one or more phonons to or from the ion motion,

whereas $\eta < 1$ reflects the situation where most probably only one or no phonon is added or removed.

For a quantitative treatment, we need to evaluate the Hamiltonian for the laser-ion interaction in the interaction picture,

$$H_{\text{int}} = \frac{\hbar\Omega}{2} \left[\sigma^+ e^{i\eta(\hat{a}+\hat{a}^\dagger)} e^{-i\delta t} + \sigma^- e^{-i\eta(\hat{a}+\hat{a}^\dagger)} e^{-i\delta t} \right], \quad (2.28)$$

with the Rabi rate Ω of the free ion, the raising and lowering operators σ^+ and σ^- of the ion's internal states, the (time dependent) creation and annihilation operators \hat{a} and \hat{a}^\dagger of the ion's motion and the laser detuning $\delta = \omega_0 - \omega_L$.

One can show that the interaction is mainly restricted to the cases fulfilling the resonance condition $\delta = \omega_z(n' - n)$, with integers n' and n [31]. In this context, the resonance with $n = n'$ corresponds to the detuning $\delta = 0$ and is referred to as the carrier transition. It is the only one that leaves the motional state unchanged during interaction. In the remaining cases with $n > n'$ ($n < n'$), we refer to the resonance as red (blue) sideband of the order $|\Delta n| = |n' - n|$. An interaction involving a sideband lowers or raises the phonon number of a motional Fock state from n to n' . This is equivalent to removing or adding Δn phonons to the motion, which is necessary in order to fulfill energy conservation.

In all cases, the coupling strength of the corresponding Fock states $|n'\rangle$ and $|n\rangle$ is described by the modified Rabi frequencies

$$\Omega_{n',n} = \Omega \langle n' | e^{i\eta(\hat{a}+\hat{a}^\dagger)} | n \rangle = \Omega M_{n',n}. \quad (2.29)$$

As stated in reference [31], we can calculate the matrix element comprising the interaction with the motional states using

$$M_{n',n} = \sqrt{\frac{n_{<}!}{n_{>}!}} \eta^{|\Delta n|} e^{-\eta^2/2} L_{n_{<}}^{|\Delta n|}(\eta^2), \quad (2.30)$$

where $n_{<}$ ($n_{>}$) is the lesser (greater) of n' and n , and $L_n^\alpha(x)$ is the associated Laguerre polynomial. We refer to $M_{n',n}$ as normalized coupling strengths and figure 2.4 shows the evaluation for different sideband orders as a function of the initial Fock state.

As pure Fock states are non-classical states of motion [59], they will not be produced by classical interactions such as Doppler cooling. After an initial step of Doppler cooling, we must therefore instead consider a thermal state with an occupation probability given by

$$P(n) = \frac{\bar{n}^n}{(\bar{n} + 1)^{n+1}} \quad (2.31)$$

for each individual Fock state $|n\rangle$, with a mean phonon number $\bar{n} \approx k_B T / \hbar \omega_z$ derived from the temperature T . The measured spectrum will then correspond to the weighted average of sideband spectra corresponding to each Fock state.

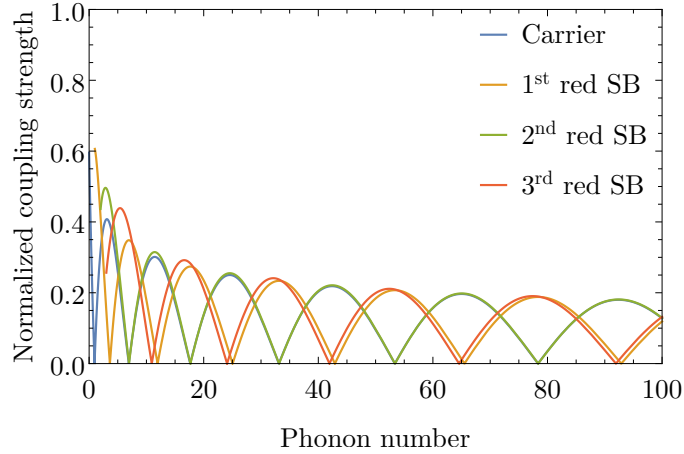


Figure 2.4: Normalized coupling strength plotted against the initial phonon number for carrier and 1st-, 2nd- and 3rd-order red sideband of ${}^9\text{Be}^+$ with a trap frequency of 436 kHz and light at 313 nm. The Rabi frequencies of the carrier and the 2nd-order red sideband converge for high phonon numbers. The same applies to the 1st- and 3rd-order red sideband. Due to the comparable high Lamb-Dicke-parameter $\eta \approx 1$, the coupling strengths of the sidebands vanish for several phonon numbers. For the calculations it is assumed that the ions are cooled to the Doppler limit.

Typical experimental parameters in this thesis will result in a high mean occupation number on the order of $\bar{n} \approx 85$ and a Lamb-Dicke parameter $\eta \approx 1$. One can show that in this case the averaged spectra will follow a Gaussian envelope as in the classical picture, which predicts a Doppler broadened spectrum [18]. We will use this fact and measure the Doppler width of the resulting spectra in order to determine the temperature and the mean occupation number after Doppler cooling. In combination with a pair of Raman laser beams, we can restrict the interaction of this technique to a single motion, which for example enables to distinguish the temperature of the axial motion from the temperature of the radial motions in the Penning trap.

CHAPTER 3

Overview of the experimental setup

The following chapter provides an overview of the experimental setup that has been used for the measurements presented in this thesis. Section 3.1 motivates the decision to choose beryllium as our ion species and provides details on the level structure that emerges from the Penning trap's magnetic field. In section 3.2 the current Penning trap stack is presented and the traps and their specific purposes are described, where the focus is placed on the beryllium trap. An overview of the cryo-mechanical setup, which houses the trap stack and provides a cryogenic vacuum for the experiment, will be given in section 3.3. Next, all optical subsystems that are required for the operation of the experiment, such as laser systems, optical platforms and imaging optics are described in section 3.4. The chapter finishes with a description of the experiment control system in section 3.5.

3.1 The beryllium ion

The main goal of the BASE experiment in Hannover is the development of new techniques for sympathetic laser cooling of (anti-)protons and the demonstration of a protocol for g -factor measurements based on quantum logic spectroscopy [34]. To this end, we aim for Coulomb coupling of a single auxiliary ion to a single (anti-)proton in a double-well potential [31]. In the intended setup, both particles can be brought to close vicinity and exchange their motional energies. On the one hand, this allows for sympathetic cooling of the (anti-)proton through laser cooling of the auxiliary ion. On the other hand, this enables the particles to exchange information about their quantum states as required for quantum logic spectroscopy.

A simple picture for the energy exchange is given in terms of two coupled pendulums. Only if both oscillate with the same resonance frequency, a complete transfer of the energy from one pendulum to the other is possible. The same is true for two coupled particles. To achieve complete energy transfer, the same oscillation frequency is required for both. Thus, we need to compensate for the mass difference between the auxiliary ion and the (anti-)proton through an adjustment of the ratio of curvature of the potential at the positions of the particles. In a double-well potential, this

situation is more difficult to achieve the more the mass of the auxiliary ion is different from the mass of the (anti-)proton [60]. This consideration leads us to beryllium, which is the lightest readily laser-coolable ion species.

Beryllium is the fourth element in the periodic table and belongs to the alkaline earth metals. In its singly ionized state, it comes with a single valence electron, corresponding to an alkaline metal like electronic structure. In the following, the level structure for ${}^9\text{Be}^+$ is presented, which is the ionized version of the sole stable beryllium isotope.

3.1.1 Electronic level structure

For laser cooling, state manipulation and fluorescence detection of ${}^9\text{Be}^+$, lasers with a wavelength of $\approx 313\text{ nm}$ are required. These are used to drive transitions between the ${}^2S_{1/2}$ ground state manifold and the ${}^2P_{1/2}$ or ${}^2P_{3/2}$ excited state manifold, where the latter are separated by a fine structure splitting of about 197 GHz [61]. Since no other relevant metastable excited states are present in the level structure of ${}^9\text{Be}^+$, no further wavelengths are required.

As we use a 5 T magnetic field to confine the ions in our Penning trap, significant Zeeman shifts are introduced to the level structure. With a magnetic field as strong as this, we operate in the deep Paschen-Back regime, where the total angular momentum J and the nuclear spin I are decoupled and the magnetic quantum numbers m_J and m_I define the states in the hyperfine manifold. The corresponding level scheme with laser transitions for cooling, repumping and qubit state manipulation is shown in figure 3.1.

We implement Doppler cooling with a laser tuned close to the transition between the ${}^2S_{1/2} |m_I = +3/2, m_J = +1/2\rangle$ state and the ${}^2P_{3/2} |m_I = +3/2, m_J = +3/2\rangle$ state. Due to the large frequency offset to neighboring Zeeman levels, state selection can be ensured with an appropriate choice of the laser frequency without the need for high purity laser polarization. Thus, a closed cooling cycle can be implemented with a single laser only. However, residual off-resonant excitations and subsequent decays still trap a small fraction of the population in the ${}^2S_{1/2} |m_I = +3/2, m_J = -1/2\rangle$ state [62]. As a countermeasure, a repumping laser resonant with the transition between the ${}^2S_{1/2} |m_I = +3/2, m_J = -1/2\rangle$ state and the ${}^2P_{3/2} |m_I = +3/2, m_J = +1/2\rangle$ state is used. In this way, high fidelity state preparation in the ${}^2S_{1/2} |m_I = +3/2, m_J = +1/2\rangle$ state is possible. Furthermore, we adjust the polarization of the laser beams so that the share of σ^+ polarization is maximized. In combination with the resonance conditions this creates a bias for angular momentum increasing transitions and ensures that the nuclear spin is prepared in the $m_I = +3/2$ state and can be neglected in the following.

In the context of sideband spectroscopy and sideband cooling, we refer to the states in the ${}^2S_{1/2}$ manifold as qubit states. In this thesis it is shown that the transition between the two states can be addressed with a two-photon Raman process using two phase-locked cw lasers at 313 nm (see section 3.4.4 and chapter 6). In the context of fluorescence detection, we refer to the ${}^2S_{1/2} |m_J = +1/2\rangle$ state as the “bright”

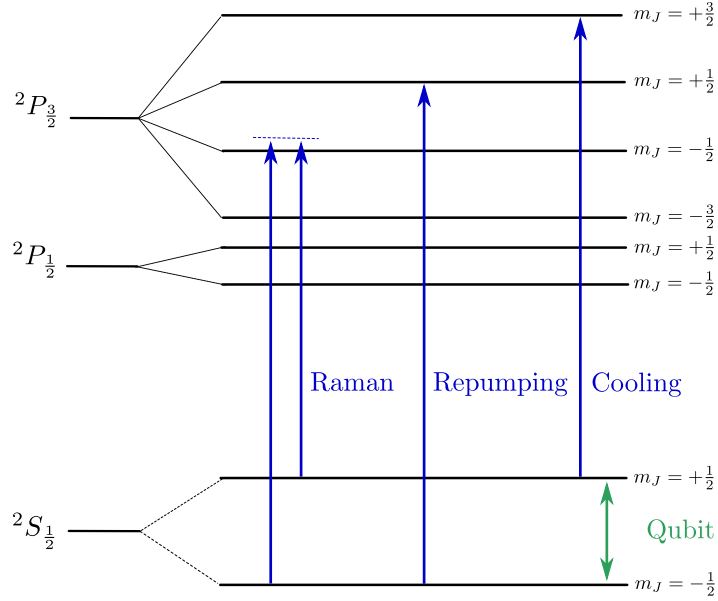


Figure 3.1: Energy level diagram and relevant transitions for ${}^9\text{Be}^+$ in a 5 T magnetic field. Optical transitions for Doppler cooling, repumping and Raman interactions are shown. The Raman laser system can be used to drive the transition between the qubit levels ${}^2S_{1/2} |m_J = \pm 1/2\rangle$. Only levels with $m_I = +3/2$ are depicted.

state and to the ${}^2S_{1/2} |m_J = -1/2\rangle$ state as the “dark” state, corresponding to the fact that photons can be scattered from the cooling laser beam or not if the ion is prepared in either of this states.

Transition frequencies and wavelengths of the above transitions for a magnetic field of 5 T are given in table 3.1. The calculations of transition frequencies and wavelengths are based on the equations given in appendix A.

Table 3.1: Calculated transitions frequencies for ${}^9\text{Be}^+$. The uncertainties are dominated by the uncertainty of the literature values of the field free transitions and the assumed magnetic field uncertainty of 1 mT.

Transition	Frequency	Wavelength
Cooling	957.467 25(14) THz	313.109 88(4) nm
Repumping	957.517 93(14) THz	313.093 31(4) nm
Qubit	139.189(28) GHz	2.1538(4) mm

3.2 Penning trap stack

The current Penning trap stack is an intermediate step towards sympathetic ground state cooling of single (anti-)protons. It comprises four cylindrical Penning traps and a proton source. The design of the traps was chosen individually in order to

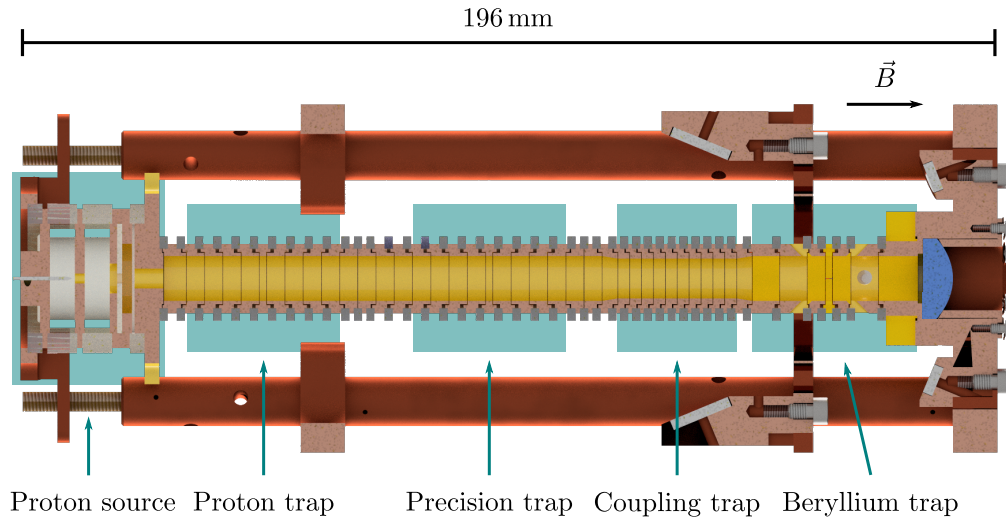


Figure 3.2: Cross-section view of the trap stack from the top. The trap stack consists of four dedicated Penning traps and a proton source. In between the beryllium trap, the coupling trap, the precision trap and the proton trap, additional auxiliary electrodes are placed. On the side of the beryllium trap, the trap stack is completed by a large endcap electrode and the trap base, which holds an aspheric lens for fluorescence detection. On the side of the proton source, an electron gun completes the trap stack. All parts are clamped together with a copper support structure. Laser beams can be steered through the beryllium trap with the mirrors that are mounted to the support structure.

fulfill the requirements for the following tasks:

- **Beryllium trap:** loading, preparation, cooling and detection of ${}^9\text{Be}^+$ ions
- **Coupling trap:** Coulomb coupling of ${}^9\text{Be}^+$ ions in a double-well potential
- **Precision trap:** detection and pre-cooling of protons
- **Proton trap:** storage of protons

A cross-section view of the complete trap stack is given in figure 3.2. All electrodes are made out of oxygen-free high conductivity (OFHC) copper and plated with a nickel diffusion barrier and hard gold. They are spaced and electrically isolated by rings made of sapphire. The dimensions of the individual electrodes were chosen as a trade-off between manufacturing capabilities, feasible trap voltages, image-charge shifts, image currents and heating rate. Details on the designs and the manufacturing process are given in reference [39]. A copper support structure is used to clamp all parts together. In the following we will focus on the beryllium trap as all measurements described in this thesis have been carried out there.

3.2.1 The beryllium trap

The beryllium trap is a five-pole Penning trap with an inner diameter of 9 mm. It evolved from the precision trap described in reference [64] and was adapted to allow for the production, preparation, cooling and detection of ${}^9\text{Be}^+$ ions. The ring electrode is radially split in four segments and enables the application of a dipole RF field for the excitation of the radial motions or a quadrupole RF field for coupling the magnetron and modified cyclotron motion [65]. In addition, the endcap electrodes are divided into two pieces to improve the transport of particles into and out of the trap. A cross-section view of the beryllium trap is shown in figure 3.3.

Ions are produced in-situ via laser ablation from a solid beryllium target housed in a 3 mm hole in one endcap. Optical access to the target is provided by a second hole on the opposite side of the electrode. For ablation, a 532 nm pulsed laser is sent into the system parallel to the magnetic field, where it is deflected and focused onto the target by an off-axis parabolic (OAP) mirror. For cooling, manipulation and fluorescence detection of the ions, four additional holes with a diameter of 1.5 mm are machined into the electrodes. These allow for the introduction of laser beams to the trap with an angle of 45° or 135° relative to the magnetic field. The laser beams at 313 nm are sent to the system parallel to the trap stack and then deflected by ultraviolet (UV) enhanced aluminum mirrors at the respective angles. The mirrors are shown in figure 3.2.

The beryllium trap is mounted on the trap base, which houses an aspheric lens. The latter allows for efficient fluorescence collection despite limited optical access. Both the lens and its mount are designed to reduce the influence of misalignment due to machining tolerances and material contraction during cooldown of the system (see section 3.3 for more information on the cryo-mechanical setup). In order to minimize stray charges on the non-conductive surface of the lens, a gold mesh is clamped between two electrodes 1 mm in front of the mesh. The design of the aspheric lens is described in reference [41].

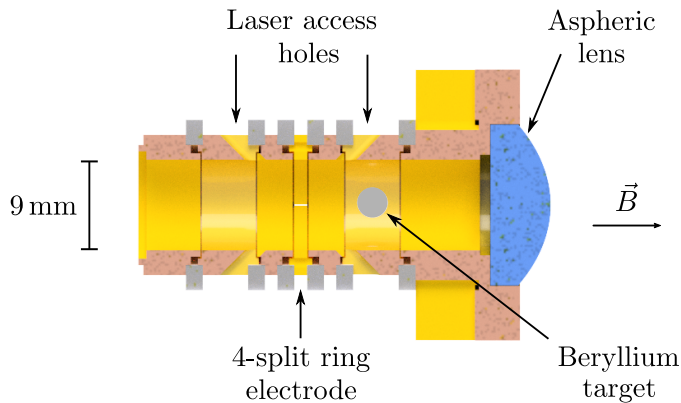


Figure 3.3: Cross-section view of the beryllium trap. See text for details.

3.2.2 Other traps

Despite their intended purpose, the other traps of the trap stack have been used for storage and splitting of beryllium clouds during my time at the experiment. In the future, the additional traps are required to demonstrate Coulomb coupling of single ions or ion clouds and to produce, prepare, pre-cool and detect protons. In the following, a short overview is given over the remaining traps.

The **coupling trap** is built out of ten identical electrodes with an inner diameter of 8 mm. The electrodes are 2.25 mm thick and come with a spacing of 0.14 mm. This geometry allows for the engineering of a symmetric double-well potential for first tests of the Coulomb coupling procedure with single ions or ion clouds in Penning traps [39]. In the future, this trap will be replaced by a scaled and microfabricated trap, that will allow for engineering of asymmetric double-well potentials with interparticle distances as small as 300 μm [35].

The **precision trap** is a reproduction of the precision trap described in reference [64]. It has an inner diameter of 9 mm and is compensated and orthogonal. The trap is equipped with one superconducting and one non-superconducting resonator. In combination with two ultra-low noise cryogenic amplifiers, these resonators allow for image charge detection of the particle's motion in the trap. In addition the resonators can be used to thermalize particles with the surrounding environment [66]. One correction electrode and one endcap are connected to an RF line each, which allows for excitation of the axial and radial motion as well.

The **proton trap** is another copy of the precision trap and is connected to a proton source that houses an electron gun and a polyethylen target [67, 68]. The proton source offers the possibility to produce protons (and other contaminant ions) through impact ionization, which can be parked in the proton trap until they are required for a measurement in the precision trap. The proton source is located at the end of the trap stack and thus completes it.

3.3 Cryo-mechanical setup

To enable a future technology transfer from the BASE experiment in Hannover to the BASE experiment at CERN, we have set up a complex cryogenic vacuum system, which is similar to the CERN setup [69] in many, but not all aspects. A simplified sketch of the setup is shown in figure 3.4 and a corresponding rendered image is provided in appendix B.

The core of our experiment is the trap stack, which is located in an inner vacuum chamber, called the “trap can”. The purpose of this inner vacuum chamber is to create an ultra-low vacuum pressure down to the 10×10^{-18} mbar regime, which is necessary to reduce the rate of background gas collisions and to increase the lifetime of anticipated future antiprotons [11]. Although we are not operating with antiprotons yet, it increases the lifetime of beryllium ions as well and prevents stray light from outside the beryllium trap from reaching the imaging optics. The trap can

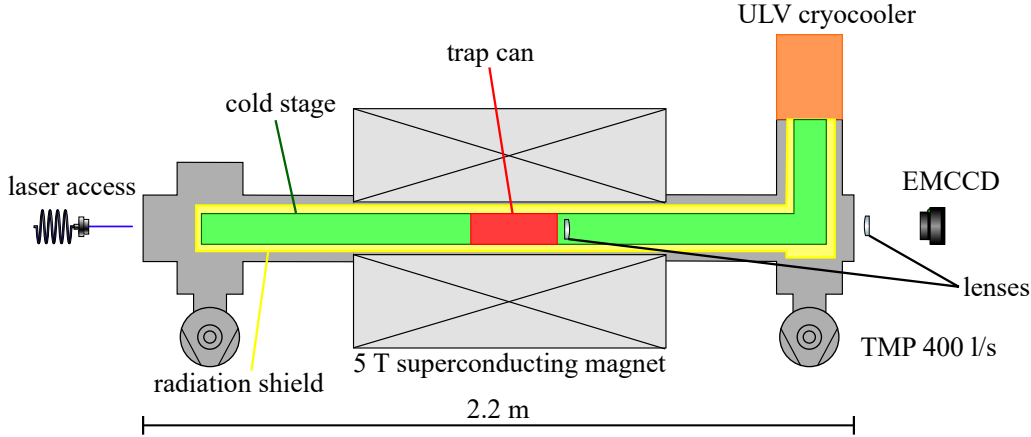


Figure 3.4: Simplified sketch of the cryo-mechanical setup. The trap can (red) is mounted in a support structure that is cooled by a cryocooler (orange). The inner support structure (“cold stage”, green) is connected to the 4 K stage of the cryocooler, while the outer support structure (“radiation shield”, yellow) is connected to the 40 K stage. The 5 T superconducting magnet (light grey) is part of the outer vacuum chamber (dark grey). Drawing not to scale. See text for details. The figure was taken from reference [40].

is a cylinder made of OFHC copper that is sealed with two flanges and indium. The flanges are made out of rings of OFHC copper into which custom plates made from stainless steel have been vacuum soldered. The plate on the side that is closer to the beryllium trap contains a central anti-reflection (AR) coated window that allows the fluorescence light to leave the trap can. In addition multiple feedthroughs for DC and RF signals are welded into the flange around the window. The steel plate on the other side of the trap can contains three AR coated windows and a pinch-off tube. One of these windows allows the ablation laser to enter the trap can, while the other two allow UV lasers to enter the system and leave it again after passing the beryllium trap. We pump the trap can with a scroll pump and a turbomolecular pump (TMP) before pinching it off and mounting it in the system.

The trap can is bolted to a cylindrical support structure made from OFHC copper and titanium, together with which it forms the “cold stage”. Its name is derived from the fact that it is connected to a 2-stage cryocooler (*Sumitomo, RDK-415D*), which is equipped with an ultra-low vibration (ULV) interface (supplied by *ColdEdge Technologies*) and used to cool down the structure to cryogenic temperatures [39]. Optimal thermal contact between the copper part of the structure and the 4 K stage of the cryocooler is thereby ensured through a connection with an annealed OFHC copper rod and custom made flexible copper braids are used to reduce the transfer of residual vibrations. In order to reduce the heat load on the cold stage, it is wrapped in multilayer superinsulation foil and mounted to a cylindrical radiation shield made of aluminum. The connection is realized via two maze-like G10 spacers, which reduce the thermal flux between the two parts. The radiation shield itself is connected to the 40 K stage of the ULV cryocooler via four OFHC copper rods

and additional copper braids, and is wrapped in multilayer insulation foil as well. In turn, the radiation shield is mounted inside the 160 mm room temperature bore of a custom 5 T superconducting magnet (built by *Oxford Instruments*) with two additional maze-like G10 spacers.

The outer vacuum chamber is completed by two vacuum crosses that are attached the open ends of the magnet's bore with stainless steel bellows. On the side, where the cryocooler is mounted on top of one of the vacuum crosses, the flanges closing the vacuum come with a window that allows to collect the fluorescence light from the beryllium trap with an imaging system and several electrical DC and RF feedthroughs. The flanges of the vacuum cross on the other side of the magnet come with two windows which allow the ablation and UV laser beams to access and exit the vacuum system. The whole vacuum system is pumped by a scroll pump and two TMPs that are mounted below the vacuum crosses.

Since we use a closed-cycle cryocooler, no regular top up of cryoliquids is necessary. However, nitrogen and helium top up is necessary for the operation of the superconducting magnet. We fill the magnet with liquid nitrogen on a weekly basis, while helium filling is necessary about every eight weeks.

More details on the vacuum system, the low-vibration cryocooler and the superconducting magnet are given in reference [39].

3.4 Optical Subsystems

In this section, all optical system required for the operation of the experiment are described. For production of ${}^9\text{Be}^+$ ions, we use a setup based on a commercial pulsed laser, which is introduced in subsection 3.4.1. For cooling, repumping and Raman interactions we use four similar UV laser systems, which were specifically designed and set up for our experiment. They are described in detail in subsection 3.4.2. For laser beam delivery close to the vacuum system, a custom movable non-magnetic optical platform is used, which is described in subsection 3.4.3. In addition, a setup to lock the phase of the UV lasers, as required for coherent Raman interactions, is presented in subsection 3.4.4. At last, the setup for imaging and detection of the ion fluorescence is described in subsection 3.4.5.

Most components for the drawings in this section were taken from reference [70].

3.4.1 Ablation laser

The ablation laser is a commercial Nd:YAG laser (*Continuum, Minilite I*), which is equipped with a frequency-doubling kit. In Q-switched operation, the laser generates pulses with a pulse length between 5–7 ns and pulse energies up to 20 mJ at 532 nm. This energy can be reduced with a built-in attenuator and a setup consisting of a $\lambda/2$ -waveplate and a polarizing beamsplitter (PBS) cube, which is placed behind the output. The second input port of the cube is used to overlap a low-power 532 nm pilot beam from a compact diode-pumped solid state laser module (*Thorlabs*

CPS532-C2) with the ablation laser. This beam is used for alignment and reduces the risk of potential damage due to unintended reflections and uncontrolled ablation. The overlapped beams are sent to the vacuum chamber, where they are focused onto the beryllium target by the OAP mirror. The ablation laser is used in single-shot mode for trap loading.

3.4.2 UV laser systems

In our experiment we use laser systems that are similar to the setups described in references [71, 72]. Fiber laser systems consisting of a pair of seed lasers and amplifiers running at 1552 nm and 1050 nm are used for sum frequency generation (SFG) of laser light at 626 nm, which is subsequently converted to 313 nm in a second harmonic generation (SHG) stage. Due to the required large detuning between different lasers, each laser system for cooling, repumping and the Raman beams requires its own pair of fundamental infrared (IR) fiber lasers. Nevertheless, by sharing the power of one 1050 nm laser system between the cooling and repumping lasers and the power of another 1050 nm laser system between both Raman lasers, the number of required IR laser systems is minimized. In total we use four fiber laser systems at 1552 nm (*NKT Photonics, Koheras BOOSTIK HP E15 system*) and two fiber laser systems at 1050 nm (*NKT Photonics, Koheras BOOSTIK HP Y10 system*).

As space is limited in our lab, we follow a modular approach for the setups for SFG and SHG. In all cases, two SFG setups are housed together in a single laser box while the SHG setup for each laser is built as a separate module. The fundamental lasers and the boxes are connected via fibers, which enables flexible placement. An

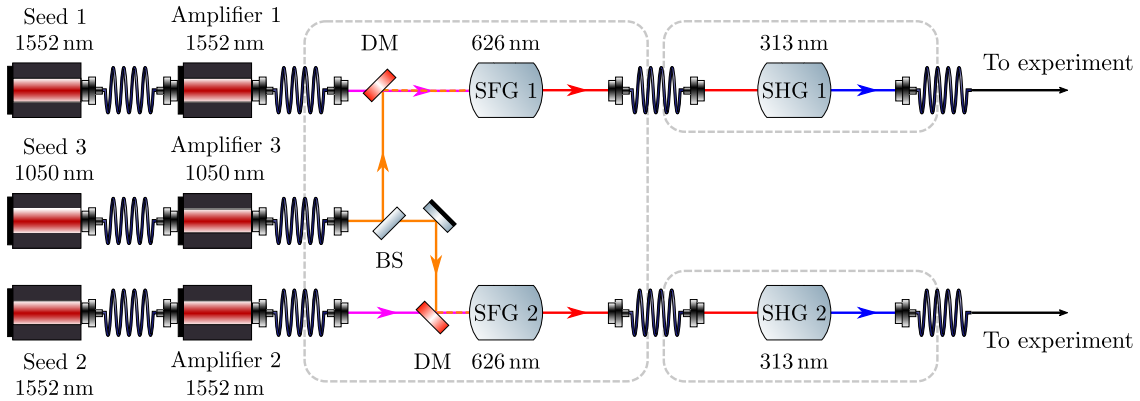


Figure 3.5: Overview of a laser system that is used to generate two beams at 313 nm. Light at 1552 nm and 1550 nm is converted to 626 nm and subsequently to 313 nm using setups for SFG and SHG. The grey dashed lines indicate a joint setup, which is housed in a single laser box. The IR lasers and the boxes are connected via fibers. A setup like this is used for the generation of the cooling and repumping beams, and another one is used for the generation of both Raman lasers. BS: beam splitter. DM: dichroic mirror.

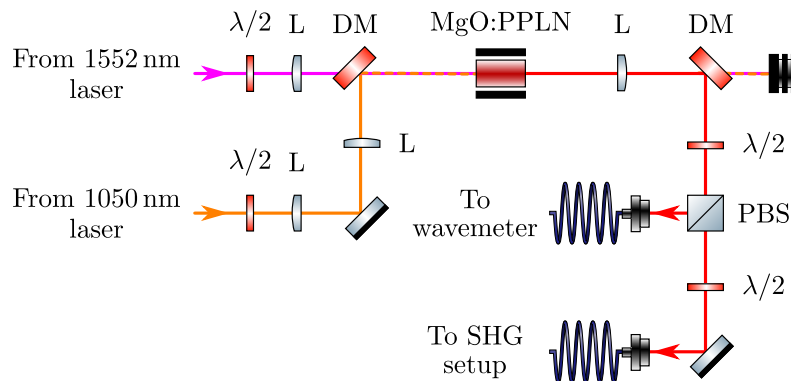


Figure 3.6: Schematic of the setup for SFG. See text for details. L: lens, DM: dichroic mirror, PBS: polarizing beamsplitter.

overview of such a setup is shown in figure 3.5.

The SFG setup is similar for all lasers and details on individual systems are given in references [73, 74]. In the following, the setup of one Raman laser beam is described (see figure 3.6). We use a magnesium-doped periodically poled lithium niobate (MgO:PPLN) crystal with dimensions $0.5 \times 10 \times 40 \text{ mm}^3$ that contains three poled lanes with cross sections of $0.5 \times 0.5 \text{ mm}^2$ and periods of $11.12 \mu\text{m}$, $11.17 \mu\text{m}$ and $11.22 \mu\text{m}$. Using a single lens with focal length $f = 200 \text{ mm}$ for the 1552 nm beam and a telescope with focal lengths $f_1 = -50 \text{ mm}$ and $f_2 = 100 \text{ mm}$ for the 1050 nm beam, both IR beams are focused into the crystal lane with a poling period of $11.22 \mu\text{m}$. As thermal effects in the crystal lead to a strong deviation from the free space beam waists, the optimal lenses, lens positions and beam waists were determined experimentally, where parameters known from similar setups [73, 75] were used for orientation. The polarization of both lasers is optimized with a $\lambda/2$ -waveplate in each case. An oven is used to heat the PPLN crystal to 171.90°C to optimize quasi-phase-matching and maximize the conversion efficiency. Dichroic mirrors are used to overlap the IR beams in front of the PPLN crystal and to separate the light at 626 nm from the IR light behind the crystal. The red light is collimated with a $f = 125 \text{ mm}$ lens.

SFG power levels and conversion efficiencies are shown in figure 3.7. For the maximum input power levels $P_{1550} = 4.97 \text{ W}$ and $P_{1050} = 2.01 \text{ W}$ a typical output power of $P_{626} = 1 \text{ W}$ is generated. This corresponds to a conversion efficiency of

$$\eta_{\text{SFG}} = \frac{P_{626}}{P_{1550} \times P_{1050} \times l_{\text{PPLN}}} = 2.51 \text{ \% W}^{-1} \text{ cm}^{-1} \quad (3.1)$$

for the crystal length $l_{\text{PPLN}} = 4 \text{ cm}$.

A small fraction of the light at 626 nm is split off the main beam with a $\lambda/2$ -waveplate and a PBS. It is coupled into a single mode (SM) fiber, which guides the light to a wavemeter. This allows to measure the laser frequency and to stabilize it via feedback to the modulation input of the 1552 nm seed laser (see section 3.5 for details). The remaining power is coupled into a 5 m polarization-maintaining (PM)

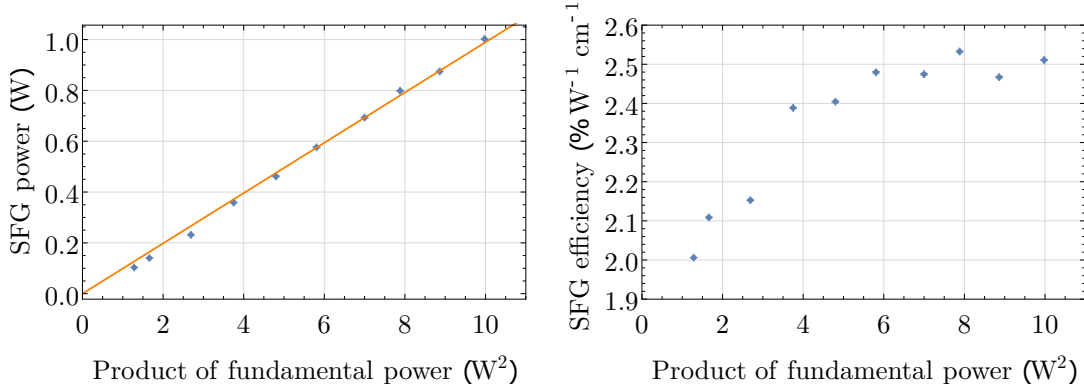


Figure 3.7: Left: SFG power as a function of the product of the fundamental power. The solid orange line is a linear fit to the data, corresponding to an average conversion efficiency of $2.47\% \text{ W}^{-1} \text{ cm}^{-1}$. Right: SFG efficiency as a function of the fundamental power.

fiber, which guides the light to the SHG setup. Another $\lambda/2$ -waveplate is used to adjust the polarization in front of the fiber, which is optimized using a polarization analyzer (*Schäfter+Kirchoff, SK010PA-VIS*).

The SHG stage is identical for all lasers systems (see figure 3.8). For frequency doubling to 313nm, we use a $4 \times 4 \times 10 \text{ mm}^3$ Brewster-cut beta barium borate (BBO) crystal, which is placed inside a bow-tie cavity for power enhancement. The cavity has a monolithic design with high long-term stability and low maintenance requirements [76]. We focus the 626 nm beam leaving the PM fiber into the cavity using a telescope consisting of two plano-convex lenses with focal lengths $f_1 = 50 \text{ mm}$ and $f_2 = 30 \text{ mm}$. The resulting beam waist of $139 \mu\text{m}$ optimizes the mode overlap

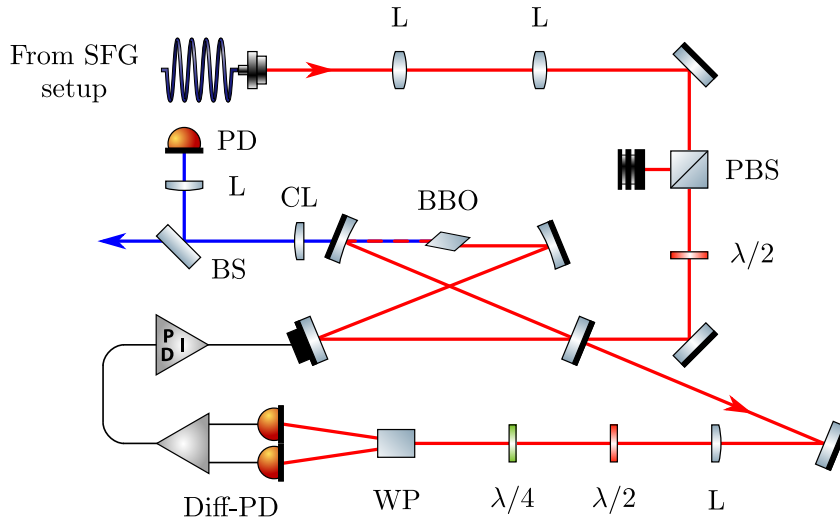


Figure 3.8: Schematic of the setup for SHG. See text for details. L: lens, PBS: polarizing beamsplitter, CL: cylindrical lens, BS: beam sampler, PD: photodiode, WP: Wollaston prism, Diff-PD: differential photodetector.

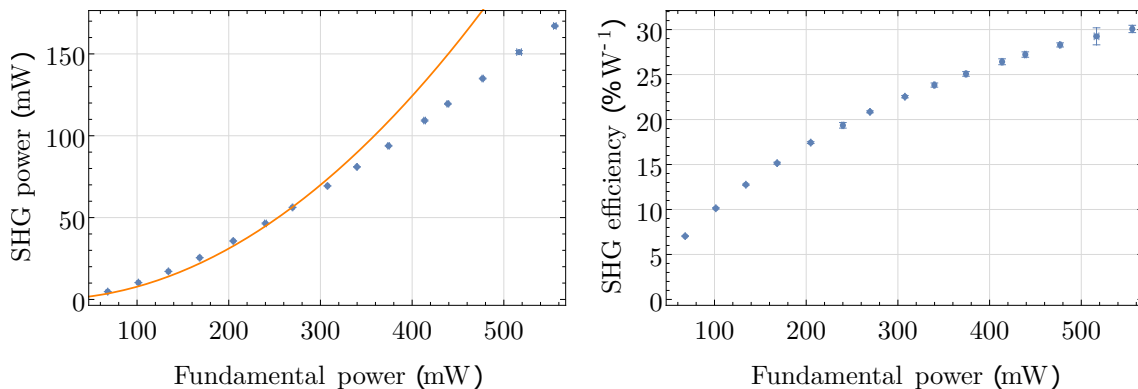


Figure 3.9: Left: SHG power as a function of the fundamental power. The solid orange line is a quadratic fit to the first 8 data points. It shows the quadratic dependence of the conversion process on the fundamental power. For high power levels the conversion efficiency saturates, since the increasing conversion losses for the fundamental power reduce the power enhancement in the cavity. Right: SHG efficiency as a function of the fundamental power.

with the cavity beam. The polarization of the fundamental beam is filtered using a PBS and adjusted with a $\lambda/2$ -waveplate. For type-I critical phase-matching, the alignment of the crystal with respect to the intra-cavity beam can be optimized with a 5-axis translation stage integrated into the monolithic cavity housing. The crystal mount is heated to 30 °C to avoid condensation and crystal degradation due to the hygroscopic nature of BBO. In addition, the whole cavity is flushed with oxygen to avoid UV degradation of the crystal surfaces. The cavity length is stabilized via feedback to a piezo-mounted cavity mirror using the Hänsch-Couillaud locking scheme [77] and a custom digital proportional-integral-derivative (PID) controller built at Physikalisch-Technische Bundesanstalt (PTB) [78]. Behind the cavity, the leaking fundamental light is filtered with a dichroic mirror from the UV light. A cylindrical lens with focal length $f = 100$ mm is used to collimate the UV beam and fraction of the beam is picked up with a beam sampler, so that the UV power can be monitored with a photodiode.

Figure 3.9 shows SHG power levels and conversion efficiencies for one cavity of the Raman laser beams. With an input power of $P_{626} = 556$ mW typically up to $P_{313} = 167$ mW are generated in the UV. This gives a conversion efficiency

$$\Gamma_{\text{SHG}} = \frac{P_{313}}{P_{626}^2} = 30.1 \text{ \%W}^{-1}. \quad (3.2)$$

The 313 nm beam is sent to a compact double-pass acousto-optic modulator (AOM) setup, which is part of the same laser box as the SHG setup. The setup is used for switching, fast frequency shifting as well as power stabilization. A schematic is shown in figure 3.10. We use a 110 MHz modulator (*Gooch & Housego, I-M110-3C10BB-3-GH27*) in combination with a retro reflecting right angle prism and a D-shaped mirror to separate the incoming and outgoing beams without polarization

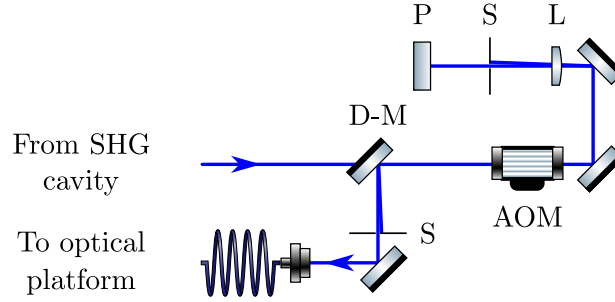


Figure 3.10: Schematic of the double-pass AOM setup. The diffracted beams are aligned so that only the first diffraction order is passing the mechanical slits. The incoming and outgoing beams are separated in front of the AOM in the vertical direction using a D-shaped mirror. D-M: D-shaped mirror, L: lens, S: mechanical slit, P: retro reflecting prism.

optics. Due to the limited space in the SHG laser box, the beam needs to be folded behind the AOM and a lens with a comparably short focal length of $f = 100$ mm is required for parallelization of the diffracted laser beam. The separation with the D-shaped mirror requires an angle in the vertical direction between the incoming and outgoing beam, which limits the achievable diffraction efficiency. Typical double-pass efficiencies achieved with this setup are in the range between 50 % and 60 %.

In order to guide the UV laser beams to the vacuum system, they are coupled into a PM fiber and sent to the laser beam delivery platform, which is described in the following.

3.4.3 Laser beam delivery platform

An optical setup on a non-magnetic static platform close to the vacuum system is used to send the laser beams to the beryllium trap. The 102 mm thick honeycomb breadboard as well as the support structure of the platform are made from grade 316L stainless steel to avoid problems due to the proximity to the 5 T superconducting magnet. The complete platform is U-shaped, so that it can enclose the vacuum cross, which optimizes the use of limited space in the lab. In addition, the support structure is equipped with retractable wheels, which allows to remove the optical platform as a whole, if the vacuum system is opened. The optical platform is shown on the left of the rendered image of the experimental setup in appendix B.

Four custom UV-compatible photonic crystal fibers are used to guide the beams for cooling, repumping and Raman interactions from their enclosures to the optical platform. To this end, patch cords with a length of 6 m are produced from bare fibers (*NKT Photonics, LMA-10-PM*) following the recipe in appendix C. To avoid fiber tip degradation, all fiber collimators (*Schäfter+Kirchoff, 60FC-4-S24-49-XV*) are permanently flushed with dry nitrogen.

On the optical platform, four identical setups are used to prepare the laser beams with a large beam diameter, pure polarization and stable power. A sketch of the

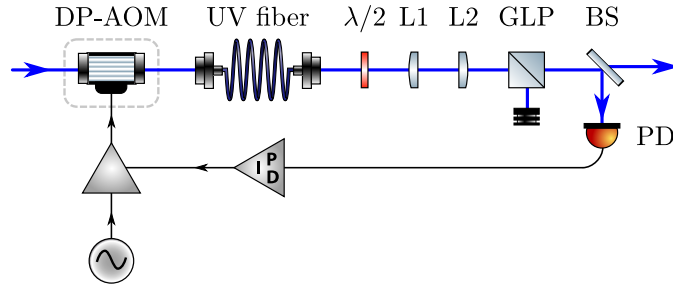


Figure 3.11: Schematic of the setup for laser beam preparation. See text for details. DP-AOM: double-pass AOM setup, L1/L2: lens 1/2, GLP: Glan-laser polarizer, BS: beam sampler, PD: photodiode

setup is shown in figure 3.11. Each laser beam is collimated and expanded to a beam diameter of about 6 mm with a telescope consisting of two plano-convex lenses with focal lengths $f_1 = 50$ mm and $f_2 = 200$ mm. A $\lambda/2$ -waveplate is used together with a Glan-laser α -BBO polarizer (*Thorlabs, GLB10-UV*) to clean the polarization. Afterwards, a small fraction of the laser power is picked up with a beam sampler (*Thorlabs, BSF10-UV*) and sent to an amplified photodiode with switchable gain and large active area (*Thorlabs, PDA100A2*) in order to stabilize the laser power. The feedback loop for stabilization consists of a digital PI controller with a bandwidth of 50 kHz and a 10 W RF amplifier, both of which were built at PTB. Here, the amplifier controls the power of the modulation signal for the same AOM, that is also used for shifting the laser frequency of the respective laser (see section 3.4.2). The regulator compares the photodiode voltage with an external setpoint, which is adjustable with the experiment control system (see section 3.5). The control signal is fed into the gain port of the RF amplifier, which in turn adjusts the diffraction efficiency of the AOM and thus the power coupled into the UV fibers. Both the RF amplifiers as well as the controller were built at PTB. The stabilization setup reduces the root mean square (RMS) power fluctuations of the UV lasers to below 0.05%. This is a reduction of more than a factor of 20 in comparison with the non-stabilized setup as depicted in figure 3.12.

Afterwards, all beams need to be combined before entering the vacuum system. Figure 3.13 shows the setup for overlapping and focusing the beams. The cooling laser is overlapped with the repumping laser using a 50/50 beam splitter (*Thorlabs, BSW20*). In front of the beamsplitter, the polarization of both beams is adjusted with $\lambda/2$ -waveplates, so that the combined beam can be overlapped with one of the Raman laser beams using an additional Glan-laser polarizer. Here, the Raman beam is introduced into the front port of the polarizer, while the beam comprising the cooling and repumping lasers is introduced into the side port under an angle of about 61° . In this configuration, the polarization of the cooling and repumping lasers is always orthogonal the polarization of the Raman laser. Afterwards, a $\lambda/4$ -waveplate is used to convert the polarization of the cooling and repumping lasers to left circular polarization and the polarization of the Raman laser to right circular polarization.

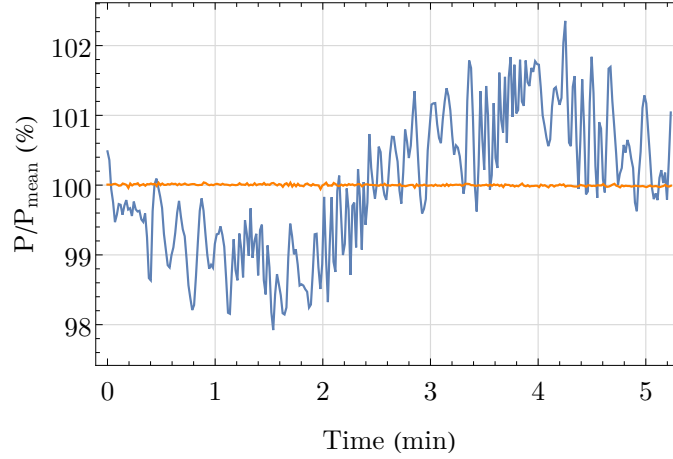


Figure 3.12: Power variation of one Raman laser beam relative to its mean power over time. Blue: Power stabilization feedback deactivated. Orange: Power stabilization feedback activated. See text for details.

The combined beam is focused with a lens with a focal length of $f = 1592$ mm (*CVI Laser Optics, PLCX-25.4-772.6-UV-248*) into the vacuum system, resulting in a focus position roughly at the center of beryllium trap. Despite the weak focussing, beam waists on the order of $100\ \mu\text{m}$ can be realized due to the large initial beam diameter. The lens is mounted on two motorized piezo translation stages (*Physikinstrumente, Q-545.240*), which allow for adjustment of the focus position in the transverse direction with nanometer resolution. An identical setup is used for focusing the second Raman laser beam into the vacuum system, which allows for an independent adjustment of the laser beam path and the focus position.

The last optical element in front of the vacuum system is a 2" 50/50 beam splitter (*Thorlabs, BSW21*), which is used to combine the second Raman laser beam with the other beams. The large size of the beam splitter allows to either overlap all beams or to adjust the beam path of the second Raman laser beam so that it travels parallel to the other beams, with a horizontal offset of 6 mm. In the first case, all beams cross the beryllium trap center co-propagating, whereas in the second case,

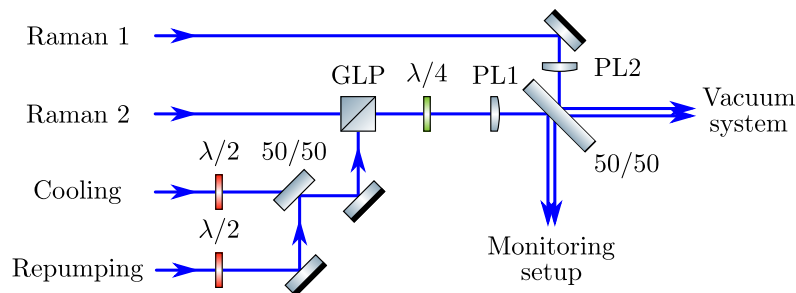


Figure 3.13: Schematic of the setup for overlapping the laser beams. See text for details. 50/50: beam splitter, GLP: Glan-laser polarizer, PL1/2: piezo actuated lens 1/2.

the in-vacuum optics guide the second Raman beam so that it crosses the other beams at a 90° angle in the center of the trap. The beam paths are shown in figures 6.1 and 6.5 in chapter 6.

The parts of the laser beams that are not sent to the vacuum system by the 2" beam splitter are used for monitoring purposes. The monitor beams are split by another 50/50 beam splitter, so that part of the laser power can be used for power monitoring with a calibrated photodiode sensor (*Thorlabs, S130VC*), while the other part is sent to a pair of beam profiling cameras (*DataRay, BladeCam-XHR*). The cameras are placed on the optical platform so that beam profiles measured at the camera positions correspond to the ones at the center of the beryllium trap.

3.4.4 Phase-lock for the Raman laser system

In contrast to the lasers for cooling and repumping, the relative phase between the two Raman lasers needs to be stabilized in order to drive coherent transition between the qubit states of $^9\text{Be}^+$. Due to the large qubit frequency of about 139 GHz at 5 T and a lack of high-speed modulators at 313 nm, an implementation of a phase lock in the UV is not feasible. Instead, we implement the phase lock using the IR laser sources. This allows us to use fast fiber-based IR modulators and photodetectors as part of the signal chain.

We lock the phase of the two 1552 nm lasers with the setup shown in figure 3.14. Therefore, we modulate the reference output of one laser, named seed laser 2, with a fiber coupled electro-optic modulator (EOM) (*EOSPACE, PM-AV5-40-PFA-PFA-SRF1W*) at a frequency close to 17.375 GHz. The required modulation signal is generated with a microwave signal generator (*Anritsu, MG3692B*) and amplified with a high power amplifier (*Mini-Circuits, ZVE-3W-183+*). The maximum power for the

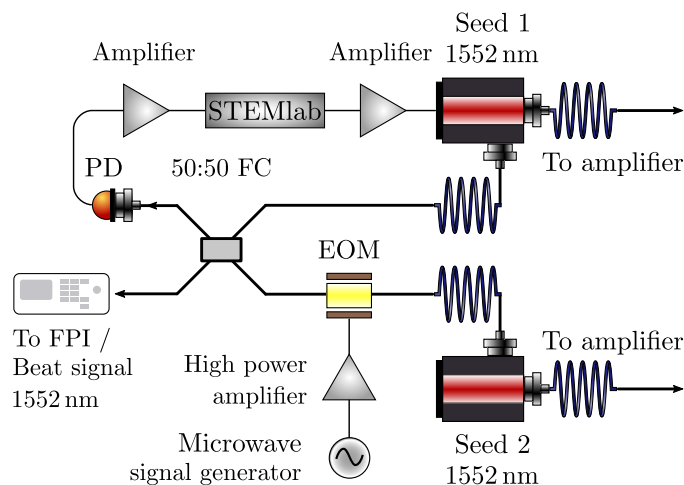


Figure 3.14: Schematic of the servo loop for the phase-lock of two 1552 nm seed fiber lasers. See text for details. FC: fiber coupler, FPI: Fabry-Pérot interferometer, PD: photodiode.

modulation is limited by the damage threshold of the EOM of 30 dBm. This allows us to maximize the fourth-order sideband component at 69.5 GHz. The other laser, named seed laser 1, is tuned close to this sideband. Both lasers are overlapped with a 2x2 fiber coupler (*Agiltron, FC-15139233*) and the beat signal is measured with a fast fiber-coupled photodetector (*Menlo system, FPD310-FC-NIR*). The photodetector has a high bandwidth of 1.5 GHz, which is useful to find the initial beat signal. The signal is amplified and fed into the input of a RedPitaya STEMLab 125-14 board, that runs a digital phase-locked loop (PLL) [79]. The board is clocked with an internal 125 MHz quartz oscillator which acts as a phase reference for the beat signal. Since the inputs are equipped with 50 MHz anti-aliasing filters, we usually phase-lock the beat signal to a fractional frequency of the oscillator of 31.25 MHz. The output of the digital controller is amplified with a fully-differential amplifier (*Texas Instruments, THS4531*) and fed back to the modulation input of seed laser 1, which closes the feedback loop of the phase lock.

To make sure that the 4th-order sideband can be generated with the setup, we measure the spectral components of the modulated laser using a Fabry-Pérot interferometer (FPI). To this end, we turn off seed laser 1 and couple the light of the output port of the fiber coupler that is not used in the feedback loop into the FPI (*Thorlabs, FPI-SA200-12B*). We scan the length of the interferometer's cavity by applying a triangular voltage to an incorporated piezoelectric actuator which in turn adjusts the position of one mirror. The FPI has an integrated photodiode detector, which we connect to an oscilloscope to measure the response of the cavity. Figure 3.15 shows exemplary sideband spectra recorded with different modulation power levels. As the FPI has a free spectral range (FSR) of 1.5 GHz, sidebands appear at positions corresponding to the modulus of their respective frequencies.

The observed sideband strengths depend on the EOM driving power and can be deduced from a Bessel function expansion of the modulated signal [80]. In our case, the 1st, 2nd, 3rd- and 4th-order sidebands are maximized at power levels of 19.0 dBm, 24.0 dBm, 26.2 dBm and 28.0 dBm for the EOM drive, respectively. Higher order sidebands are observed as well, but we are unable to maximize them, as the driving power is limited by the damage threshold of the EOM.

For the phase lock, we set the driving power to 28 dBm, which maximizes the 4th-order sideband and thus the beat signal for the digital PLL. As only the reference output of seed laser 2 is modulated, no sidebands at 17.375 GHz or multiples thereof are present in the main beam. This maintains all the amplified power in the carrier and avoids spurious transmissions, as the sidebands could be translated through the SFG and SHG setups to the UV domain.

At the same time, this poses the problem that we cannot characterize the beat signal directly, as we lack the possibility to measure a beat signal frequency of 69 GHz. Instead, we measure the beat signal with a reduced offset frequency. To this end, we turn off the microwave generator and lock both seed fiber lasers to each other with an offset of 31.25 MHz only. Although the additional phase noise introduced by the modulation source is multiplied by a factor of 4 for the 4th-order sideband, we can still neglect the omission of this component in our analysis, as

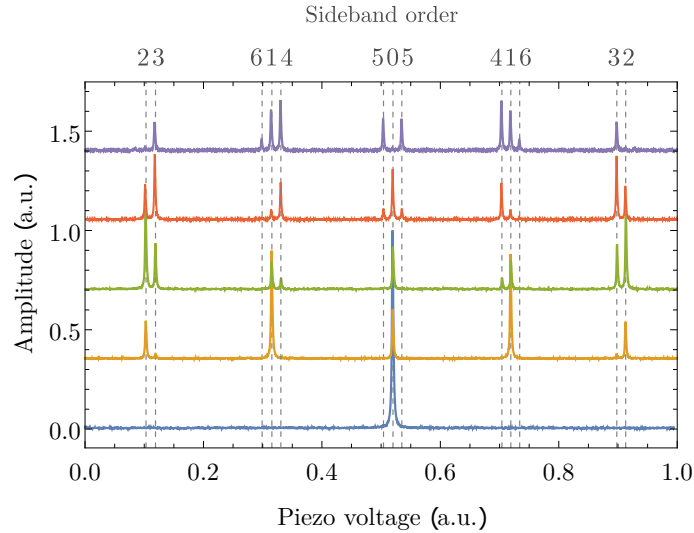


Figure 3.15: Sideband spectra at 1552 nm measured with a FPI. A resonance scan with the modulation turned off (blue) and four resonance scans at EOM driving power levels of 19.0 dBm (yellow), 24.0 dBm (green), 26.2 dBm (red) and 28.0 dBm (purple) are shown. The power levels correspond to the modulation indices that maximize the 1st-, 2nd-, 3rd- and 4th-order sideband, respectively. The amplitude scale is identical for all measurements, while the individual measurements are offset by a constant value for clarity. Grey dashed lines and labels on top indicate sideband positions and sideband orders.

fibers and mechanical vibrations are expected to introduce considerably stronger phase noise than the generator equipped with an ultra-low phase noise option causes. For example, phase noise introduced by the fibers used in the laser setups exceed the specified single-sideband (SSB) phase noise at low frequencies [81] by several orders of magnitude, as will be shown in the following. Thus, we can analyze the degradation of the phase lock throughout the setup and transfer the findings to the case with high frequency offset as well.

For the analysis, we measure the beat signal spectrum at four different positions in the setup. The first spectrum is recorded at 1552 nm. Towards this end, we connect a fiber-based photodiode to the second output of the fiber coupler that is used to overlap the reference beams of the seed lasers (see figure 3.14). This is comparable to a measurement, where the main output of both seed lasers would be overlapped prior to the fiber-based amplification. The second spectrum is recorded at 626 nm just after SFG. Both 626 nm beams are overlapped with a 50/50 beamsplitter and coupled into a fiber, which is connected to a fiber-based photodiode. For the third spectrum, we repeat this process at 313 nm just after SHG. The last spectrum is measured on the platform close to the vacuum system after the lasers have been transmitted through the UV fibers. There, we use the reference beams that are usually used to monitor the beam profiles (see section 3.4.3) and focus both of them onto a free-space photodiode with a lens. We record all spectra with a spectrum analyzer. For comparison of the main spectral features, all spectra are shown in

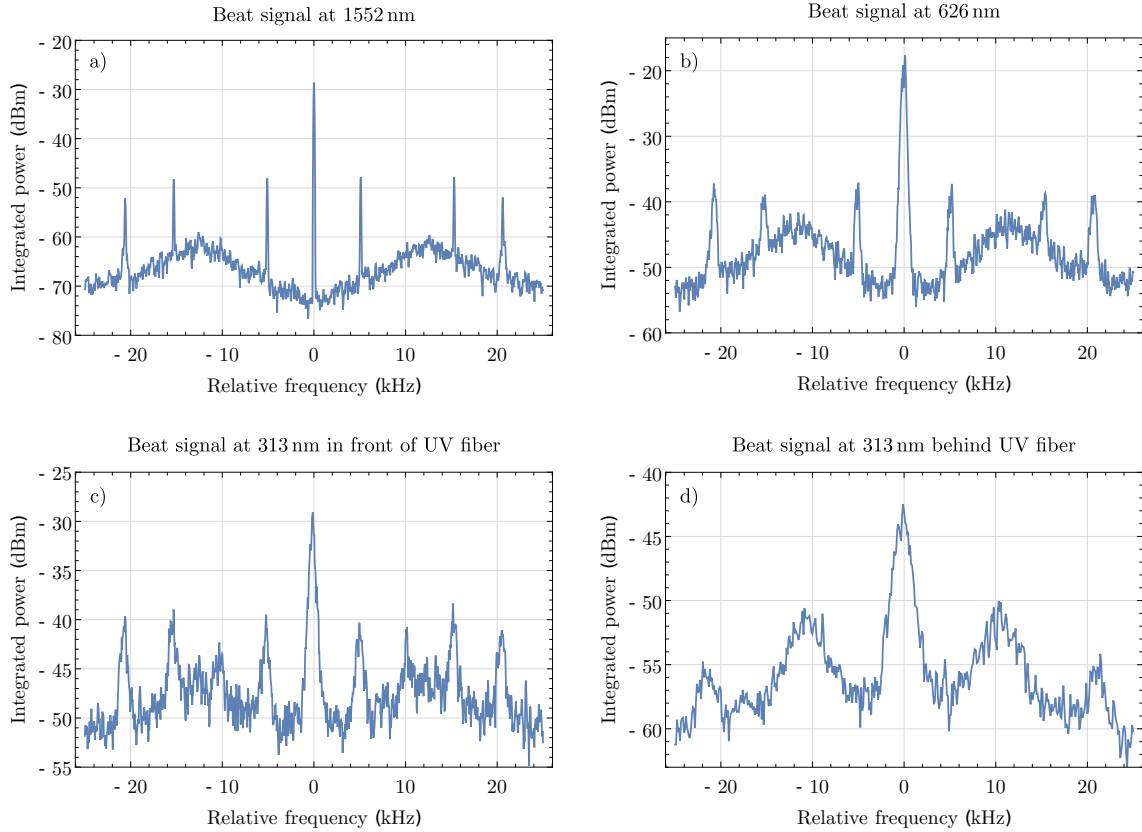


Figure 3.16: Beat signal spectra measured at 1552 nm, 626 nm and 313 nm. The frequencies are given relative to a central frequency of 31.25 MHz for the measurements at 1552 nm and 626 nm and relative to a central frequency of 62.5 MHz for the measurements at 313 nm. All spectra correspond to an average of 10 scans with a 100 Hz measurement bandwidth each.

figure 3.16.

At 1552 nm we measure a narrow central peak, whose linewidth is limited by the bandwidth of the spectrum analyzer (we measure a linewidth < 1 Hz in a separate measurement with a spectrum analyzer bandwidth of 1 Hz). In addition, broad bumps around a relative frequency of 12.6 kHz are observed. The central frequency of these so-called “servo bumps” corresponds to the case where the phase delay of the feedback signal exceeds 180° , thus marking the transition from negative to positive feedback. Furthermore we observe additional narrow sidebands at relative frequencies of 5.0 kHz, 15.3 kHz and 20.6 kHz. We attribute these to the seed lasers’ internal switching power supplies, as they are reproducible with all lasers of the same type that we own. There are seed lasers where this effect is suppressed to some extent. However, their tuning ranges do not fit the wavelength requirements for the Raman lasers and have not been used for the analysis presented here. From figure 3.16, a signal-to-noise ratio (SNR) of 19.5 dB can be inferred, where we define the SNR as the difference between the main peak and strongest parasitic sideband.

For the beat signal at 626 nm, we observe a broadened central peak with a full

width at half maximum (FWHM) of about 500 Hz. The broadening is introduced in the fiber-based amplification step, as the fibers couple the laser frequencies to the lab's thermal and acoustic environment [82]. The SFG process itself does not introduce additional phase noise, as the same 1050 nm laser is used in both cases. The same amount of broadening is observed for the parasitic sidebands, whereas the relative level of the background noise, including the servo bumps, is increased. Since the parasitic sidebands are affected in the same way as the main peak, the SNR is the same as for the measurement at 1552 nm (see figure 3.16b).

The fiber link between the SFG setups and the SHG setups introduces additional broadening. Due to the doubling of the laser frequencies, the central beat frequency is doubled to 62.5 MHz together with the widths of all spectral components. This results in a FWHM of about 1 kHz for the central peak. Furthermore, the non-linear frequency doubling process introduces additional parasitic sidebands at mixing frequencies of the already existing ones. The most prominent one is observed at a frequency of 10.3 kHz. At the same time, the SNR is reduced to 9.3 dB (see figure 3.16c).

The final spectrum, measured with two focused free space beams, corresponds to the one that would be measured at the ion position. Due to the fiber transmission at 313 nm, the central peak is broadened once more to a FWHM of 1.5 kHz. Compared to the previous measurements, the mode overlap is reduced, as the beams are not overlapped with a fiber anymore. This reduces the SNR to 7.6 dB, as the servo-bumps are lifted above the parasitic sidebands (see figure 3.16d). Figure 3.17 shows the same spectrum with a larger frequency span. Compared to the main peak we measure a drop of the background noise of 32 dB (64 dB) within a frequency span of ± 100 kHz (± 500 kHz). This behaviour can be attributed to the intrinsic low phase noise of the seed fiber lasers at 1552 nm.

The final linewidth is sufficiently small to resolve individual sidebands of single

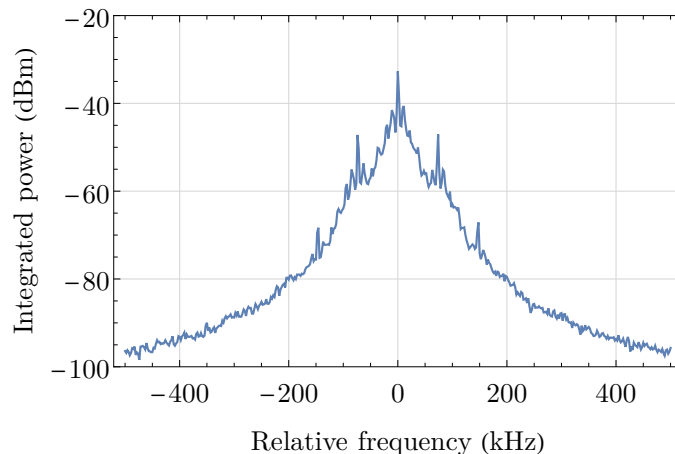


Figure 3.17: Beat signal spectra measured at 313 nm with a span of 1 MHz. The frequencies are given relative to a central frequency of 62.5 MHz. The spectrum corresponds to an average of 10 scans with a 100 Hz measurement bandwidth each.

${}^9\text{Be}^+$ ions, as typical axial trap frequencies are on the order of a few hundred kHz in our Penning trap. Within this thesis, the laser system is used for thermometry of ${}^9\text{Be}^+$ ion crystals. This corresponds to a measurement of a Doppler broadened transition with a linewidth on the order of several MHz. Since this is a relaxed requirement, no further modification of the laser system is required for this purpose.

3.4.5 Imaging and detection system

In general, fluorescence detection can be implemented either in the radial or in the axial direction of a Penning trap. In a cylindrical design, collecting the radial fluorescence light requires a hole in the ring electrode. A suitable optical system can then be used to collimate the light passing the hole and guide it out of the magnet's bore and the vacuum system. In our case, this is technically challenging, since the bore of the superconducting magnet is filled with the cryogenic support structure (see section 3.3). In addition, the design of the beryllium trap comes with a small length for the ring electrode (see section 3.2.1), which limits the possible size of the hole and leads to a poor light collection efficiency. Consequently, we decided to collect the fluorescence light from the beryllium trap along the axial direction only.

The imaging system was developed with the goal to collect as many photons as possible with a photomultiplier tube (PMT), to optimize the image quality for detection with an electron-multiplying charge-coupled device (EMCCD) camera and to enable a straight-forward adjustment. A sketch of the system is shown in figure 3.18.

A single aspheric lens is used to collect the fluorescence light from the ions and to guide it out of the vacuum system. The custom lens is made from fused silica with an AR coating for 313 nm. It is located at a distance of 18.9 mm from the center of the beryllium trap and mounted in a 9 mm aperture of the trap stack that extends up to a distance of 17.8 mm from the trap center. This geometry effectively limits the numerical aperture (NA) to 0.25, which means that 1.6% of the total fluorescence light is collected. Furthermore, the lens creates an intermediate focus 548 mm away from the lens, which can be imaged from outside the vacuum system. The light leaves the vacuum in a distance of 1042 mm from the trap center.

Outside the vacuum system, a plano-convex lens with a focal length $f = 100$ mm is used to obtain an image of the ions with six-fold magnification. The lens is placed

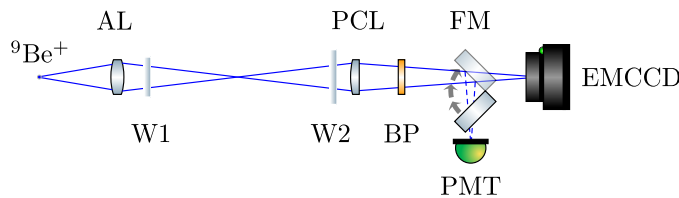


Figure 3.18: Schematic of the imaging system. See text for details. AL: aspheric lens, PCL: plano-convex lens, FM: flip mirror, W1: trap can window, W2: vacuum window, BP: bandpass filter.

close to the vacuum window in a mount that allows translation in the x -, y - and z -direction as well as tilts in the x - and y -direction to compensate misalignment of the optical system. If spatial resolution is required, the resulting image can be recorded with an EMCCD camera (*Andor, iXon A-885-KCS-VP*). If only the total fluorescence is of interest, photons can be counted with a PMT (*Hamamatsu, H8259-01*). Switching between the two detectors is possible with a motorized flip mirror mount in front of the camera. To reduce stray light, a UV bandpass filter is placed in the imaging path and the flip mirror as well as the PMT are mounted in a light tight housing. The PMT is rigidly connected to the EMCCD camera, which in turn is mounted on a 3-axis translation stage. Once the imaging system is set up, alignment of the flip mirror is not possible anymore and the positions of the two detectors are fixed relative to each other. Thus, the imaging system can only be optimized with respect to one of them. Typically, the system is optimized for maximum fluorescence detection with the PMT, with an off-centered, but sharp picture on the EMCCD camera.

It is possible to replace the plano-convex lens with a setup consisting of a second aspheric lens and a microscope objective. This enables to spatially filter the image in an additional intermediate focus plane and to increase the magnification. However, earlier measurements showed that this comes with a significant alignment overhead due to the low depth of focus and depth of field of the microscope objective as well as a detrimental reduction of the total fluorescence signal if the ion position in the trap deviates from the ideal one. Therefore, the alternative setup was not used for the measurements presented here. Details on alternative systems and the design process of the imaging optics are given in reference [41].

3.5 Experiment control

For the control of our experiment, we use the *Advanced Real-Time Infrastructure for Quantum physics (ARTIQ)* control system from *m-Labs* [83]. *ARTIQ* provides a high level programming language based on *Python*, that can be used to describe experimental sequences. The corresponding code is compiled and executed on dedicated field programmable gate array (FPGA) hardware, which enables for nanosecond timing resolution and sub-microsecond latency.

The hardware design is based on a modular approach where peripherals communicate with a core device (*m-Labs, Sinara 1123 Carrier "Kasli"*). We use hardware modules for RF frequency generation via direct digital synthesis (DDS) (*m-Labs, Sinara 4410/4412 DDS "Urukul"*), digital-to-analog converter (DAC) based voltage generation (*m-Labs, Sinara 5432 DAC "Zotino"*) and transistor-transistor logic (TTL) pulse generation and detection (*m-Labs, Sinara 2118 TTL cards*). Experiments are managed via the *ARTIQ master* program that runs on a local computer and connects to the core device via a local area network (LAN). Additional non-proprietary hardware can be controlled with the *ARTIQ master* via network or serial interfaces using a custom network device support package (NDSP). The *ARTIQ master* is in

turn controlled via the *ARTIQ dashboard*.

DC signals for trapping potentials and ion transport are generated with a self-built arbitrary waveform generator [84], the so-called “pretty darn quick” (PDQ) box. It is based on an FPGA controlled ensemble of DACs with 16-bit resolution, 50 MHz update rate and a voltage range of ± 10 V. The PDQ box is controlled with an NDSP that allows for real-time control. Voltages for selected electrodes (for example all electrodes of the beryllium trap) are amplified up to 30 V with an additional self-built amplifier. All DC signals are filtered with three cascaded first order low-pass filters, where each filter is placed at a different temperature stage. As a trade-off between noise reduction and sufficiently fast transport speed, the filter system was designed with a cutoff frequency of 1.3 kHz, which is about an order of magnitude lower than typical magnetron frequencies in our experiment.

In the beryllium trap, each segment of the ring electrode and one correction electrode are connected to an individual RF line (see Section 3.2.1). This configuration allows to excite the motion of the ions in the radial as well as the axial direction of the trap with dipole fields, while in the radial direction quadrupole fields can be used to couple the magnetron and modified cyclotron motion to each other. In the precision trap, one correction electrode and one endcap electrode is equipped with an RF line, which allows to apply dipole excitations. The RF lines are equipped with a capacitive voltage divider and an additional large 1 M Ω resistance, which reduces the effective cutoff frequency for the DC line connected to the same electrode to 1.2 kHz.

The required RF signals are generated using *Urukul*, which provides frequencies ranging from 1 MHz up to 400 MHz with power levels between -21.5 dBm and 10 dBm. Frequencies below 1 MHz may be generated with *Urukul* as well, but additional frequency dependent attenuation needs to be considered in this regime. Still, further strong attenuation is required in practice to avoid particle loss due to too high excitation amplitudes. Further excitation signals can be generated using several arbitrary waveform generators (*Keithley, 3390* and *Keysight, 33611A, 33522B*), which are controlled with custom NDSPs.

The wavelengths and frequencies of the laser systems for cooling, repumping and Raman interactions are measured and controlled using a wavemeter with 2 MHz accuracy (*HighFinesse, WSU-2*), that is frequently calibrated with a stabilized helium-neon laser (*SIOS Meßtechnik, SL 03*). The wavemeter software comes with a digital PID controller, that we either use to stabilize the laser frequencies or to apply frequency sweeps. We use an NDSP to manage the PID controller settings via ARTIQ. Furthermore, the microwave signal generator for the Raman laser phase lock is controlled with an NDSP as well. RF signals for the AOMs are generated using *Urukul* and amplified with the 10 W RF amplifiers. The setpoints of the digital PID controllers for laser power stabilization are controlled using *Zotino*. TTL signals are used to control the orientation of the flip mirror in front of the EMCCD camera and to read out the PMT counts. A schematic overview of the whole experiment infrastructure is given in figure 3.19.

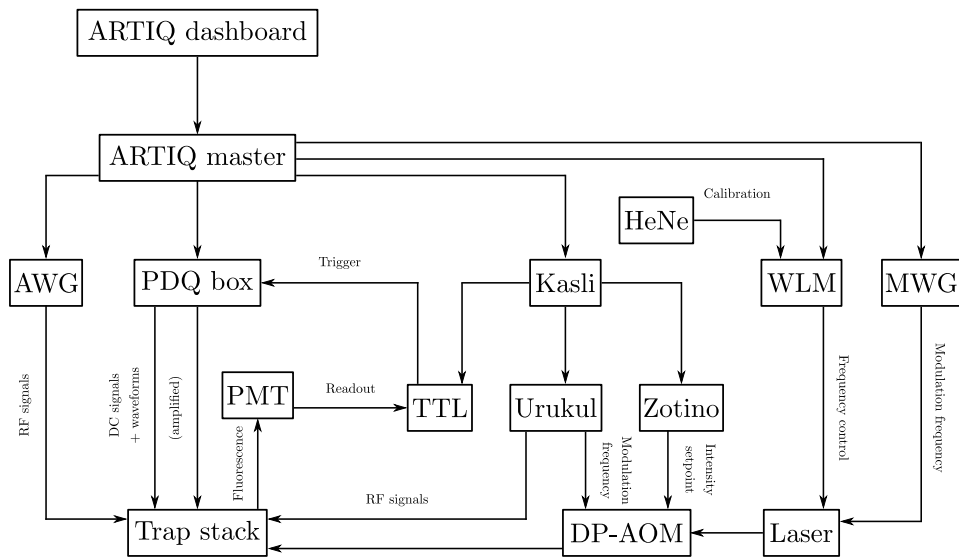


Figure 3.19: Schematic overview of experiment infrastructure. See text for details. AWG: arbitrary waveform generator, DP-AOM: double-pass AOM setup, WLM: wavemeter, HeNe: helium-neon laser, MWG: microwave signal generator.

CHAPTER 4

Particle preparation

The prerequisite for a meaningful measurement in a Penning trap is the careful preparation of the ions to be studied. Therefore, it is not only necessary to produce and trap them, but also to reduce their number as much as necessary for the particular measurement. Furthermore, appropriate cleaning of the trap is required to avoid disturbances of the measurement by trapped contaminants or ions on a high magnetron orbit. Also, it is necessary to determine the trap frequencies and the magnetic field with adequate precision for predictions about sideband and thermometry measurements and the analysis of the respective results.

In the following I will describe the loading routine (section 4.1), followed by the description of the techniques used to reduce the number of particles in the trap (section 4.2). Afterwards I will give a brief overview of techniques that we use to clean the trap in section 4.3. At last, measurements of the trap frequencies and the magnetic field as well as implications for the further measurements will be presented in section 4.4.

4.1 Loading procedure

In a cryogenic Penning trap like ours, the combination of a deep trapping potential with an ultra-low rate of background-gas collisions allows to store particles for days, months or even years [11, 85]. In the case of ${}^9\text{Be}^+$, the cryogenic vacuum also suppresses other typical degradation processes, such as hydride-ion formation [86]. Thus, it is only rarely necessary to reload our traps. Nevertheless, particle losses due to unexpected interactions with the experimental system or careless user input makes reloading necessary every once in a while.

Loading of ${}^9\text{Be}^+$ requires a two-step process consisting of the production of neutral beryllium and subsequent ionization. In our case, we use a frequency doubled Nd:YAG laser at 532 nm for the generation of a plume of beryllium atoms through ablation from a target that is embedded in one endcap of the beryllium trap (see sections 3.2.1 and 3.4.1). If the pulse energy of the laser is high enough, a part of

the ablated atoms is subsequently ionized¹ and trapped with stable orbits.

The following is a summary of our loading routine for the beryllium trap:

- **Step 0: All trap voltages are set to 0 V to eject the remaining particles.**
- **Step 1: The voltage at the ring electrode is set to -20 V and the tuning ratio for the correction electrodes is set to 0.88.** It is possible to choose a higher voltage (closer to 0 V) at the ring electrode to reduce the number of initially trapped particles. However, whenever a problem with the loading routine is detected, we switch back to -20 V, as this value has proven to be robust with regard to long-term drifts of the system.
- **Step 2: We turn on the cooling laser and apply a sawtooth ramp to its frequency.** The ramp starts with a laser detuning of -640 MHz, which is decreased until it reaches the resonance². The period of this scan is on the order of 30 s. The large detuning allows for efficient cooling of hot particles, which suffer from a large Doppler shift.
- **Step 3: A single shot of the ablation laser is fired.** We have been able to load ions with pulse energies as low as 40 μ J [39]. A reasonable pulse energy that compensates for the regular drift of the laser beam trajectory, and thus the focus on the beryllium target, lies in the range of 60 – 80 μ J.
- **Step 4: We wait for several minutes and monitor the ion fluorescence signal on the EMCCD camera.** A very bright signal with constant amplitude or erratic behavior tells us that the ion cloud is too large and requires the ejection of particles in order to enable efficient laser cooling. If instead we see a rise of the signal that corresponds to the frequency ramp of the cooling laser, this tells us that the ion cloud is cooled sufficiently and localized in the trap center. Particle ejection and cleaning routines can now be applied in order to prepare the ions for a measurement.

In principle, it is possible to load single ions directly by using a photoionization laser, which eliminates the need for subsequent particle ejection. Although a laser system for resonant two-photon ionization was built and implemented initially [39, 87, 88], it turned out that it is associated with a large experimental overhead and problems during daily operation. For this reason, the laser system was dismissed and not used throughout this thesis. Instead, we resorted to several routines for particle ejection and trap cleaning, which will be described in the following sections.

¹ The details of the ionization mechanism are unknown so far.

² The resonance of the cooling transition is always assumed at a frequency of $957.466\,924$ THz during the loading procedure.

4.2 Particle ejection

Particle ejection is necessary to extract a small ion cloud or single ions out of an initially large ion cloud. Different approaches can be pursued and combined to reach this goal. During my time at the experiment we implemented three different methods to reduce the number of particles: evaporative reduction, pulsing of the trap potential and splitting in a double-well potential. In the following I will describe these methods briefly.

Evaporative reduction of the particle number

A straightforward way to reduce the number of confined particles is to lower the trap potential until ions with a high kinetic energy are able to escape. It can be applied directly after ion loading to discard very hot trapped particles. However, it is not useful if the ions have already been laser cooled for a long time and thus are strongly localized in the trap center. In this case, the atoms will only leave the trap if the potential is very shallow, which entails the risk of losing the whole ensemble.

We typically apply a maximum voltage on the order of -1 V to the ring electrode during the evaporation routine, while the tuning ratio on the correction electrodes is kept constant.

Pulsing the trap potential

Another routine to reduce the number of ions is based on grounding of trap electrodes for a short time. Without axial confinement, the Coulomb repulsion leads to an explosion of the trapped particles, and some ions, preferably those on high magnetron orbits, escape from the trap [89].

To this end, we adiabatically transport the ions to the ring electrode of the proton trap (see section 3.2.2). This electrode is designed to deflect the beam of the electron gun in order to hit an off-axis target for the creation of protons in the future [68]. Due to the high voltage requirements of the intended application, the electrode is currently not equipped with RC filters and thus allows fast pulsing of the applied voltage. If the ions are confined with this electrode only, it is possible to pulse the overall trap potential with a single TTL switch.

Unfortunately, it turned out that this method is not reliable, as the optimal pulse length seems to depend on parameters which we cannot measure reliably, such as the cloud size. As the loss of all ions at once is likely with this routine if the wrong parameters are chosen, it was dismissed for the recent measurements.

Splitting the particles with a double-well potential

Our most commonly used routine for particle number reduction is based on dividing the trapped ions into two parts with the help of a double-well potential. One part is

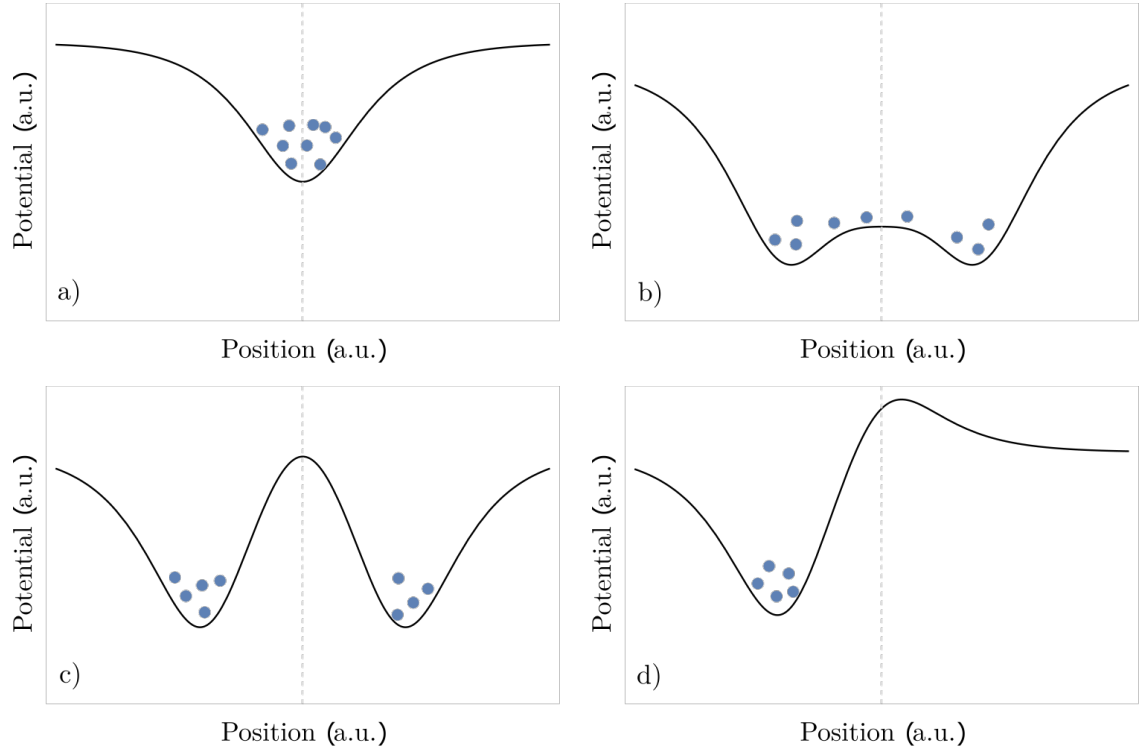


Figure 4.1: Axial potential shapes during the splitting procedure. Beryllium ions are represented by large blue dots. a) initial trap potential, b) double-well potential with shallow barrier, c) double-well potential with strong potential wedge, d) potential shape after the release of a part of the ions. See text for details.

kept, while the other part is dismissed from the trap. This scheme is based on the ideas presented in reference [90] and was adapted to our experiment [41].

In the beryllium trap, the double-well potential for the splitting routine is generated with continuous voltage ramps that are applied to the five electrodes. We start with a harmonic potential generated with a ring electrode voltage of $V_R = -20$ V and a tuning ratio $TR = 0.88$ for the correction electrodes, while the endcaps are held at ground (figure 4.1a). In a first step, we ramp down both endcap electrodes to -30 V. This effectively creates a double-well potential with a shallow barrier in the center, which allows the ions to spread out (figure 4.1b). In a second step, the ring electrode voltage is increased to 25 V, while the correction electrodes are ramped up to 0 V. This creates a potential wedge that separates the ions into two independent parts (figure 4.1c). In the third step, one of the endcap electrodes is ramped up to 0 V, thus releasing the corresponding part of the ions (figure 4.1d). In a last step, all electrodes are ramped back to their initial values. Each step is a linear ramp performed within 250 ms, resulting in a total time of 1 s for the complete routine.

Figure 4.2 shows images of ion ensembles of different sizes that can be produced with these reduction schemes. For a low number of ions, discrete levels of the fluorescence signal are observed, which allow to determine the exact number of ions. Although we are able to produce single ions, all measurements in this thesis were

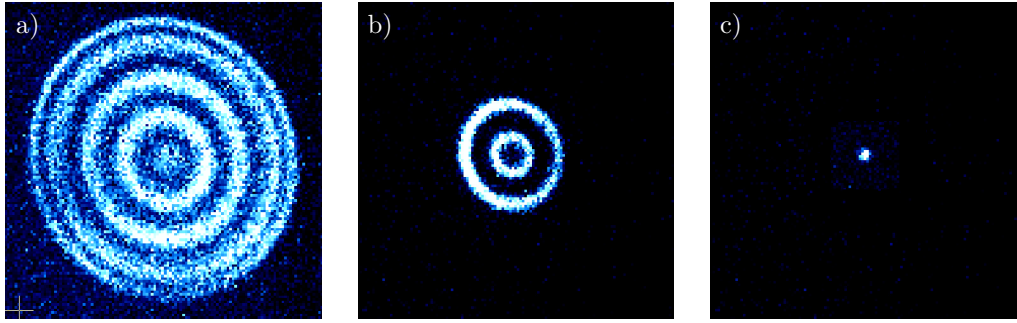


Figure 4.2: Images of ion ensembles of different sizes. The ions were imaged along the axial direction with the EMCCD camera. The ring structure is observed because the ion cloud rotates with a period that is much shorter than the exposure time of the camera. (a) medium size ion cloud with four rings around a central bright spot (b) small size ion cloud with two rings and no central spot (c) single ion.

carried out with medium or small size ion clouds. The reason for this is an unstable fluorescence signal that can be observed for ion clouds with less than seven particles. The frequency and duration of this dropouts do not follow any discernible pattern [39].

In the last months of my time in the laboratory, the hypothesis of dropouts due to transitions to a dark state which is not part of the cooling cycle [41] could be ruled out with the implementation of the repumping laser. This suggests that the fluorescence dropouts are caused by individual ions leaving the field of view of the imaging system for a limited period of time. A possible reason for this behavior could be magnetron heating caused by fluctuations of the cooling laser parameters. Since the gradient cooling scheme sensitively depends on the offset of the laser position from the trap center, beam pointing fluctuations may play a role. For this reason, custom mounts for fiber couplers and highly stable stainless-steel mirror mounts (*Thorlabs, POLARIS-K1S4*) were implemented on the laser beam delivery platform. In addition, all other optic mounts were replaced by mounts which minimized the required degrees of freedom and possible movements. Still, vertical drifts of the laser position at the reference positions of the beam profiling cameras on the order of a few tens of μm are observable on a timescale of about two hours. To further reduce the drifts, active beam stabilization is being considered for the future. In addition, we consider the idea of mode cleaning optics for the cooling beam, as the beam at the trap center does not correspond to an ideal Gaussian beam, which is assumed for theoretical predictions. The non-Gaussian beam profiles are caused by the photonic crystal fibers and additional aberrations, which are introduced due to the required large beam diameter on the laser beam delivery platform. The topic of magnetron heating remains the subject of future investigations.

Nevertheless, it is also possible that other, so far unidentified, mechanisms are causing the unstable fluorescence signal. One such contributing mechanism could be identified in the last months of my time in the laboratory: ions on high magnetron orbits. This insight led to the implementation of several cleaning procedures, which

will be described in the next section.

4.3 Cleaning methods

Cleaning the trap of unwanted ions is an important part of particle preparation. Although we cannot detect the presence of contaminants such as protons or helium ions with our system directly, the BASE experiment at Mainz has shown that it is possible to load a small number of protons through ablation from a beryllium target and subsequent cleaning of the trap [30]. Since they use the same loading technique as we do, this suggests that in our setup at least some protons are produced by ablation along with the beryllium ions as well.

Furthermore, Penning trap experiments with laser cooled ${}^9\text{Be}^+$ ions usually suffer from hydride-ion formation [86]. When this happens, the heavier BeH^+ ions are separated from the lighter ${}^9\text{Be}^+$ ions due to the centrifugal force caused by the rotation of the ion cloud. As our system does not offer the possibility for imaging along the radial direction, we cannot detect the centrifugal separation directly. As an alternative, it is possible to measure the decay of the total fluorescence signal of the ${}^9\text{Be}^+$ ions due to defect formation over time [91]. However, since no problems related to a decrease in the signal have been observed with particles trapped for time scales up to several weeks so far, no precise measurement of this type has been performed. Nevertheless, defect formation of hydride ions cannot be ruled out completely.

In contrast, one type of contaminant that we can detect with our system are beryllium ions on high magnetron orbits. These typically manifest themselves in an unstable fluorescence signal, if the size of the cloud in the center of the trap is small. Sometimes a collapse of one ion towards the trap center can be observed, which leaves a typical fingerprint in the fluorescence signal. This consists of a fluorescence dropout, followed by a rapid spike and an increased signal after a settling time on the order of a second.

The following cleaning methods have been implemented in our experiment to avoid disturbances due to contaminants of any kind during a measurement.

RF excitation

For a contamination species with known mass, it is possible to remove it from the trap with an RF pulse with constant frequency and high amplitude. If the pulse is applied at the contaminants' axial or magnetron frequency, while the beryllium ions are laser cooled at the same time, the contaminants are resonantly excited until they separate from the ions in the trap center. Subsequently, they are removed from the trap, either because their kinetic energy exceeds the trapping potential, or because their magnetron orbit is increased so much that they hit an electrode surface. This technique can be combined with an evaporative reduction of the particle number to ensure that excited ions leave the trap.

SWIFT cleaning

An extension of the RF pulse based cleaning approach is called stored waveform inverse Fourier transform (SWIFT) cleaning. The method is based on the generation of tailored waveforms that are applied to a trap electrode with an arbitrary waveform generator. Here, the Fourier transformed spectrum of the waveforms corresponds to a sum of frequency bands with sharp edges. This allows to address multiple frequency bands, and thus to excite different contaminant species at the same time, while the frequency bands containing resonances of ${}^9\text{Be}^+$ are cut out. Details on the generation of the required waveforms are described in reference [92].

Aperture cutoff

A rather simple approach to clean the trap of ions on high magnetron orbits is based on the transport through an electrode with a small diameter. If the magnetron orbits are as big as or bigger than the electrode diameter, particles will hit the surface of the electrode and thus will be removed from the trap. For the implementation of this scheme, we use one electrode of the proton source, which has a diameter of 4 mm, whereas the diameter of the electrodes in the beryllium trap is 9 mm. To increase the efficiency of method, we combine it with RF or SWIFT cleaning pulses, which increase the magnetron orbits of the excited particles.

The combination and frequent repetition of multiple steps for particle number reduction and subsequent cleaning of the beryllium trap allows for the preparation of a pure and strongly localized ${}^9\text{Be}^+$ ion cloud that can be used for precision measurements. Due to the high vacuum quality, it is usually not necessary to clean a once prepared cloud again at a later time.

4.4 Measurement of the trap frequencies

The starting point for many measurements in Penning traps is an accurate knowledge of the trap frequencies. For example, if we want to apply the RF cleaning pulses that have been described in the previous section, we need to know the trap frequencies of the contaminants in advance. In this thesis, we are interested in performing thermometry measurements with an ion cloud. Here, the axial trap frequency is required for the calculation of the Lamb-Dicke parameter (see equation 2.27), which yields useful information for the comparison of the Raman resonances obtained with and without interaction with the axial motion of the ions. Furthermore, the trap frequencies can be used to calculate the magnetic field, which in turn allows the calculation of frequency shifts within the level structure of ${}^9\text{Be}^+$. As long as the level structure is not known with sufficient precision, we cannot even tune the lasers to the involved transition frequencies.

We measure the trap frequencies as follows. We prepare an ion cloud in the beryllium trap and cool it with the cooling laser with a fixed detuning of -10 MHz

relative to the resonance frequency, which is determined by a measurement as described in section 5.1. Next, we deactivate the cooling laser and shine in an RF pulse with a frequency close to the trap frequency that we want to investigate. Depending on the detuning of the pulse, it will excite the ion motion with a certain probability. For detection, we turn on the cooling laser again and collect the fluorescence light with the PMT. If the frequency of the RF pulse was close to resonance and the ions have been heated, this will result in an increased Doppler shift during detection. Thus, the number of detected photons will decrease in comparison to the case of large RF detuning. We repeat this scheme consisting of initial cooling, excitation and subsequent detection for different RF frequencies to obtain a resonance curve of the trap frequency.

For a measurement of the axial trap frequency, a pre-cooling time of 300 ms before each excitation pulse is chosen to ensure that successive pulses do not influence each other. The RF pulse is generated with *Urukul* and applied to one correction electrode of the beryllium trap. Each pulse has a length of 13 ms and is attenuated by 60 dB before reaching the vacuum feedthroughs (30 dB set in the *Urukul* settings and additional 30 dB introduced with fixed attenuators). Afterwards the fluorescence light is collected for 12 ms with the PMT. The averaged result¹ of 20 individually scanned resonance spectra for a ring electrode voltage $V_R = -20$ V is shown in figure 4.3.

With a Gaussian fit to the data we obtain a central frequency $\nu_z = 435.792(1)$ kHz

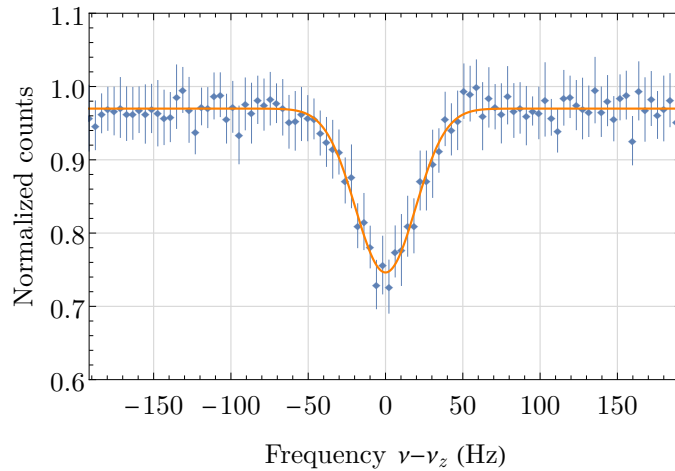


Figure 4.3: Measurement of the axial frequency. The normalized PMT counts are shown as a function of the applied RF frequency. The blue data points and error bars correspond to an average of 20 individual scans. The solid orange line is a fit of a Gaussian profile to the data. The RF frequencies are given relative to the central frequency $\nu_z = 435\,792$ Hz of the fit.

¹ All resonance spectra shown in this thesis are normalized to the maximum PMT counts of the respective averaged spectrum.

and a FWHM $\Delta\nu_z = 46(3)$ Hz. This can be compared with earlier measurements with the same setup [41], which have determined a C_2 parameter of $17\,639\text{ m}^{-2}$ for equation 2.16. For the ring electrode voltage used here, this evaluates to an axial trap frequency of 437.720 kHz . The deviation of the recent measurement in comparison with this value is on the order of 2 kHz and can have several reasons. A possible explanation is given by further findings presented in the same reference. Asymmetries in the trapping potential were observed, which are probably introduced by one segment of the ring electrode that is not properly connected to its RF line. This leads to an energy-dependent correction for the trap frequencies [43]. Depending on the cloud size and the pre-cooling time in between the RF pulses, different trap frequencies can be observed. As we do not have the possibility to determine the cloud size in a quantitative way, no detailed comparison is possible. Nevertheless, it is reasonable to use long pre-cooling times in between the RF pulses to minimize energy dependent shifts and broadening effects, as was done in the measurement presented here.

For a measurement of the modified cyclotron frequency with the same ring electrode voltage, the same procedure is repeated, with the difference that the RF pulses are applied to one segment of the ring electrode. Again, a pre-cooling time of 300 ms is used and the length of the RF pulses is 13 ms . A total attenuation of 78.5 dB is used (18.5 dB set in the *Urukul* settings, 60 dB introduced with fixed attenuators). The fluorescence light is collected for 12 ms as before. The averaged result of 20 individually scanned resonance spectra is shown in figure 4.4. We obtain a central frequency of $\nu_+ = 8491.033(1)\text{ kHz}$ and a FWHM of $\Delta\nu_+ = 42(3)\text{ Hz}$ from a Gaussian fit to the data. The deviation in comparison with earlier measurements can be explained by the fact that the modified cyclotron frequency depends on the

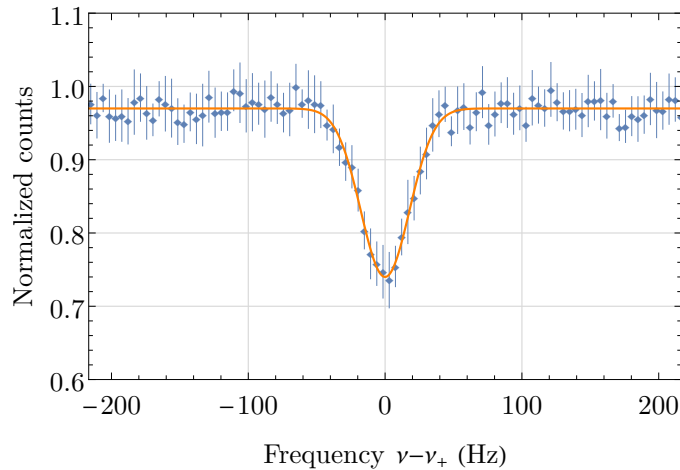


Figure 4.4: Measurement of the modified cyclotron frequency. The normalized PMT counts are shown as a function of the applied RF frequency. The blue data points and error bars correspond to an average of 20 individual scans. The solid orange line is a fit of a Gaussian profile to the data. The RF frequencies are given relative to the central frequency $\nu_+ = 8\,491\,033\text{ Hz}$ of the fit.

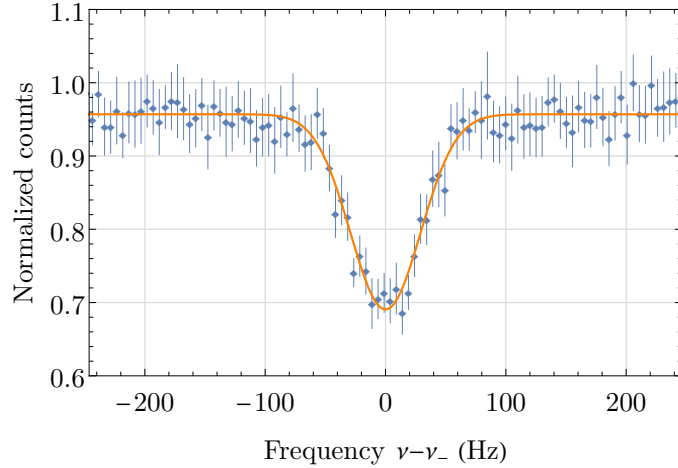


Figure 4.5: Measurement of the magnetron frequency. The normalized PMT counts are shown as a function of the applied RF frequency. The blue data points and error bars correspond to an average of 20 individual scans. The solid orange line is a fit of a Gaussian profile to the data. The RF frequencies are given relative to the central frequency $\nu_- = 11\,154\text{ Hz}$ of the fit.

axial trap frequency (see equation 2.7), where a deviation was found already.

For a measurement of the magnetron frequency, we need to modify the generation of the RF pulses, since *Urukul* is not able to generate the required frequency directly. Instead we connect two outputs of the same *Urukul* board to a mixer (*Mini-Circuits, ZAD-6+*) and filter the output with a fifth-order low pass filter with a cut-off frequency of 50 kHz (*Thorlabs, EF124*) and an additional low pass filter with a cut-off frequency of 1.9 MHz (*Mini-Circuits, BLP-1.9+*). This way, the resulting frequency is determined by the frequency difference of the two initial *Urukul* signals. The signal is split with a power splitter (*Mini-Circuits, ZFSC-2-1+*) and applied to two opposite segments of ring electrode. The pre-cooling time, length of the RF pulses and the readout time are chosen as before. The ring electrode voltage is set to -20 V . The averaged result of 20 individually scanned resonance spectra is shown in figure 4.5. A Gaussian fit to the data yields a central frequency $\nu_- = 11.154(2)\text{ kHz}$ and a FWHM of $\Delta\nu_- = 69(5)\text{ Hz}$.

Determination of the free cyclotron frequency and the magnetic field

We can use the invariance theorem (equation 2.10) to calculate the free cyclotron frequency with the results from the previous section. This results in a frequency $\nu_c = 8502.216(42)\text{ kHz}$. For this value, we obtain a magnetic field $B = 4.989\,772(25)\text{ T}$, making use of equation 2.4. This is a deviation of about 10 mT from the expected value of 5 T, but in accordance with earlier results [41].

The value of 5 T stems from the specification of the manufacturer and a measurement with a nuclear magnetic resonance (NMR) magnetometer that was carried out after the superconducting magnet had been energized and shimmed in 2015 [39].

However, since the calibration of the magnetometer had expired at the time of the measurement, it cannot be guaranteed that this value corresponds to the actual one. On the other hand, the invariance theorem used for the calculation of the magnetic field is exact only for single particles [93]. For more than one particle, higher-order effects due to particle-particle interaction not covered by the invariance theorem can falsify the result. Therefore, the value calculated here should also be treated with caution.

For the anticipated thermometry and sideband measurements, this uncertainty is problematic. A magnetic field deviation of 10 mT corresponds to a shift of the qubit frequency on the order of a few hundred MHz. This must be put in relation with the expected linewidth for the stimulated Raman transitions on the order of a few kHz for measurements without interaction with the axial motion. Without prior knowledge about the relevant experimental parameters for the Raman laser system, finding the resonance for the first time becomes a Sisyphean task. Furthermore, the optical transition frequencies are shifted on the same order of magnitude. This impedes the correct addressing of the repumping transition, which is necessary for high fidelity state preparation of the ions in a single quantum state.

To resolve this issue, we decided to experimentally determine the relevant optical resonance frequencies of ${}^9\text{Be}^+$ in our system. The corresponding measurements are described in the next chapter.

CHAPTER 5

Measurements of optical resonance frequencies

The basis for every laser based cooling, manipulation or detection routine is the knowledge of the involved optical resonance frequencies with adequate precision. For example, imprecise addressing of the resonances can lead to infidelities during state preparation or to an undesired increase of the final particle temperature after cooling. This chapter describes how we have determined the relevant optical resonance frequencies of ${}^9\text{Be}^+$ in our system. To this end, we have implemented different types of resonance measurements based on fluorescence detection, which will be described in the following.

The resonance measurements can be distinguished by the number of involved lasers. Section 5.1 describes the procedure for a measurement of the resonance frequency of the cooling transition, which requires only a single laser. In addition, more involved resonance measurements with two or three lasers, to which we refer as double and triple-resonance measurements, are introduced in sections 5.2 and 5.3. The results of the measurements will be summarized in section 5.4.

5.1 The cooling transition

A particularly convenient property of ${}^9\text{Be}^+$ is the fact that in a Penning trap, a closed cooling cycle can be implemented in a straightforward way. Due to the simple level structure, the gradient cooling technique described in section 2.3 can be realized with a single laser tuned below the resonance frequency between the ${}^2S_{1/2} |m_J = +1/2\rangle$ and the ${}^2P_{3/2} |m_J = +3/2\rangle$ state, without the need for an additional repumping laser¹. We can then use the PMT or the EMCCD camera to monitor the fluorescence signal of the ions.

Still, if we want to determine the central frequency and the linewidth of the cooling

¹ Off-resonant excitations will effectively trap a small amount of the population in the ${}^2S_{1/2} |m_J = -1/2\rangle$ state [39, 53]. This effect is partly suppressed through the choice of our laser polarization. However, for an ion cloud, it will only lead to a relative decrease of the fluorescence signal. For that reason, it will be neglected here.

resonance, we encounter two problems. The first problem is that as soon as we change the frequency of the cooling laser, the cooling parameters change and thus the temperature of the ions is not constant during the measurement. This in turn affects the shape of the resonance curve due to a change of the corresponding Doppler shift. The second problem is that the magnetron motion is heated as soon as we reach the line center, which will increase the trajectory of the ions until they eventually leave the region of the beryllium trap that is observable with the imaging system. An interpretation of the resulting profile can become difficult.

As an example, we record a resonance with a medium size ion cloud¹. For the measurement, the cooling laser beam is sent through the beryllium trap at an angle of 45° relative to the trap axis and offset from the trap center in the vertical direction. A vertical beam waist of 155 μm, a horizontal beam waist of 270 μm and a power of 278 μW is used². Initially, the offset in the vertical direction is adjusted for a fixed detuning of the cooling laser, until a stable fluorescence signal and a constant spatial distribution is observed with the EMCCD camera. For the measurement, a sawtooth frequency sweep with a frequency range of 60 MHz and a period of 20 s is applied to the laser frequency. The maximum frequency is chosen so that the sweep just covers the expected resonant frequency to minimize heating of the magnetron motion. Every 100 ms the laser frequency is readout with the wavemeter³ and the fluorescence light of the ions is collected with the PMT for 12 ms. Figure 5.1 shows the averaged result of six individual frequency scans.

From low to high laser frequencies, the fluorescence signal increases, until a sharp drop at a frequency $\nu_0 = 957.466\,932(1)$ THz is observed. At this point, the magnetron motion is heated so much, that the ions leave the field-of-view of the imaging optics. Thus, it indicates the resonance frequency of the cooling transition. However, the absolute frequency of the transition is hard to determine, as the ion cloud is rotating. Depending on its size and its rotation frequency, additional Doppler shifts are introduced. Since we cannot measure the cloud size and the rotation frequency is not constant during the measurement, it is hard to pin down a frequency and a corresponding uncertainty. We have observed comparable drops of the fluorescence signal in a range of frequencies between 957.466 924 THz and 957.466 934 THz in the past.

From the measurement presented here, we cannot infer reliable information about

-
- 1 As we cannot determine the number of ions precisely, we roughly categorize them by the number of observable rings. See figure 4.2 in chapter 4 for a comparison of different cloud sizes.
 - 2 The beam waists and power levels at the position of the ions are estimated from the reference measurements described in section 3.4.3. In the case of the power levels, a fixed conversion factor is determined experimentally, which enables us to calculate the power of a laser beam in front of the vacuum window. About 75 % of this power is transmitted to the ions in the beryllium trap.
 - 3 This is necessary because of a variable timing offset between the start of the measurement sequence through ARTIQ and the start of the frequency sweep through the wavemeter PID regulator. For this reason, the data points in figure 5.1 are provided with an error bar for the frequency.

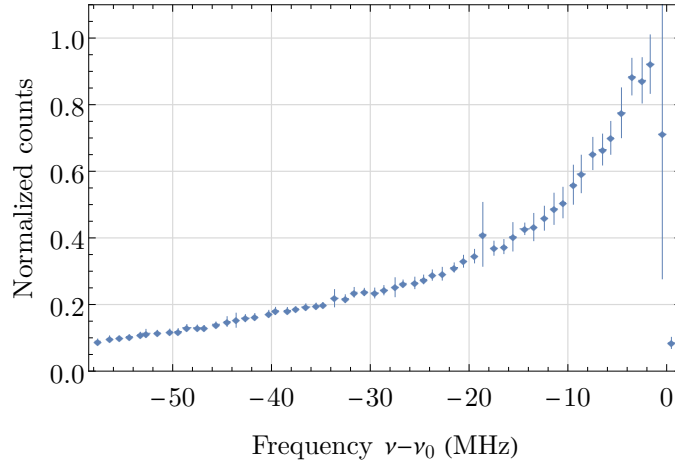


Figure 5.1: Resonance measurement of the cooling transition. The normalized PMT counts are shown as a function of the applied laser frequency. The blue data points and error bars correspond to an average of six individual scans. The laser frequencies are given relative to the frequency $\nu_0 = 957.466\,932$ THz, at which a sharp drop of the fluorescence signal is observed. The blue-detuned side of the resonance was not scanned, as the ions are heated strongly and leave the observable region of the trap as soon as the resonance is exceeded.

the linewidth and thus the temperature of the ion cloud, as the recorded resonance (excluding the points where no fluorescence signal is observed) does not follow the usual Voigt profile. Obtaining a reliable lineshape is possible with a careful division of the measurement into cooling and detection steps with individual laser power levels and detunings [41]. Nevertheless, with this measurement method it is not possible to measure the resonance frequency with a higher accuracy than is the case with the measurement described above. For this reason, the above value is taken as the best approximation of the actual resonance frequency.

5.2 Double-resonance measurements

With two lasers, more involved techniques can be used to measure other optical resonance frequencies of ${}^9\text{Be}^+$. If one laser is addressing the cooling transition and constantly scattering photons, then the second laser can be used to disturb the system by pumping the ions to states, which do not participate in the cooling cycle. In this way, a decay of the fluorescence signal is detectable, which allows us to draw conclusions about the resonance addressed with the second laser. We refer to this technique as a double-resonance measurement.

In the following, we assume that the cooling laser is tuned slightly to the red of the transition between the ${}^2S_{1/2} |m_J = +1/2\rangle$ and ${}^2P_{3/2} |m_J = +3/2\rangle$ states. If we excite an ion with a second “probe” laser to the ${}^2P_{3/2} |m_J = +1/2\rangle$ state, it decays to the ${}^2S_{1/2} |m_J = -1/2\rangle$ state with a probability of $1/3$ and thus leaves the cooling cycle. On the other hand, if the ion decays back into the ${}^2S_{1/2} |m_J = +1/2\rangle$ state, it

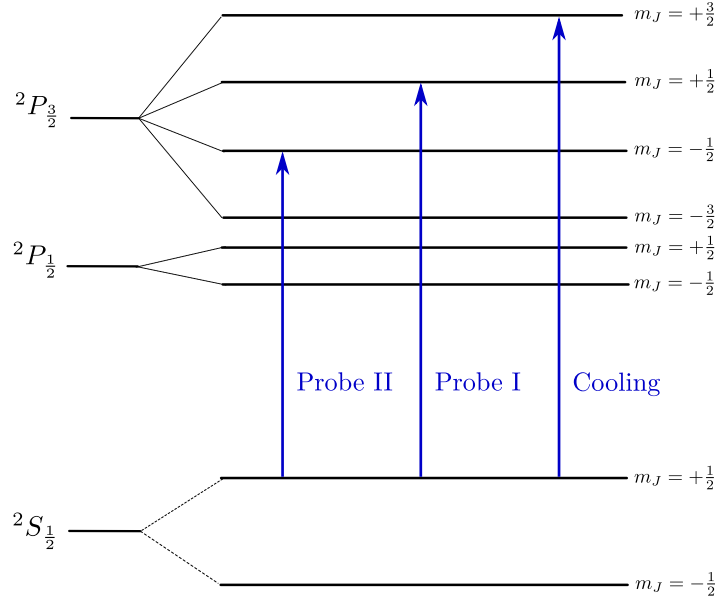


Figure 5.2: Energy level diagram and relevant transitions for double-resonance measurements. Transitions for cooling and probing the ions are shown. Only levels with $m_I = +3/2$ are depicted.

is excited by the probe laser again and the process is repeated, until it eventually leaves the cooling cycle as well. After a certain time, all ions will have left the cooling cycle. The speed of the corresponding decay of the fluorescence signal depends on the detuning of the probe laser from the transition, and thus its excitation rate. Therefore, measuring the resonance frequency of the probe transition is possible by measuring the decay as a function of the probe laser frequency [53].

In case of an excitation to the $2P_{3/2} |m_J = -1/2\rangle$ state, the same mechanism applies, but the probability for a decay to the $2S_{1/2} |m_J = -1/2\rangle$ state is $2/3$, and thus the decrease of the fluorescence signal is more pronounced for the same laser parameters. To better distinguish the different transitions, we refer to the transition between the $2S_{1/2} |m_J = +1/2\rangle$ and $2P_{3/2} |m_J = +1/2\rangle$ states as “probe transition I”, and to the transition between the $2S_{1/2} |m_J = +1/2\rangle$ and $2P_{3/2} |m_J = -1/2\rangle$ states as “probe transition II”. All transitions are shown in figure 5.2.

For the following measurements, we set the cooling laser frequency to a fixed detuning of about -10 MHz relative to the resonance frequency, which was measured before. This corresponds roughly to half of the transition’s natural linewidth of 19.6 MHz and thus prepares the ions at a temperature that is close to the Doppler limit (see section 2.3). As before, the vertical offset of the cooling beam is adjusted until a stable fluorescence signal and a constant spatial distribution is observed with the EMCCD camera. The power of the cooling laser is fixed at $123 \mu\text{W}$, which together with the given beam waists corresponds approximately to the transition’s saturation intensity [94].

For a measurement of the resonance frequency of probe transition I, the probe

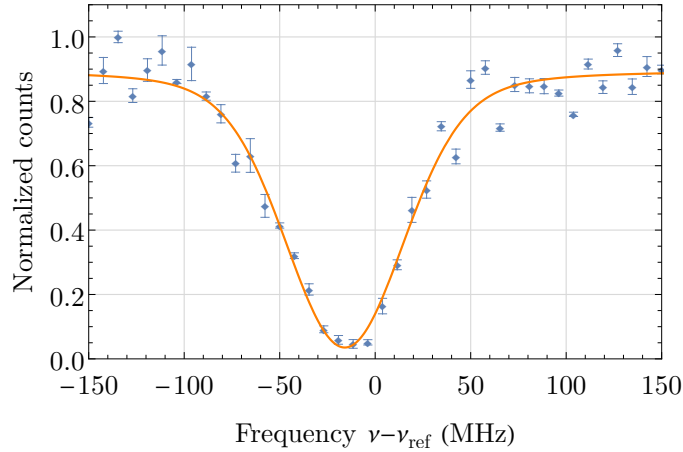


Figure 5.3: Double-resonance measurement for probe transition I. The normalized PMT counts are shown as a function of the applied laser frequency, which is given relative to the reference frequency $\nu_{\text{ref}} = 957.378\,630$ THz. The blue data points and error bars correspond to an average of three individual scans. The solid orange line is a fit of a Voigt profile to the data.

laser beam is overlapped with the cooling laser beam. Its beam waist is set to $135\,\mu\text{m}$ in the horizontal and $115\,\mu\text{m}$ in the vertical direction. The laser power is set to $3\,\mu\text{W}$ and the beam is prepared with p-polarization. The procedure for a single resonance scan is as follows. The ion cloud is initialized with the cooling laser for 2 s. Afterwards, the cooling laser is turned off and the probe laser is applied for $20\,\mu\text{s}$, which pumps part of the ions to the dark state. For detection, the cooling laser is turned on again and the fluorescence light is collected for 12 ms with the PMT. This procedure is then repeated with different probe laser frequencies. The comparably large time step for initialization of the ions is required to repump the ions to the $^2S_{1/2} |m_J = +1/2\rangle$ state. Furthermore, it allows the Hänsch-Couillaud lock of the probe laser's SHG cavity to relock after coarse changes of the laser frequency via the wavemeter PID regulator. These are necessary, since a random ordering of the probe laser frequencies is used for the measurement. Frequency changes from one data point to the next can easily exceed 100 MHz. The averaged result of three individual measurements is shown in figure 5.3. For the measurement, we define an arbitrary reference frequency $\nu_{\text{ref}} = 957.378\,630$ THz, close to which we expect the actual probe transition frequency.

From the fit of a Voigt profile to the data, we obtain a central frequency that is shifted by $-16(3)$ MHz from the reference frequency and an FWHM of $75(8)$ MHz. Both parameters depend on the interaction with the rotating ions and thus on the vertical position of the probe beam relative to the ion cloud. To analyze this behavior in detail, we repeat the measurement for different vertical positions of the probe laser beam. Figure 5.4 shows the dependence of the central resonance frequency and of the FWHM on the vertical laser beam position.

A linear dependence of the shift of the central resonance frequency on the vertical laser beam position is observed. From the linear fit shown in figure 5.4a we obtain

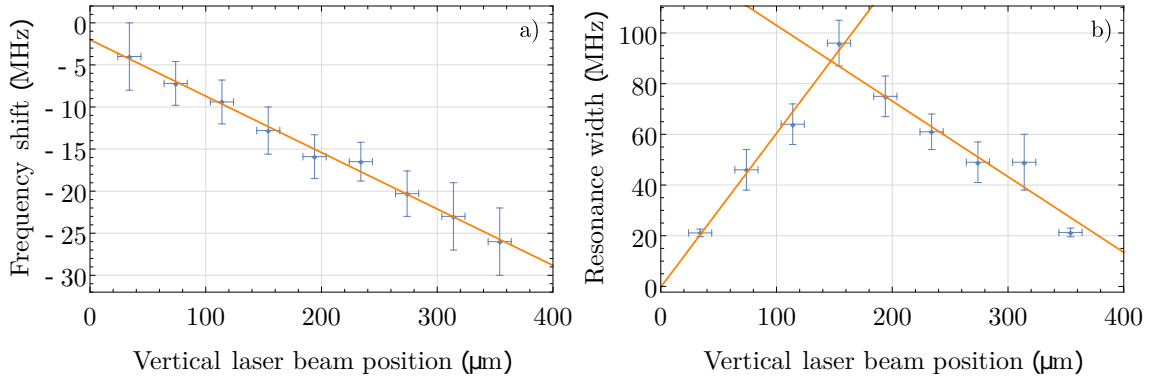


Figure 5.4: Dependence of the observed resonance frequency of probe resonance I on the laser beam position. Left: Dependence of the central resonance frequency on the vertical laser beam position. The resonance frequency is given as a frequency shift relative to the reference frequency $\nu_{\text{ref}} = 957.378\,630$ THz. The laser beam positions must be understood as relative measures, as they are not referenced to an absolute position. Right: Dependence of the FWHM on the vertical laser beam position. Solid orange lines are linear fits to the data. See text for details.

a gradient of $-67(5)$ kHz/ μm . Reference [53] describes a procedure, which uses this value to determine the rotation frequency of the ion cloud. This is possible because the observed frequency dependence results from an additional Doppler shift due to the rotation. However, we cannot apply this procedure here, as the central assumption, that the probe laser beam diameter is much smaller than the spatial distribution of the ion cloud, is not fulfilled.

We can see this by looking at the dependence of the FWHM of the measurements on the vertical laser beam position (see figure 5.4b). As is also laid out in reference [53], the effective width of the resonance depends on the natural linewidth of the transition, Doppler broadening due to the ion temperature and an additional Doppler broadening due to the rotation of the ion cloud and the finite laser beam diameter. For the case of a probe beam waist that is much smaller than the ion cloud, the resonance width is expected to be constant and independent of the laser beam position. In contrast, we observe a maximum FWHM at a vertical laser beam position $y = 154\,\mu\text{m}$ and a decrease of the width towards higher and lower positions. As a guide to the eye, two linear functions are fitted to the data points on the left hand side and the right hand side of the maximum, from which one can see that the corresponding gradient depends on the direction in which the position of the laser beam changed.

This behavior can be explained if a cloud diameter on the order of the probe laser beam diameter is assumed. In this case, the resonance width depends on the velocity spread of the particles that interact with the laser. If the laser beam fully overlaps with the ion cloud, it interacts with all ions and thus the velocity spread is maximal, while a partial overlap corresponds to a reduced spread and thus a reduced linewidth. Because the beam shape is not symmetric with respect to its center-of-intensity, the observed gradient depends on the direction in which the beam is moved.

The linear fits overlap at a laser beam position of $y = 147(40) \mu\text{m}$, which we attribute to the position where the overlap of the laser beam with the ion cloud is maximal. This position is our best estimate on the vertical position of the trap center, at which the Doppler shift due to the rotation of the ion cloud is minimized. If we evaluate the linear fit of figure 5.4a at this position, we obtain a frequency shift of $-12(3)$ MHz corresponding to an absolute value of $957.378\,618(3)$ THz.

Without a measurement of the rotation frequency, we are unable to determine the plasma parameter and the ion temperature as introduced in section 2.2. Although it is also possible to obtain the rotation frequency from cloud aspect ratio measurements [95], we are unable to do so, as we lack the possibility to image the ion cloud along the radial direction. The reason for these difficulties is that our apparatus was designed as a single-ion experiment and was not intended to be used with ion clouds. Nevertheless, the double-resonance measurement allows us to determine the resonance frequencies of the probed transition with sufficient accuracy. We thus repeat the resonance measurement for probe transition II.

The same experimental parameters are used as before. As we do not adjust the polarization of the probe laser to a circular one, the higher probability for a decay to the dark state is compensated by a lower excitation probability, and thus no adjustment of the laser power is necessary. For the measurement, a reference frequency of $\nu_{\text{ref}} = 957.286\,702$ THz is assumed. Figure 5.5 shows the dependence of the central resonance and the FWHM on the vertical laser beam position.

As before, a linear dependence of the frequency shift on the vertical laser beam position is obtained. The gradient is determined from the linear fit in figure 5.4a to be $-62(8)$ kHz/ μm . This is compatible with the value measured using probe transition I, although we cannot measure or control the absolute cooling beam

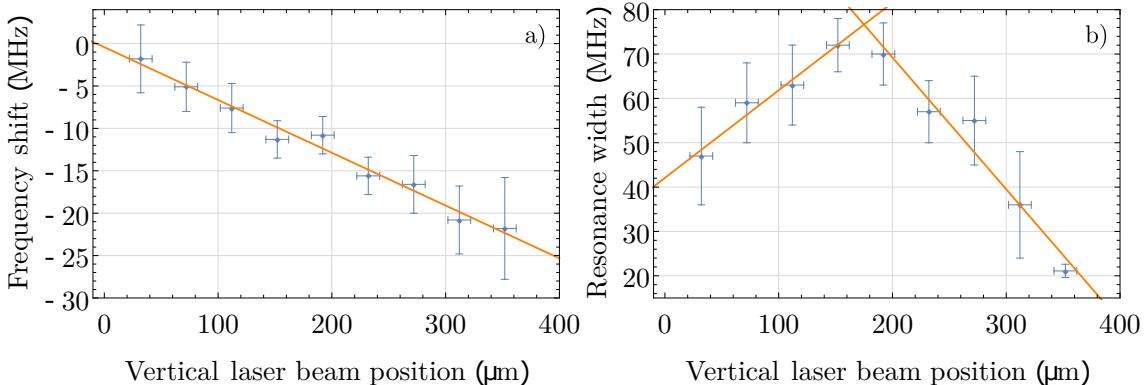


Figure 5.5: Dependence of the observed resonance frequency of probe resonance II on the laser beam position. Left: Dependence of the central resonance frequency on the vertical laser beam position. The resonance frequency is given as frequency shift relative to the reference frequency $\nu_{\text{ref}} = 957.286\,702$ THz. The laser beam positions must be understood as relative measures, as they are not referenced to an absolute position. Right: Dependence of the FWHM on the vertical laser beam position. Solid orange lines are linear fits to the data. See text for details.

position and thus the rotation frequency, which determines the gradient. Two linear fits to the left and right half of the data points of figure 5.4b yield a crossing at a vertical laser beam position $y = 175(46) \mu\text{m}$. Evaluating the linear fit of figure 5.4a at this position yields a frequency shift of $-11(3) \text{ MHz}$ and a corresponding absolute value of $957.286\,691(3) \text{ THz}$.

5.3 Triple-resonance measurements

The previous measurements can be expanded by introducing a third laser, which allows us to address the resonance frequencies of transitions that bring the dark ions back into the cooling cycle. In this way, monitoring the increase of the fluorescence signal allows us to draw conclusions about the resonance addressed with the third laser. We refer to this technique as triple-resonance measurement.

In the following, we refer to the transition between the states ${}^2S_{1/2} |m_J = -1/2\rangle$ and ${}^2P_{3/2} |m_J = +1/2\rangle$ as “repumping transition I” and to the transition between the states ${}^2S_{1/2} |m_J = -1/2\rangle$ and ${}^2P_{3/2} |m_J = -1/2\rangle$ as “repumping transition II”. The transitions are shown in figure 5.6. If we excite an ion that is in the ${}^2S_{1/2} |m_J = -1/2\rangle$ state by applying a laser that is resonant with one of these transitions, it will either decay into the bright ${}^2S_{1/2} |m_J = +1/2\rangle$ state or back into the dark state. In the latter case, it will be excited again by the repumping laser and the process is repeated. After a certain time, all ions will have been repumped into the cooling cycle.

For the measurement, we set the power of the the cooling laser to $123 \mu\text{W}$ and tune

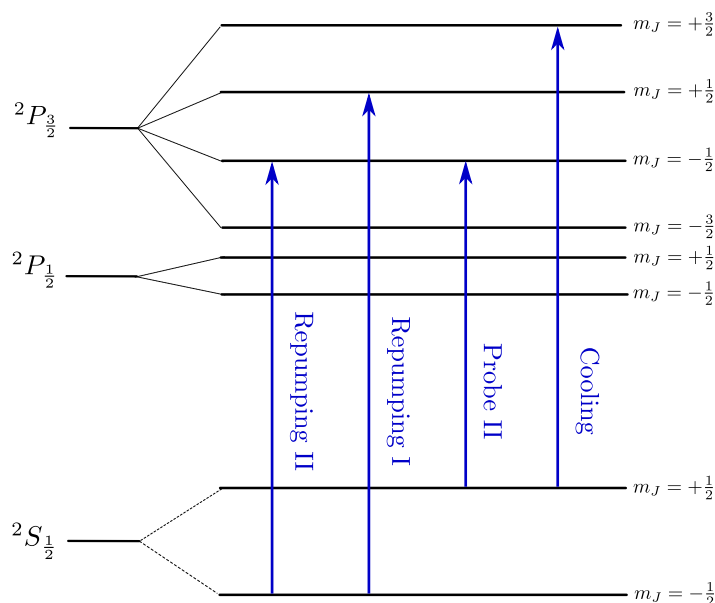


Figure 5.6: Energy level diagram and relevant transitions for triple-resonance measurements. Transitions for cooling, probing and repumping the ions are shown. Only levels with $m_I = +3/2$ are depicted.

its frequency to 10 MHz below resonance. The probe laser beam is aligned to the trap center and tuned to the resonance frequency of probe transition II, where both parameters have been determined with measurements as described in the previous section. The power of the probe laser is fixed at $3\ \mu\text{W}$. The third laser beam is overlapped with the probe laser beam and tuned close to a repumping transition.

The measurement procedure for determining the resonance frequency of repumping transition I is as follows. The beam waist of the third laser is fixed to $240\ \mu\text{m}$ in the horizontal and $80\ \mu\text{m}$ in the vertical direction. The laser power is set to $3\ \mu\text{W}$ and the polarization is chosen to be left circular to maximize the excitation probability. The ion cloud is initialized with the cooling laser for 2 s. Afterwards, the cooling laser is turned off and the probe laser is applied for $20\ \mu\text{s}$. Next, the probe laser is turned off and the repumping laser is applied for $20\ \mu\text{s}$. Finally, the cooling laser is turned on and the fluorescence light is collected for 12 ms with the PMT. The procedure is repeated for different frequencies of the repumping laser. The averaged result of three individual measurements is shown in figure 5.7.

We obtain a central frequency $\nu = 957.517\,502(1)\ \text{THz}$ and an FWHM of $\nu = 71(3)\ \text{MHz}$ with the fit of a Voigt profile to the data. Due to the overlap with the probe laser beam, it is reasonable to assume that the repumping laser beam is aligned so that it crosses the trap center and it is not necessary to repeat the measurement for different vertical laser beam positions. However, it must be taken into account that this position is subject to an uncertainty, which in turn is connected to a Doppler shift because of the rotation of the ions. Thus, it is reasonable to assume the same $\pm 3\ \text{MHz}$ frequency uncertainty that was obtained for the probe transition frequencies, which must be added to the uncertainty from the fit.

We repeat the same measurement procedure for repumping transition II. Because

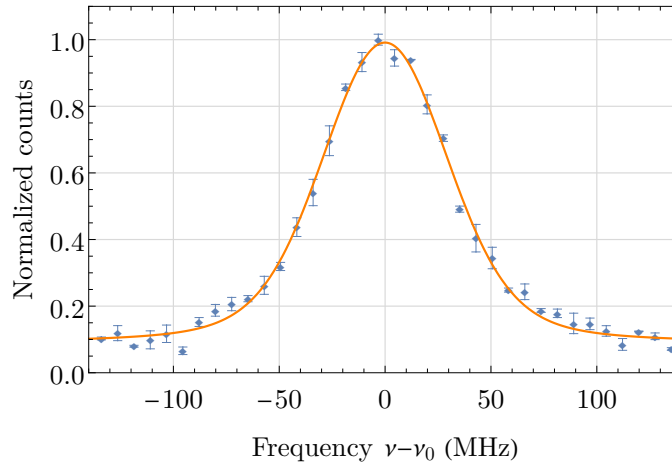


Figure 5.7: Triple-resonance measurement for repumping transition I. The normalized PMT counts are shown as a function of the applied laser frequency. The blue data points and error bars correspond to an average of three individual scans. The solid orange line is a fit of a Voigt profile to the data. The laser frequencies are given relative to the central frequency $\nu_0 = 957.517\,502\ \text{THz}$ of the fit.

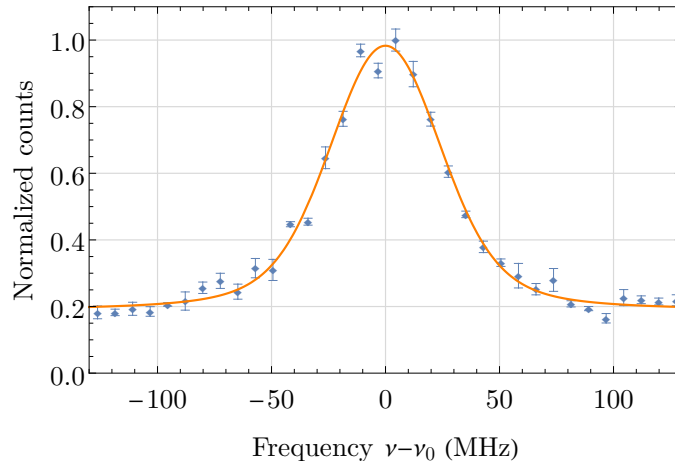


Figure 5.8: Triple-resonance measurement for repumping transition II. The normalized PMT counts are shown as a function of the applied laser frequency. The blue data points and error bars correspond to an average of three individual scans. The solid orange line is a fit of a Voigt profile to the data. The laser frequencies are given relative to the central frequency $\nu_0 = 957.425\,578$ Hz of the fit.

of wavelength tuning limitations, we switch to a different UV laser, which we can tune close to the desired transition. The laser comes with a symmetric beam waist of $145\,\mu\text{m}$ for both the horizontal as well as the vertical direction. Its power is set to $2\,\mu\text{W}$ for the measurement and p-polarization is chosen. Again, we overlap the laser beam with the probe laser beam to ensure that it crossed the trap center. Figure 5.8 shows the averaged result of three individual measurements. A Voigt fit yields a central frequency $\nu = 957.425\,578(1)$ THz and an FWHM of $\nu = 59(4)$ MHz. As before, an additional uncertainty of the resonance frequency on the order of ± 3 MHz needs to be taken into account due to the position uncertainty relative to the trap center.

5.4 Summary of the measured transition frequencies

The frequency measurements presented in this chapter provide us with all the relevant information that we need for cooling, probing and repumping ${}^9\text{Be}^+$ ions in our Penning trap. The results of the frequency measurements are summarized in table 5.1.

With the repumping frequencies known, we are now able to prepare the ions in the ${}^2S_{1/2} |m_J = +1/2\rangle$ state with high fidelity. Furthermore, we can determine the resonance frequency of the qubit transition with these results. We can calculate the frequency either by taking the difference between the frequencies of probe transition I and repumping transition I or the difference of the frequencies between probe transition II and repumping transition II. The results are frequencies of

Table 5.1: Summary of the measured transition frequencies.

Transition	Frequency	Uncertainty
Cooling	957.466 932 THz	-
Probe I	957.378 618 THz	± 3 MHz
Probe II	957.286 691 THz	± 3 MHz
Repumping I	957.517 502 THz	± 4 MHz
Repumping II	957.425 578 THz	± 4 MHz

138 884(7) MHz and 138 887(7) MHz, which are compatible with each other within the uncertainty ranges. Indeed, addressing the transition with a phase-locked laser system that is tuned close to this frequency difference allows us to drive stimulated Raman transitions. The results of these measurements are presented in the next chapter.

CHAPTER 6

Stimulated Raman transitions and thermometry of ${}^9\text{Be}^+$

In this chapter, the functionality of the Raman laser system is demonstrated with first measurements based on stimulated Raman transitions. These measurements can be divided into two categories, depending on the way in which the Raman laser beams are aligned in the beryllium trap. In the first case, both Raman laser beams are overlapped, which suppresses the interaction with the motion of the ions and allows for a high precision measurement of the qubit frequency. The corresponding measurements are presented in section 6.1. In the second case, the measurements are carried out with crossed Raman laser beams, which enables the interaction with the axial motion. Thermometry measurements carried out in this configuration are presented in section 6.2.

6.1 Measurements with co-propagating Raman laser beams

To locate the Raman resonance in the first place, we overlap both Raman laser beams and send them through the center of the beryllium trap as shown in figure 6.1. In this way, the interaction with the ion motion is reduced, as the wave vector difference between the beams and thus the effective photon recoil is minimized.

For the following measurements, we choose a detuning of $\Delta \approx 20$ GHz for Raman laser I relative to repumping transition II and for Raman laser II relative to probe transition II (see figure 6.2). Furthermore, the phase stability of the Raman lasers is ensured with the setup described in section 3.4.4. We prepare Raman laser I with a horizontal beam waist of $180\ \mu\text{m}$, a vertical beam waist of $110\ \mu\text{m}$ and p-polarization. Raman laser II is prepared with a horizontal beam waist of $160\ \mu\text{m}$, a vertical beam waist of $80\ \mu\text{m}$ and right circular polarization. Because the beams are propagating with an angle of 45° relative to the direction of the magnetic field, the overlap of p-polarization with π -polarization is smaller than the overlap of right circular polarization with σ^- -polarization in the reference frame of the ions. To compensate this effect, we set the power of Raman laser beam I to $3.2\ \text{mW}$ and the power of Raman laser beam II to $1.2\ \text{mW}$.

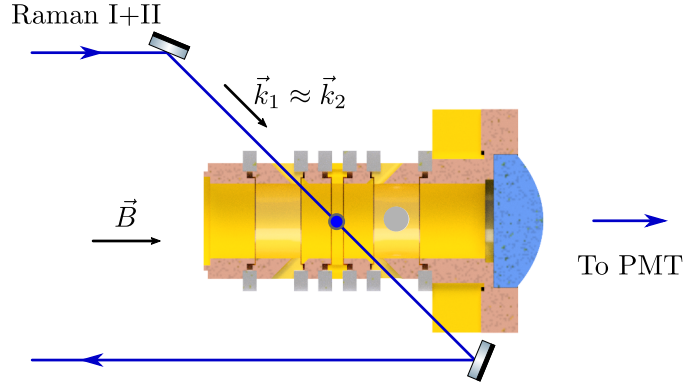


Figure 6.1: Laser beam setup for co-propagating Raman beams in the beryllium trap. Both Raman lasers are aligned with the laser beams for cooling and repumping. This setup leads to a negligible wave vector difference between the Raman lasers. Some components for this drawing were taken from reference [70].

6.1.1 Qubit frequency

For the measurement of the qubit frequency, we use a cooling and a repumping laser to prepare the ions in the ${}^2S_{1/2} |m_J = +1/2\rangle$ state. The former laser is tuned 10 MHz below the cooling resonance and the latter is resonant with repumping resonance I. The length of the preparation step is set to 75 ms to ensure that consecutive measurements are independent of each other. In a second step, we turn off the cooling and repumping lasers and apply both Raman lasers for 75 μs . This transfers part of the population to the ${}^2S_{1/2} |m_J = -1/2\rangle$ state, with a probability that depends on the detuning of the Raman laser frequency difference ν_R from the qubit transition frequency. In the final step, we shine in the cooling laser for 12 ms and detect the fluorescence light with the PMT. The sequence is repeated with different detunings from the qubit transition, where we use an AOM for an adjustment of the frequency difference ν_R . An averaged result of 20 individual measurements is shown in figure 6.3.

A Gaussian fit yields a central resonance frequency of 138 887.380(12) MHz with an FWHM of 178(29) kHz. The result for the central frequency is compatible with the calculations of section 5.4. However, due to the narrower linewidth of the Raman transition, a measurement resolution on the order of kHz is achieved here. In this case, residual AC Stark shifts limit the absolute accuracy. As the laser beam positions are not stabilized with respect to the trap center, the observed shifts differ between individual measurements.

The measured linewidth is more than an order of magnitude larger than expected from the fundamental limit due to the finite Raman laser pulse length. Furthermore, we observe a dependence of the resonance width on the number of ions and the radial spread of the ion cloud. The fewer ions are used for the measurement and the smaller their spatial distribution, the smaller becomes the resonance width. This behavior is possibly caused by a combination of the following effects. First, a

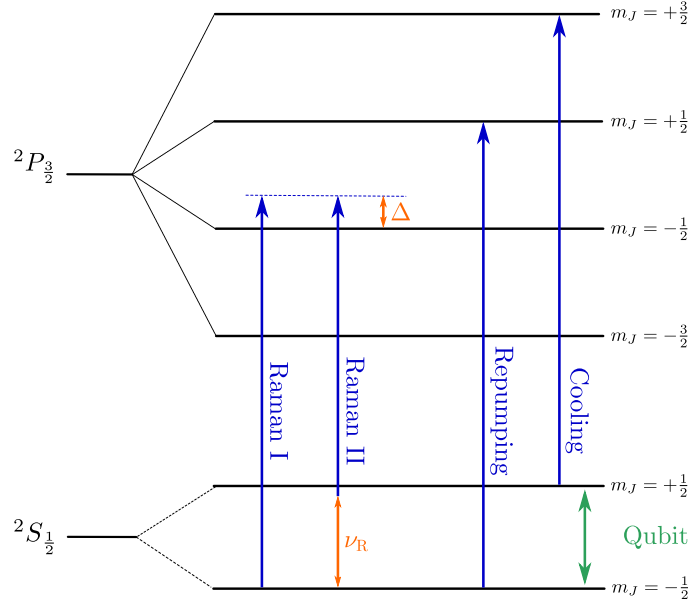


Figure 6.2: Energy level diagram and relevant transitions for stimulated Raman transitions. The ${}^2P_{1/2}$ manifold is not shown for clarity and only levels with $m_I = +3/2$ are depicted.

magnetic field inhomogeneity along the spatial distribution of the ions can contribute to the linewidth. The more ions are part of the cloud, the larger is the region of the trap that is probed during a measurement. In turn, the bigger becomes the spread of the ions' resonance frequencies. Second, the residual wave vector difference of the Raman laser beams leads to a Doppler shift that depends on the cloud's rotation frequency and the position of the individual ions in the cloud. Ions on the outer trajectories will experience a stronger shift, due to their higher velocity. Third, we know that the beam diameters of the Raman lasers are on the order of the cloud diameter. Thus, the laser power is not constant along the cloud and the ions will experience individual AC Stark shifts. This effect is further enhanced by residual drifts of the beam positions during a resonance measurement.

Recently, my colleagues were able to repeat this measurement with single ions. Due to the considerably smaller spatial distribution and the omission of the rotation of the cloud, the influence of the effects mentioned above were minimized and a linewidth on the order of 10 kHz was achieved. Challenges and prospects for measurements with single ions are described in section 7.2.1.

6.1.2 Coherence time

For a measurement of the coherence time, the population transfer as a function of the Raman laser pulse length was measured. A similar measurement routine as before was used, with the difference that the frequency difference between the Raman lasers was set to the central qubit resonance frequency, and the pulse length was scanned

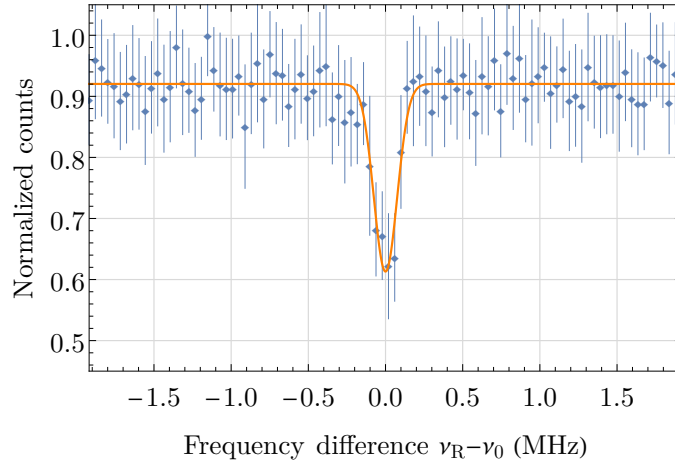


Figure 6.3: Measurement of the qubit frequency. The normalized PMT counts are shown as a function of the laser frequency difference between the Raman lasers. The blue data points and error bars correspond to an average of 20 individual scans. The solid orange line is a fit of a Gaussian profile to the data. The frequency differences are given relative to the central frequency $\nu_0 = 138\,887.380$ MHz of the fit.

instead. Figure 6.4 shows the the averaged result of 20 individual measurements.

No Rabi oscillations can be observed. The fast decay of the collective coherence is expected, since the large linewidth of the qubit resonance corresponds to a broad distribution of the contributing Rabi frequencies among the ion cloud. A simple exponential fit results in a decay time of $\tau_{\text{dec}} \approx 4 \mu\text{s}$, which agrees with the observed order of magnitude of the FWHM of the resonance measurement. Higher coherence times and first signals of Rabi oscillations were observed in the measurements with a

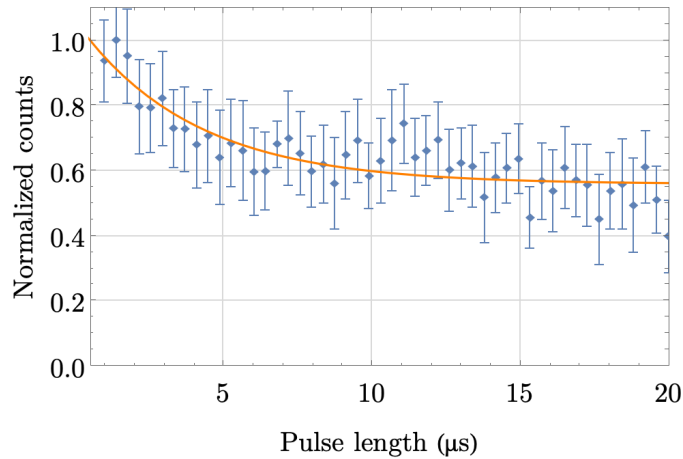


Figure 6.4: Measurement of the coherence time. The normalized PMT counts are shown as a function of the applied Raman laser pulse length. The blue data points and error bars correspond to an average of 20 individual scans. The solid orange line is a fit of an exponential function to the data. The fit includes an offset to correct for background counts and yields a decay time of about $4 \mu\text{s}$.

single ion carried out by my colleagues recently.

6.1.3 Conclusion for the magnetic field

We can use the results of the previous sections to determine the magnetic field with high precision. Using the Breit-Rabi formulae from appendix A and assuming that the broadening of the resonance is caused exclusively by magnetic field inhomogeneities, we obtain a value of 4.989 225(6) T. This value is close to the one obtained from the trap frequency measurements in section 4.4 and confirms the hypothesis of a magnetic field that is lower than the value specified by the manufacturer.

The explanation of this deviation is not straightforward. A distortion of the magnetic field in the beryllium trap could be caused, for example, by the presence of the ferro-magnetic nickel plating of the trap electrodes. Since we are unable to distinguish a broadening of the resonance frequency due to magnetic field inhomogeneities from effects due to the residual Raman laser wave vector difference and the variation of the laser power along the ion cloud, further investigations with a single ion and a modification of the experimental setup are required for a quantitative characterization.

6.2 Measurements with crossed Raman laser beams

For thermometry measurements, we align both Raman laser beams such that they cross in the center of the beryllium trap as shown in figure 6.5. The orientation of the laser beams is chosen such that a wave vector difference along the magnetic field is produced. This leads to an effective photon recoil along the axial direction, while the interaction with the orthogonal radial motional degrees of freedom is minimized.

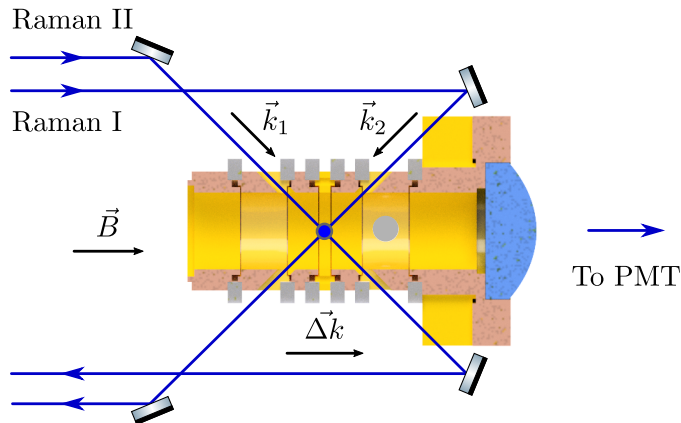


Figure 6.5: Laser beam setup for crossed Raman beams in the beryllium trap. Both Raman lasers intersect at the trap center under an angle of 90° , which leads to an effective wave vector difference along the trap axis. Some components for this drawing were taken from reference [70].

For the Raman laser beam that does not follow the cooling and repumping beams on their way through the trap, a new strategy for alignment was developed, as it could not be overlapped with an existing beam. For a coarse adjustment of the laser beam position, we tune Raman laser I close to the cooling resonance and use the fluorescence signal of the EMCCD camera as a reference signal. As soon as an image is obtained, we optimize the laser beam position with the same routines that are used for the optimization of the cooling laser position (see section 5.1). At this position, we tune the laser frequency back to the one required for the stimulated Raman transition and check if we are able to drive the Raman resonance. The laser beam is then moved until the drop of the fluorescence signal is maximized for a given set of Raman laser parameters. Once a good position is obtained, the reference position of Raman laser I on the laser beam delivery platform is recorded with a beam profiling camera. If the beam setup is changed from crossed beams to co-propagating beams and back, this reference position is used as an initial guess, which simplifies the realignment.

6.2.1 Axial thermometry measurements

Since we are using an ion cloud for the thermometry measurements, we expect a high number of motional degrees of freedom, that cannot be resolved by means of sideband spectroscopy. As described in section 2.4, we expect a Doppler broadened spectrum instead. Thus we can use the FWHM $\Delta\nu$ of the resonance to calculate the ion temperature via¹

$$T = \frac{m\lambda^2 \Delta\nu^2}{8 \ln 2 k_B}, \quad (6.1)$$

where m is the beryllium mass, λ the Raman laser wavelength and k_B the Boltzmann constant.

For a measurement of the axial mode temperature we use the same laser parameters and the same routine as for the measurement of the qubit frequency, but need to increase the Raman laser pulse length to 500 μs , which is an increase of a factor ≈ 6.7 . This is necessary to compensate for the reduced coupling strength introduced through the coupling with the axial motion, as described by equation 2.29. Figure 6.6 shows the averaged results of 20 individual measurements.

The Gaussian fit yields a central resonance frequency of 138 911.81(8) MHz with an FWHM of 9.60(27) MHz. Using equation 6.1, we calculate a corresponding axial mode temperature of 1.77(10) mK. This is a factor ≈ 3.5 higher than the theoretical Doppler limit of 0.5 mK. There are several possible reasons why the temperature is higher than expected. One is the uncalibrated shift of the cooling laser detuning due to the rotation of the ion cloud. Another reason could be heating due to trap imperfections, which have been observed in the setup before [41]. The

¹ In general, this equation is only valid if both laser beams cross at an angle of 90° .

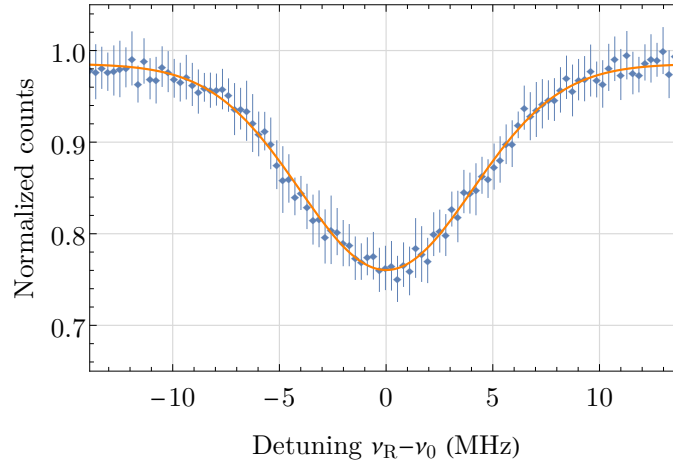


Figure 6.6: Raman resonance measurement with crossed Raman lasers. The normalized PMT counts are shown as a function of the laser frequency difference between the Raman lasers. The blue data points and error bars correspond to an average of 20 individual scans. The solid orange line is a fit of a Gaussian profile to the data. The frequency differences are given relative to the central frequency $\nu_0 = 138\,911.81$ MHz of the fit.

lowest possible temperature after Doppler cooling is desirable because the lower the initial temperature is, the easier and more effective the subsequent sideband cooling becomes. A quantitative analysis of these effects is planned for measurements with single ions.

In comparison with the measurement of section 6.1.1, we observed a shift of the central frequency by ≈ 24 MHz. The shift is reproduced in all measurements with crossed Raman laser beams and corresponds to a change of the magnetic field on the order of $900 \mu\text{T}$. More recent measurements performed by my colleagues showed that this shift was permanent. The central frequency of the latter measurements can be reproduced independent of the optical path of the Raman lasers. We suspect small mechanical changes within the experimental setup due to a failure of the air conditioning system as the cause. Such a failure occurred between the two measurements with co-propagating and crossed Raman laser beams presented here. Furthermore, we are able to observe a shift of the resonance frequency of about 2 MHz while filling the superconducting magnet with helium, probably caused by a similar effect, as the temperature in the lab and the magnet is strongly affected by the filling process. However, this shift is non-permanent and a relaxation of the resonance frequency is observed within 24 hours.

6.2.2 Influence of the cooling laser parameters

We repeat the thermometry measurement for different parameters of the cooling laser to analyze their influence on the final temperature. Figure 6.7 shows the dependence of the axial temperature on the detuning of the cooling laser. We observe

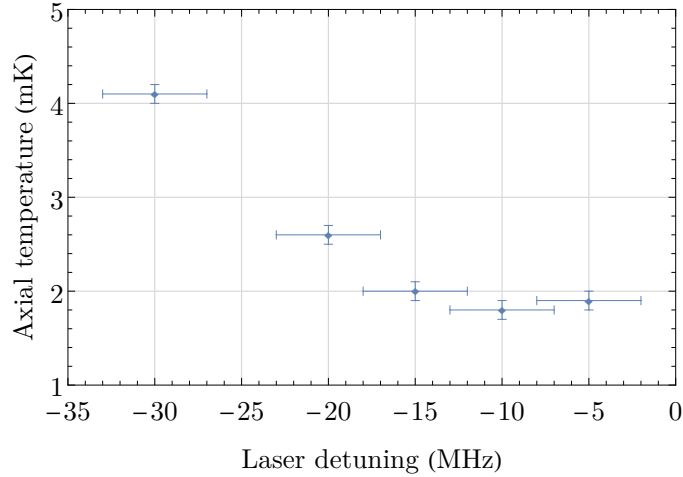


Figure 6.7: Measurement of the axial mode temperature as a function of the cooling laser detuning. The large uncertainty of the detuning for each measurement is related to the unknown Doppler shift due to the rotation frequency. See text for details.

a minimum temperature of $1.8(1)$ mK at a detuning of -10 MHz, which is about half the linewidth of the resonance and in accordance with the theory presented in section 2.3. For detunings further away from the resonance, a significant increase of the temperature is observed, while for detunings closer to the resonance, the temperature increase is less pronounced.

Measurements as a function of the laser power and the vertical laser beam position are shown in figure 6.8. No clear dependence of the temperature on these parameters can be observed. This is in accordance with equation 2.22, which does not predict a dependence of the axial kinetic energy on these parameters.

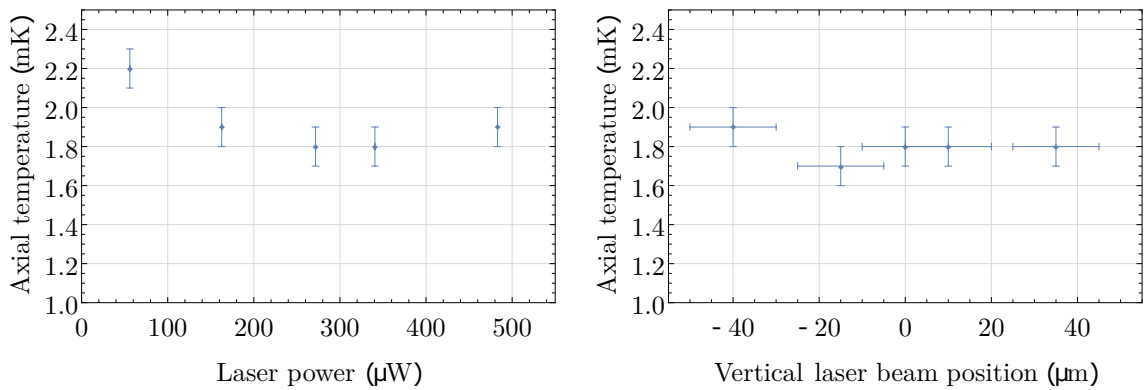


Figure 6.8: Measurement of the axial mode temperature as a function of the cooling laser power (left) and the vertical laser beam position (right). The error bars for the laser power are smaller than the data points. The vertical laser beam position must be understood as a relative measure, as it is not referenced to an absolute position. See text for details.

CHAPTER 7

Summary and Outlook

7.1 Summary

In this thesis, a cryogenic Penning trap system was presented that offers all prerequisites for ground state cooling of single ${}^9\text{Be}^+$ ions. In addition, cw laser systems at 313 nm for Doppler cooling, repumping and Raman interactions have been developed and integrated in the experiment. To this end, a new optical platform for laser beam delivery to the beryllium trap was used. Furthermore, a setup for locking the relative phase of two lasers at 313 nm as required for coherent Raman interactions was developed, characterized and set up.

The existing loading and particle ejection routines for the beryllium trap were extended by new cleaning procedures which reduce the influence of contaminants on all measurements. Carefully prepared ion clouds were used to measure the trap frequencies with high precision. These measurements gave indications that the magnetic field deviates from its expected value of 5 T.

The discrepant information about the magnetic field made it necessary to determine the resonance frequencies of the transitions used for cooling, probing and repumping of ${}^9\text{Be}^+$ through single- and multi-resonance measurements. After the determination of the repumping resonance frequencies, it was possible to prepare the ${}^9\text{Be}^+$ ions with high precision in the ${}^2S_{1/2} |m_J = +1/2\rangle$ state. Furthermore, the results allowed to estimate the qubit frequency, which subsequently could be probed with the Raman lasers.

A pair of phase-locked lasers at 313 nm was used for the demonstration of stimulated Raman-transitions with ${}^9\text{Be}^+$ ions. Co-propagating Raman laser beams were used to determine the qubit frequency with high precision, which in turn confirmed a magnetic field of about 4.989 T. Crossed Raman laser beams were used for thermometry measurements and the axial mode temperature was measured as a function of the cooling laser parameters. A minimal temperature of 1.77(10) mK could be achieved with a Doppler-cooled cloud of ${}^9\text{Be}^+$ ions.

These results pave the way for future high-precision measurements with ${}^9\text{Be}^+$ ions and protons. However, in order to enable sympathetic laser cooling of (anti-)protons

and g -factor measurements based on quantum logic spectroscopy, several improvements and system upgrades need to be implemented in the future.

7.2 Outlook

In the following, the major milestones on the way towards (anti-)proton g -factor measurements with quantum logic spectroscopy will be outlined. These milestones comprise improvements for the near future as well as long term upgrades of the Penning trap system.

7.2.1 Measurements with single ions

To simplify future measurements with single ions, it is necessary to enable their deterministic production. Although the current setup allows for the production of single ions, the loading process is non-deterministic and thus time consuming. As outlined in sections 4.1 and 4.2, we usually load a large number of ions, which is subsequently reduced until a single ion is left. However, for a low number of ions, it often happens that we lose all of them at once through the application of an ejection or cleaning routine. In this case, the whole process needs to be started over again. Currently, the production of a single ion takes several hours.

This can be remedied through the implementation of a photoionization laser for direct loading of a small number of ions [95]. In this case, the pulse energy of the ablation laser can be reduced, so that only neutral beryllium ions are ablated and the production rate of photoionized ions could be controlled with the additional laser. A suitable laser system has already been developed in the past [87, 88]. However, as it was not absolutely necessary for the operation of the experiment so far, it was dismissed to reduce the experimental overhead. In addition, the laser system suffered from the degradation of the BBO crystal used for the generation of light at 235 nm through SHG. This effect needs to be investigated and eliminated before the re-integration of the laser system into the experimental setup.

Another problem which needs to be solved in order to simplify measurements with single ions is the occurrence of fluorescence dropouts, as described in section 4.2. Since there is a reasonable chance that these dropouts are connected to the sensitive dependence of the gradient cooling technique on the cooling laser parameters, a disentanglement of the cooling process in the axial and radial directions will be helpful. For example, an additional axial cooling laser beam can be implemented, as is the case in other Penning trap experiments with laser cooled ions [89, 91]. The additional cooling beam will allow for an independent adjustment of the axial and radial cooling rates. In this way, a bigger parameter space is available for the search of a robust setting with a stable fluorescence signal. A potential design for the implementation of an axial cooling beam in our experimental setup was investigated in reference [96].

In general, the experiment will benefit from an improved beam pointing stability of all lasers. Although a series of improvements concerning the passive stability of the laser beams has been implemented recently, slow drifts of the beams are still present at the position of the ions. A connection between these drifts and the aforementioned fluorescence dropouts could not be ruled out so far. To this end, an active beam pointing stabilization setup based on a position sensor and piezo-actuated mirror or lens mounts can be implemented.

A complementary approach to the problem of fluorescence dropouts is the implementation of an axialization drive [65, 97], which allows to couple the magnetron motion to the modified cyclotron motion. The advantage of this method is that the magnetron mode can be cooled more efficiently and laser cooling becomes possible without the restrictions comprised in equation 2.21. To this end, it will be necessary to ensure the functionality of the RF lines of the ring electrode segments in the beryllium trap, as otherwise no pure rotating quadrupole field can be applied. Since this requires to open and disassemble the experimental apparatus, the electrodes of the beryllium trap should be replaced by new ones without nickel plating at the same time. In this way, it is possible to check whether the ferro-magnetic plating is the cause of the observed reduction of the magnetic field.

7.2.2 Sideband spectroscopy and ground state cooling of ${}^9\text{Be}^+$

With a possibility to reliably trap and detect single ${}^9\text{Be}^+$ ions without fluorescence dropouts, the techniques used for thermometry measurements presented in this thesis can be used for sideband spectroscopy of single ions as well. Figure 7.1 shows a sideband spectroscopy measurement of the axial motion that was taken with a single ion. Here, the data was post-processed to dismiss all data points where the ion had left the field of view of the imaging system. Although the post-processing routine increased the total time required for the data acquisition and evaluation to two days, it was the first measurement which proved that sideband spectroscopy is possible in our setup. However, a large number of sidebands was observed, corresponding to a large Lamb-Dicke factor and a high thermal occupation number. Sideband cooling with this system is very slow and requires the implementation of many sideband pulses on different higher order sidebands to reach the ground state.

To improve on this problem, we can increase the axial trap frequency, which reduces the Lamb-Dicke factor and the mean occupation number after Doppler cooling at the same time. However, an increase of the axial frequency is always connected to an increase of the magnetron frequency as well. Thus, the axial trap frequency can only be increased up to the limit resulting from equation 2.21, as long we rely on the gradient cooling technique only.

One way to overcome this limit is to use the axialization technique as described in the previous section. To this end, careful tuning of the applied DC and RF voltages is required, to avoid the introduction of micromotion at the axialization frequency

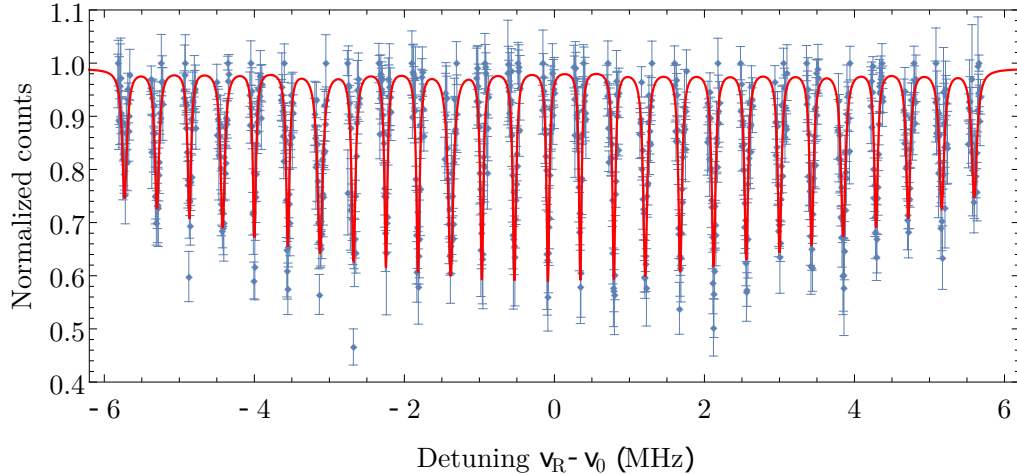


Figure 7.1: Sideband spectroscopy measurement of the axial motion of a single ion. The normalized PMT counts are shown as a function of the laser frequency difference between the Raman lasers. The blue data points and error bars correspond to a series of resonance measurements, where each sideband was probed in a “windowed” measurement. The solid red line is a comb of individually fitted Lorentz profiles with a global Gaussian envelope. The frequency differences are given relative to the frequency $\nu_0 = 138\,911.9$ MHz.

[89]. With a carefully tuned and aligned trap, temperatures close to the Doppler limit and thus a lower thermal occupation number should be achievable. From this starting point, ground state cooling of single ${}^9\text{Be}^+$ ions can be implemented with a multi-sideband cooling procedure as laid out in references [26, 98], where the number of required sideband pulses is reduced and the cooling speed is increased.

7.2.3 Sympathetic cooling of protons

For sympathetic laser cooling of protons, the demonstration of Coulomb coupling of single ions in a double-well potential is necessary. To this end, ${}^9\text{Be}^+$ ions and protons must be transported along the trap stack.

Fast adiabatic transport of ions in our Penning trap system has been investigated in reference [41]. Although the measurements were carried out with ion clouds, the techniques developed in this work enable for fast adiabatic transport of single ions as well. Using the macroscopic coupling trap currently installed in the Penning trap stack, we will be able to conduct first proof-of-principle measurements for Coulomb coupling of two ${}^9\text{Be}^+$ ions in a symmetric double-well potential in the future.

To extend this technique to protons, it will become necessary to commission the proton source. In the current setup, it was not possible to demonstrate proton production. We suspect a gold mesh which is mounted in front of the electron gun as the cause. Although the mesh is mounted in order to prevent excessive charging of the dielectric surfaces, it looks like the period of the grating was chosen too small, so that even a small misalignment of the electron gun during assembly or because

of contractions during the cooldown of the system might lead to an orientation in which the mesh blocks the beam of the electron gun. In this case, no protons can be produced from the polyethylene target. In the new design of the proton source, a mesh with a larger period is chosen to avoid this problem in the future.

As soon as protons can be produced, they need to be pre-cooled with a cryogenic tank circuit. To this end, particle detection based on induced image-charge detection with the already installed cryogenic resonators [66, 99] needs to be demonstrated and characterized.

For Coulomb coupling of single ${}^9\text{Be}^+$ ions and protons, a micro-fabricated coupling trap needs to be machined and produced [35]. This miniaturized version of the coupling trap will allow for an asymmetric double-well potential, which is required for efficient coupling of particles with different masses. In the current design, each electrode will have an inner radius of $400\ \mu\text{m}$ and a thickness of $200\ \mu\text{m}$. The smaller dimensions of the trap will allow to decrease the distance of the particles in the double-well potential to $300\ \mu\text{m}$ and to increase the trap frequency of both particles to about $4\ \text{MHz}$ [7]. Both of these effects will increase the exchange rate and thus reduce the time required for a complete exchange of the motional energy. Electrode samples for the new coupling trap have been produced and are currently being investigated.

In combination with ground state cooling of single beryllium ions, the micro-fabricated coupling trap will enable for ground state cooling of single protons, which is an essential prerequisite for quantum logic spectroscopy.

7.2.4 Quantum logic spectroscopy with protons

The last missing tool for the implementation of quantum logic spectroscopy is a sideband trap for protons. In this dedicated trap, sideband transitions can be driven through the combination of an RF drive with a static magnetic field gradient [38, 100]. Provided the proton is in the ground state, red and blue sidebands can be driven as in the case of laser driven sidebands.

Combining all the aforementioned techniques, fast readout of the proton's spin state will be possible using quantum logic spectroscopy. To this end, a single proton will be cooled to its ground state through sympathetic laser cooling with a single ${}^9\text{Be}^+$ ion in the engineered double-well potential. In the next step, the spin state information can be transferred from the proton to the ${}^9\text{Be}^+$ ion using the common motion as a quantum bus. Finally, fluorescence detection can be used to determine the spin state of the ${}^9\text{Be}^+$ ion and to retrieve the information about the spin state of the proton.

7.2.5 Measurement of the proton g -factor

The details of g -factor measurements based on quantum logic spectroscopy are laid out in reference [34]. In comparison with current routines for particle preparation and spin state readout based on cryogenic tank-circuits and the continuous Stern-Gerlach

effect, faster experiment cycle times will become possible and potential sidereal variations of the g -factor may be studied.

APPENDIX A

Calculation of the transition frequencies

In the following, the equations for calculating the transition frequencies of ${}^9\text{Be}^+$ are summarized briefly. They are taken from reference [91], in which the corresponding theory is laid out in detail. The calculations are based on the fact that the field-free transitions between the S and P manifolds are well known and only additional contributions due to the spin-orbit coupling, the Zeeman interaction with the electron's spin and orbital magnetic moment, the Zeeman interaction with the nuclear magnetic moment and the hyperfine interaction need to be taken care of.

Throughout this appendix, h is Planck's constant, μ_B is the Bohr magneton and the different g 's denote corresponding g -factors of angular momentum. Measured atomic constants for ${}^9\text{Be}^+$ are listed in table A.1.

Table A.1: Atomic constants of ${}^9\text{Be}^+$

Name	Value	Reference
Field-free transition $\nu_{S_{1/2} \rightarrow P_{3/2}}$	957.396 80(13) THz	[61], converted to THz
Field-free transition $\nu_{S_{1/2} \rightarrow P_{1/2}}$	957.199 65(12) THz	[61], converted to THz
Fine structure splitting $\Delta E/h$	197.150(64) GHz	[61]
Hyperfine constant $A_{P_{3/2}}$	-1.5(12) MHz	[61]
Hyperfine constant $A_{P_{1/2}}$	-118.6(36) MHz	[61]
Hyperfine constant $A_{S_{1/2}}$	-625.008 837 048(10) MHz	[63]
Nuclear g -factor ^a g_I	$2.134\,779\,853(2) \times 10^{-4} g_J$	[63]

^a We use the definition of reference [63], which relates the nuclear magnetic moment to the Bohr magneton μ_B . This simplifies the Breit-Rabi formulae given below. In some literature, such as reference [61], the magnetic moment is related to the nuclear magneton μ_N and a corresponding value for g_I is quoted instead.

Energy shifts of the ${}^2P_{1/2}$ and ${}^2P_{3/2}$ states

The energy scale in the P manifold is dominated by the spin-orbit interaction and the electronic Zeeman interaction. The hyperfine interaction and contributions from the nuclear magnetic moment can be neglected in the initial calculations, because their energy scale is several orders of magnitude lower. The following equations are obtained using exact diagonalization of the corresponding Hamiltonian in the $|L, S, m_L, m_S\rangle$ basis.

The energy shifts of the ${}^2P_{3/2}$ states are given by the equations

$$\begin{aligned}
E_{3/2}^{3/2} &= \frac{1}{3}\Delta E + \mu_B(1 + \frac{1}{2}g_S)B \\
E_{1/2}^{3/2} &= \frac{1}{6}\left(-\Delta E + 3\mu_B B + \sqrt{9\Delta E^2 + 6\Delta E\mu_B(g_S - 1)B + 9\mu_B^2(g_S - 1)^2B^2}\right) \\
E_{-1/2}^{3/2} &= \frac{1}{6}\left(-\Delta E - 3\mu_B B + \sqrt{9\Delta E^2 - 6\Delta E\mu_B(g_S - 1)B + 9\mu_B^2(g_S - 1)^2B^2}\right) \\
E_{-3/2}^{3/2} &= \frac{1}{3}\Delta E - \mu_B(1 + \frac{1}{2}g_S)B
\end{aligned} \tag{A.1}$$

and the energy shifts of the ${}^2P_{1/2}$ states are given by

$$\begin{aligned}
E_{1/2}^{1/2} &= \frac{1}{6}\left(-\Delta E + 3\mu_B B - \sqrt{9\Delta E^2 + 6\Delta E\mu_B(g_S - 1)B + 9\mu_B^2(g_S - 1)^2B^2}\right) \\
E_{-1/2}^{1/2} &= \frac{1}{6}\left(-\Delta E - 3\mu_B B - \sqrt{9\Delta E^2 - 6\Delta E\mu_B(g_S - 1)B + 9\mu_B^2(g_S - 1)^2B^2}\right).
\end{aligned} \tag{A.2}$$

In both cases, we can account for the hyperfine interaction and the contribution of the nuclear magnetic moment by treating them perturbatively and adding the additional terms

$$E_{\text{hf,nuc}} = hAm_I m_J + \mu_B g_I m_I B, \tag{A.3}$$

where A corresponds to the hyperfine constant of the respective P state.

Energy shifts of the ${}^2S_{1/2}$ states

In case of the S manifold a different approach needs to be pursued. Due to the vanishing orbital angular momentum, the spin-orbit interaction does not dominate the energy scale and the hyperfine interaction as well as the contribution due to the nuclear magnetic moment need to be considered before diagonalization. Thus, diagonalization is carried out in the $|F, m_F\rangle$ basis, which leads to equations that are

known as the Breit-Rabi formulae. The resulting energy shifts are given by

$$E_{m_F=F_{\pm}} = hAIJ \pm \frac{1}{2}\mu_B B(g_J J + g_I I) \quad (\text{A.4})$$

in the case of the stretched states with $F_{\pm} \equiv \pm(I + J)$, where A is the hyperfine constant of the $^2S_{1/2}$ states. The energy shifts for the remaining states are given by

$$E_{F,m_F} = -\frac{hA}{4} + g_I m_F \mu_B B \pm \frac{1}{2} \sqrt{h^2 A^2 F_{\pm}^2 + 2hA m_F \mu_B (g_J - g_I) B + \mu_B^2 (g_I - g_J)^2 B^2}, \quad (\text{A.5})$$

where a plus (minus) sign in front of the root corresponds to the case of $F = 1$ ($F = 2$) and $m_F = 0, \pm 1$.

Transition frequencies

The resonance frequency for a given transition can be calculated by adding the shifts of the involved states from the field free transition. In case of the cooling laser, these are the $^2S_{1/2} |m_I = +3/2, m_J = +1/2\rangle$ and the $^2P_{3/2} |m_I = +3/2, m_J = +3/2\rangle$ states, yielding

$$\begin{aligned} h\nu_{cooling} &= h\nu_{S_{1/2} \rightarrow P_{3/2}} + E_{3/2}^{3/2} - \frac{1}{3} \Delta E \\ &+ hA_{3/2} m_I m_J + \mu_B g_I m_I B - E_{m_F=F_+}. \end{aligned} \quad (\text{A.6})$$

In case of the repumping laser, these are the $^2S_{1/2} |m_I = +3/2, m_J = -1/2\rangle$ and the $^2P_{3/2} |m_I = +3/2, m_J = +1/2\rangle$ states, corresponding to

$$\begin{aligned} h\nu_{repumping} &= h\nu_{S_{1/2} \rightarrow P_{3/2}} + E_{1/2}^{3/2} - \frac{1}{3} \Delta E \\ &+ hA_{3/2} m_I m_J + \mu_B g_I m_I B - E_{F=2, m_F=1}. \end{aligned} \quad (\text{A.7})$$

Furthermore, the transition frequency for the qubit is given by the Breit-Rabi formulae:

$$h\nu_{Qubit} = E_{m_F=F_+} - E_{F=2, m_F=1}. \quad (\text{A.8})$$

APPENDIX B

Rendered image of the experimental setup

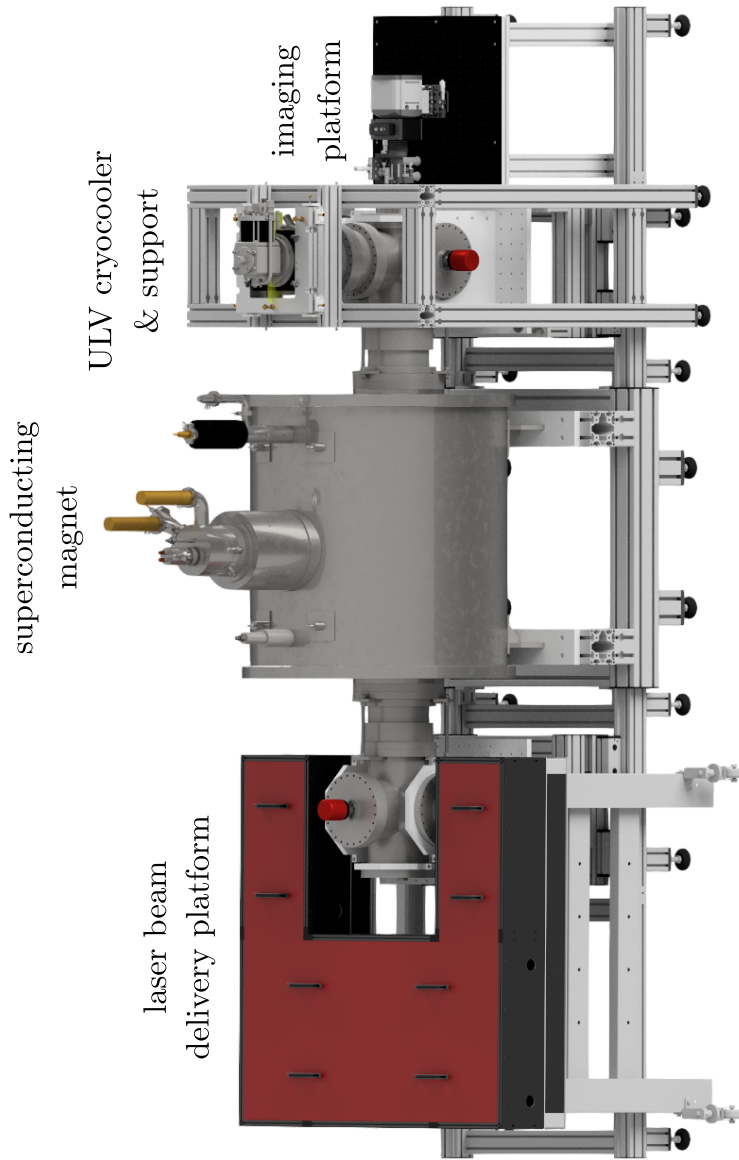


Figure B.1: Rendered image of the experimental setup. The system is 4 m long, 1 m wide and 2 m tall.

APPENDIX C

Recipe for UV fiber production

To guide the laser beams at 313 nm from their enclosures to the optical delivery platform, we use custom UV-compatible fibers. The fibers are produced with the following recipe, which was adapted from the procedures described in references [101, 102]. Although an infrastructure for fiber connectorization and hydrogen loading exists at PTB, we decided to rely on external companies for the production process. In the case of connectorization of PM fibers, this is because the company achieved better results than the average PhD student in terms of mode shape and incoupling efficiencies. In the case of hydrogen loading, this is because the hydrogen vessel at PTB is not able to accommodate fibers with the required length of 6 m.

In the following, the steps for the production of ready-to-use fibers are summarized:

- **Step 1 - Fiber connectorization:** We use large mode area (LMA) fibers of the type *LMA-10-PM* from *NKT Photonics*, which we order with a length of 6 m at *ALPhANOV*. Before shipment, the fibers are equipped with two FC/APC connectors that can handle injection losses up to 500 mW and a 3 mm steel jacketing. We choose steel instead of polyvinyl chloride (PVC), as this reduces the problems associated with plastic memory, which typically occur after hydrogen loading.
- **Step 2 - Hydrogen loading:** We send the fibers to *iXBlue Photonics*, where they are hydrogenated in a pressurized vessel for two weeks. Typical process parameters¹ are a pressure of 150 bar and a temperature of 50 °C. After hydrogenation, the fibers are stored at −18 °C and shipped in an insulated cooling box, because a low temperature reduces the rate at which hydrogen diffuses out of the fiber. Once the fibers arrive at Hannover, we store them in a freezer. In this state, the fibers can be stored for weeks, if required.
- **Step 3 - UV curing:** We take the fibers out of the freezer and let them accommodate to room temperature. The fibers are mounted with pairs of

¹ It is likely that other combinations of time periods and process parameters will give equally good results. Due to the limited number of fibers produced, we have not yet had the opportunity to try them out.

suitable fiber couplers, so that the fiber tips can be flushed with nitrogen to avoid degradation. We couple a 313 nm laser beam into the fibers, so that a laser power between 10 mW and 20 mW is transmitted and expose the fibers to the laser light for 48 hours. In this process, color centers are formed through the interaction with the UV radiation and subsequently inactivated through a chemical reaction with the nearby hydrogen molecules. The result are UV solarization resistant fibers, which are ready for use in the experiment.

If the fibers are handled carefully and constantly flushed with nitrogen, operation is possible for about a year without problems. Over time, a slow degradation of the mode profile is observable, which leads to a smearing of the usual hexagonal shape. In this case, one can try to polish the fiber tip to remove potential contaminants on the surface or send the fibers to *ALPhANOV*, so that they can be re-connectorized. It is not necessary to repeat hydrogen loading and UV curing for fibers which have been cured before.

Bibliography

- [1] A. R. Liddle: *An Introduction to Modern Cosmology*. Wiley (2015). (see p. 1)
- [2] W. Quint and M. Vogel: *Fundamental Physics in Particle Traps*. Springer (2014). (see p. 1)
- [3] R. Lehnert: *CPT Symmetry and Its Violation*. *Symmetry* **8**, 114 (2016). doi: 10.3390/sym8110114 (see p. 1)
- [4] W. Demtröder: *Experimentalphysik 4: Kern-, Teilchen- und Astrophysik*. Springer Spektrum (2017). doi: 10.1007/978-3-662-52884-6 (see p. 1)
- [5] R. S. Van Dyck, P. B. Schwinberg and H. G. Dehmelt: *New high-precision comparison of electron and positron g factors*. *Physical Review Letters* **59**, 26–29 (1987). doi: 10.1103/PhysRevLett.59.26 (see p. 1)
- [6] B. Schwingenheuer et al.: *CPT Tests in the Neutral Kaon System*. *Physical Review Letters* **74**, 4376–4379 (1995). doi: 10.1103/PhysRevLett.74.4376 (see p. 1)
- [7] C. Smorra et al.: *BASE – The Baryon Antibaryon Symmetry Experiment*. *The European Physical Journal Special Topics* **224**, 3055 (2015). doi: 10.1140/epjst/e2015-02607-4 (see pp. 1, 77)
- [8] S. Ulmer, C. Smorra, A. Mooser, K. Franke, H. Nagahama, G. Schneider, T. Higuchi, S. Van Gorp, K. Blaum, Y. Matsuda, W. Quint, J. Walz and Y. Yamazaki: *High-precision comparison of the antiproton-to-proton charge-to-mass ratio*. *Nature* **524**, 196–199 (2015). doi: 10.1038/nature14861 (see p. 1)
- [9] G. Schneider, A. Mooser, M. Bohman, N. Schön, J. Harrington, T. Higuchi, H. Nagahama, S. Sellner, C. Smorra, K. Blaum, Y. Matsuda, W. Quint, J. Walz and S. Ulmer: *Double-trap measurement of the proton magnetic moment at 0.3 parts per billion precision*. *Science* **358**, 1081–1084 (2017). doi: 10.1126/science.aan0207 (see pp. 1, 2)
- [10] C. Smorra et al.: *A parts-per-billion measurement of the antiproton magnetic moment*. *Nature* **550**, 371–374 (2017). doi: 10.1038/nature24048 (see pp. 1, 2)

- [11] S. Sellner et al.: *Improved limit on the directly measured antiproton lifetime*. New Journal of Physics **19**, 083023 (2017). doi: 10.1088/1367-2630/aa7e73 (see pp. 2, 22, 41)
- [12] H. Häffner, T. Beier, S. Djekić, N. Hermanspahn, H.-J. Kluge, W. Quint, S. Stahl, J. Verdú, T. Valenzuela and G. Werth: *Double Penning trap technique for precise g factor determinations in highly charged ions*. The European Physical Journal D - Atomic, Molecular, Optical and Plasma Physics **22**, 163–182 (2003). doi: 10.1140/epjd/e2003-00012-2 (see p. 2)
- [13] L. S. Brown and G. Gabrielse: *Geonium theory: Physics of a single electron or ion in a Penning trap*. Reviews of Modern Physics **58**, 233–311 (1986). doi: 10.1103/RevModPhys.58.233 (see pp. 2, 7)
- [14] H. G. Dehmelt: *Continuous Stern-Gerlach effect: Principle and idealized apparatus*. Proceedings of the National Academy of Sciences of the United States of America **83**, 2291–2294 (1986). (see p. 2)
- [15] S. Ulmer, A. Mooser, H. Nagahama, S. Sellner and C. Smorra: *Challenging the standard model by high-precision comparisons of the fundamental properties of protons and antiprotons*. Philosophical Transactions of the Royal Society A: Mathematical, Physical and Engineering Sciences **376**, 20170275 (2018). doi: 10.1098/rsta.2017.0275 (see p. 2)
- [16] S. Ulmer: *First Observation of Spin Flips with a Single Proton Stored in a Cryogenic Penning Trap*. PhD thesis, Universität Heidelberg (2011). (see pp. 2, 8, 10)
- [17] G. Schneider: *300 ppt Measurement of the Proton g -Factor*. PhD thesis, Johannes Gutenberg-Universität (2017). (see p. 2)
- [18] D. J. Wineland and W. M. Itano: *Laser cooling of atoms*. Physical Review A **20**, 1521–1540 (1979). doi: 10.1103/PhysRevA.20.1521 (see pp. 3, 11, 14, 16)
- [19] F. Diedrich, J. C. Bergquist, W. M. Itano and D. J. Wineland: *Laser Cooling to the Zero-Point Energy of Motion*. Physical Review Letters **62**, 403 (1989). doi: 10.1103/PhysRevLett.62.403 (see p. 3)
- [20] D. J. Heinzen and D. J. Wineland: *Quantum-limited cooling and detection of radio-frequency oscillations by laser-cooled ions*. Physical Review A **42**, 2977 (1990). doi: 10.1103/PhysRevA.42.2977 (see p. 3)
- [21] P. O. Schmidt, T. Rosenband, C. Langer, W. M. Itano, J. C. Bergquist and D. J. Wineland: *Spectroscopy Using Quantum Logic*. Science **309**, 749–752 (2005). doi: 10.1126/science.1114375 (see p. 3)
- [22] C. W. Chou, D. B. Hume, J. C. J. Koelemeij, D. J. Wineland and T. Rosenband: *Frequency Comparison of Two High-Accuracy Al^+ Optical Clocks*. Physical Review Letters **104**, 070802 (2010). doi: 10.1103/PhysRevLett.104.070802 (see p. 3)

- [23] F. Wolf, Y. Wan, J. C. Heip, F. Gebert, C. Shi and P. O. Schmidt: *Non-destructive state detection for quantum logic spectroscopy of molecular ions*. Nature **530**, 457–460 (2016). doi: 10.1038/nature16513 (see p. 3)
- [24] C.-W. Chou, C. Kurz, D. B. Hume, P. N. Plessow, D. R. Leibbrandt and D. Leibfried: *Preparation and coherent manipulation of pure quantum states of a single molecular ion*. Nature **545**, 203–207 (2017). doi: 10.1038/nature22338 (see p. 3)
- [25] P. Micke, T. Leopold, S. A. King, E. Benkler, L. J. Spieß, L. Schmöger, M. Schwarz, J. R. Crespo López-Urrutia and P. O. Schmidt: *Coherent laser spectroscopy of highly charged ions using quantum logic*. Nature **578**, 60–65 (2020). doi: 10.1038/s41586-020-1959-8 (see p. 3)
- [26] J. F. Goodwin, G. Stutter, R. C. Thompson and D. M. Segal: *Resolved-Sideband Laser Cooling in a Penning Trap*. Physical Review Letters **116**, 143002 (2016). doi: 10.1103/PhysRevLett.116.143002 (see pp. 3, 76)
- [27] P. Hrmo, M. K. Joshi, V. Jarlaud, O. Corfield and R. C. Thompson: *Sideband cooling of the radial modes of motion of a single ion in a Penning trap*. Physical Review A **100**, 043414 (2019). doi: 10.1103/PhysRevA.100.043414 (see p. 3)
- [28] M. Bohman, A. Mooser, G. Schneider, N. Schön, M. Wiesinger, J. Harrington, T. Higuchi, H. Nagahama, C. Smorra, S. Sellner, K. Blaum, Y. Matsuda, W. Quint, J. Walz and S. Ulmer: *Sympathetic cooling of protons and antiprotons with a common endcap Penning trap*. Journal of Modern Optics **65**, 568–576 (2018). doi: 10.1080/09500340.2017.1404656 (see p. 3)
- [29] J. M. Cornejo, M. J. Gutiérrez, E. Ruiz, A. Bautista-Salvador, C. Ospelkaus, S. Stahl and D. Rodríguez: *An optimized geometry for a micro Penning-trap mass spectrometer based on interconnected ions*. International Journal of Mass Spectrometry **410**, 22–30 (2016). doi: 10.1016/j.ijms.2016.10.010 (see p. 3)
- [30] M. Bohman: *Sympathetic Cooling of a Proton with Resonant Image Current Coupling*. PhD thesis, Universität Heidelberg (2020). (see pp. 3, 46)
- [31] D. J. Wineland, C. Monroe, W. M. Itano, D. Leibfried, B. E. King and D. M. Meekhof: *Experimental issues in coherent quantum-state manipulation of trapped atomic ions*. Journal of Research of the National Institute of Standards and Technology **103**, 259 (1998). doi: 10.6028/jres.103.019 (see pp. 3, 14, 15, 17)
- [32] K. R. Brown, C. Ospelkaus, Y. Colombe, A. C. Wilson, D. Leibfried and D. J. Wineland: *Coupled quantized mechanical oscillators*. Nature **471**, 196–199 (2011). doi: 10.1038/nature09721 (see p. 3)
- [33] M. Harlander, R. Lechner, M. Brownnutt, R. Blatt and W. Hansel: *Trapped-ion antennae for the transmission of quantum information*. Nature **471**, 200–203 (2011). doi: 10.1038/nature09800 (see p. 3)

- [34] J. M. Cornejo, R. Lehnert, M. Niemann, J. Mielke, T. Meiners, A. Bautista-Salvador, M. Schulte, D. Nitzschke, M. J. Borchert, K. Hammerer, S. Ulmer and C. Ospelkaus: *Quantum logic inspired techniques for spacetime-symmetry tests with (anti-)protons*. *New Journal of Physics* **23**, 073045 (2021). doi: 10.1088/1367-2630/ac136e (see pp. 3, 17, 77)
- [35] J.-A. Fenske: *Prozessierung von Komponenten mikro-strukturierter Penning-Ionenfallen*. Master's thesis, Technische Universität Braunschweig (2019). (see pp. 3, 22, 77)
- [36] A.-G. Paschke: *$^9\text{Be}^+$ ion qubit control using an optical frequency comb*. PhD thesis, Leibniz Universität Hannover (2017). (see p. 3)
- [37] J. Mielke, J. Pick, J.-A. Coenders, T. Meiners, M. Niemann, J. M. Cornejo, S. Ulmer and C. Ospelkaus: *139 GHz UV phase-locked Raman laser system for thermometry and sideband cooling of $^9\text{Be}^+$ ions in a Penning trap*. arXiv:2106.13532v1 (2021). (see p. 3)
- [38] D. Nitzschke, M. Schulte, M. Niemann, J. M. Cornejo, S. Ulmer, R. Lehnert, C. Ospelkaus and K. Hammerer: *Elementary Laser-Less Quantum Logic Operations with (Anti-)Protons in Penning Traps*. *Advanced Quantum Technologies* **9**, 1900133 (2020). doi: 10.1002/qute.201900133 (see pp. 3, 77)
- [39] M. Niemann: *Design and commissioning of an experiment for sympathetic cooling and coupling of ions in a cryogenic Penning trap*. PhD thesis, Leibniz Universität Hannover (2019). (see pp. 4, 20, 22–24, 42, 45, 50, 53)
- [40] M. Niemann, T. Meiners, J. Mielke, M. J. Borchert, J. M. Cornejo, S. Ulmer and C. Ospelkaus: *Cryogenic $^9\text{Be}^+$ Penning trap for precision measurements with (anti-)protons*. *Measurement Science and Technology* **31**, 035003 (2019). doi: 10.1088/1361-6501/ab5722 (see pp. 4, 23)
- [41] T. Meiners: *Characterisation of an experiment for sympathetic cooling and coupling of ions in a cryogenic Penning trap*. PhD thesis, Leibniz Universität Hannover (2021). (see pp. 4, 8, 21, 38, 44, 45, 49, 50, 55, 70, 76)
- [42] J. D. Jackson: *Classical Electrodynamics*. Wiley (1999). (see pp. 5, 8)
- [43] M. Vogel: *Particle Confinement in Penning Traps*. Springer International Publishing (2018). doi: 10.1007/978-3-319-76264-7_1 (see pp. 5, 49)
- [44] M. Knoop, N. Madsen and R. C. Thompson: *Trapped Charged Particles: A Graduate Textbook with Problems and Solutions*. World Scientific (Europe) (2016). doi: 10.1142/q0004 (see p. 7)
- [45] G. Gabrielse, L. Haarsma and S. L. Rolston: *Open-endcap Penning traps for high precision experiments*. *International Journal of Mass Spectrometry and Ion Processes* **88**, 319–332 (1989). doi: 10.1016/0168-1176(89)85027-X (see pp. 8, 10)

- [46] R. S. Van Dyck, D. J. Wineland, P. Ekstrom and H. G. Dehmelt: *High mass resolution with a new variable anharmonicity Penning trap*. Applied Physics Letters, 446 (1976). (see p. 8)
- [47] R. C. Thompson and D. C. Wilson: *The motion of small numbers of ions in a Penning trap*. Zeitschrift für Physik D: Atoms, Molecules and Clusters **42**, 271–277 (1997). doi: 10.1007/s004600050367 (see p. 10)
- [48] D. H. E. Dubin and T. M. O’Neil: *Trapped nonneutral plasmas, liquids, and crystals (the thermal equilibrium states)*. Reviews of Modern Physics **71**, 87–172 (1999). doi: 10.1103/RevModPhys.71.87 (see p. 10)
- [49] R. C. Thompson: *Ion Coulomb crystals*. Contemporary Physics **56**, 63–79 (2015). doi: <http://dx.doi.org/10.1080/00107514.2014.989715> (see p. 10)
- [50] E. L. Pollock and J. P. Hansen: *Statistical Mechanics of Dense Ionized Matter. II. Equilibrium Properties and Melting Transition of the Crystallized One-Component Plasma*. Physical Review A **8**, 3110–3122 (1973). doi: 10.1103/PhysRevA.8.3110 (see p. 10)
- [51] S. L. Gilbert, J. J. Bollinger and D. J. Wineland: *Shell-Structure Phase of Magnetically Confined Strongly Coupled Plasmas*. Physical Review Letters **60**, 2022–2025 (1988). doi: 10.1103/PhysRevLett.60.2022 (see p. 10)
- [52] J. J. Bollinger, D. J. Heinzen, F. L. Moore, W. M. Itano, D. J. Wineland and D. H. E. Dubin: *Electrostatic modes of ion-trap plasmas*. Physical Review A **48**, 525–545 (1993). doi: 10.1103/PhysRevA.48.525 (see p. 11)
- [53] L. R. Brewer, J. D. Prestage, J. J. Bollinger, W. M. Itano, D. J. Larson and D. J. Wineland: *Static properties of a non-neutral ${}^9\text{Be}^+$ -ion plasma*. Physical Review A **38**, 859–873 (1988). doi: 10.1103/PhysRevA.38.859 (see pp. 11, 53, 56, 58)
- [54] X.-P. Huang, J. J. Bollinger, T. B. Mitchell and W. M. Itano: *Phase-Locked Rotation of Crystallized Non-neutral Plasmas by Rotating Electric Fields*. Physical Review Letters **80**, 73–76 (1998). doi: 10.1103/PhysRevLett.80.73 (see p. 11)
- [55] X.-P. Huang, J. J. Bollinger, T. B. Mitchell, W. M. Itano and D. H. E. Dubin: *Precise control of the global rotation of strongly coupled ion plasmas in a Penning trap*. Physics of Plasmas **5**, 1656–1663 (1998). doi: 10.1063/1.872834 (see p. 11)
- [56] C. J. Foot: *Atomic Physics*. Oxford University Press (2005). (see pp. 11, 14)
- [57] W. M. Itano and D. J. Wineland: *Laser cooling of ions stored in harmonic and Penning traps*. Physical Review A **25**, 35–54 (1982). doi: 10.1103/PhysRevA.25.35 (see pp. 12, 13)
- [58] S. Mavadia: *Motional Sideband Spectra and Coulomb Crystals in a Penning Trap*. PhD thesis, Imperial College London (2013). (see p. 13)

- [59] C. C. Gerry and P. L. Knight: *Introductory Quantum Optics*. Cambridge University Press (2005). (see p. 15)
- [60] M. Niemann: *Konzeption eines Quantenlogikdetektors für Tests diskreter Symmetrien mit (Anti-)Protonen*. Master's thesis, Leibniz Universität Hannover (2013). (see p. 18)
- [61] J. J. Bollinger, J. S. Wells, D. J. Wineland and W. M. Itano: *Hyperfine structure of the $2p\ ^2P_{1/2}$ state in $^9\text{Be}^+$* . *Physical Review A* **31**, 2711–2714 (1985). doi: 10.1103/PhysRevA.31.2711 (see pp. 18, 79)
- [62] D. J. Wineland, J. C. Bergquist, W. M. Itano and R. E. Drullinger: *Double-resonance and optical-pumping experiments on electromagnetically confined, laser-cooled ions*. *Optics Letters* **5**, 245–247 (1980). doi: 10.1364/OL.5.000245 (see p. 18)
- [63] D. J. Wineland, J. J. Bollinger and W. M. Itano: *Laser-Fluorescence Mass Spectroscopy*. *Physical Review Letters* **50**, 628 (1983). doi: 10.1103/PhysRevLett.50.628 (see p. 79)
- [64] G. Schneider: *Development of a Penning trap system for the high precision measurement of the antiproton's magnetic moment*. Master's thesis, Johannes Gutenberg-Universität Mainz (2014). (see pp. 21, 22)
- [65] H. F. Powell, D. M. Segal and R. C. Thompson: *Axialization of Laser Cooled Magnesium Ions in a Penning Trap*. *Physical Review Letters* **89**, 093003 (2002). doi: 10.1103/PhysRevLett.89.093003 (see pp. 21, 75)
- [66] M. J. Borchert: *Developments for the high precision measurement of the antiproton magnetic moment*. Master's thesis, Leibniz Universität Hannover (2017). (see pp. 22, 77)
- [67] J. Pick: *Entwurf einer Quelle zum Laden von Protonen in eine kryogene Penningfalle*. Bachelor's thesis, Leibniz Universität Hannover (2017). (see p. 22)
- [68] N. Pulido: *A proton source for precision experiments in Penning traps*. Master's thesis, Leibniz Universität Hannover (2019). (see pp. 22, 43)
- [69] M. J. Borchert: *Challenging the Standard Model by high precision comparisons of the fundamental properties of antiprotons and protons*. PhD thesis, Leibniz Universität Hannover (2021). (see p. 22)
- [70] A. Franzen: *ComponentLibrary*. URL: <https://www.gwoptics.org/ComponentLibrary/> (visited on 08/04/2021) (see pp. 24, 66, 69)
- [71] A. C. Wilson, C. Ospelkaus, A. P. VanDevender, J. A. Mlynek, K. R. Brown, D. Leibfried and D. J. Wineland: *A 750-mW, continuous-wave, solid-state laser source at 313 nm for cooling and manipulating trapped $^9\text{Be}^+$ ions*. *Applied Physics B* **105**, 741–748 (2011). doi: 10.1007/s00340-011-4771-1 (see p. 25)

- [72] H.-Y. Lo, J. Alonso, D. Kienzler, B. C. Keitch, L. E. de Clercq, V. Negnevitsky and J. P. Home: *All-solid-state continuous-wave laser systems for ionization, cooling and quantum state manipulation of beryllium ions*. Applied Physics B **114**, 17–25 (2014). doi: 10.1007/s00340-013-5605-0 (see p. 25)
- [73] A. Idel: *Ein kompaktes Lasersystem zum sympathetischen Kühlen einzelner (Anti-) Protonen durch ${}^9\text{Be}^+$ Ionen*. Master's thesis, Leibniz Universität Hannover (2016). (see p. 26)
- [74] J. Pick: *140 GHz Raman laser system for quantum control in Penning traps*. Master's thesis, Leibniz Universität Hannover (2020). (see p. 26)
- [75] K. K. Voges: *Lasersysteme für Einzel-Ionen- Experimente mit ${}^9\text{Be}^+$* . Master's thesis, Leibniz Universität Hannover (2014). (see p. 26)
- [76] S. Hannig, J. Mielke, J.-A. Fenske, M. Misera, N. Beev, C. Ospelkaus and P. O. Schmidt: *A highly stable monolithic enhancement cavity for second harmonic generation in the ultraviolet*. Review of Scientific Instruments **89**, 013106 (2018). doi: 10.1063/1.5005515 (see p. 27)
- [77] T. W. Hänsch and B. Couillaud: *Laser frequency stabilization by polarization spectroscopy of a reflecting reference cavity*. Optics Communications **35**, 441–444 (1980). doi: 10.1016/0030-4018(80)90069-3 (see p. 28)
- [78] J.-A. Fenske: *Implementierung eines digitalen PID-Reglers mit dem Entwicklungsboard „Red Pitaya“*. Bachelor's thesis, Ostfalia Hochschule für angewandte Wissenschaften (2015). (see p. 28)
- [79] A. Tourigny-Plante, V. Michaud-Belleau, N. Bourbeau Hébert, H. Bergeron, J. Genest and J.-D. Deschênes: *An open and flexible digital phase-locked loop for optical metrology*. Review of Scientific Instruments **89**, 093103 (2018). doi: 10.1063/1.5039344 (see p. 33)
- [80] W. Peng, L. Zhou, S. Long, J. Wang and M. Zhan: *Locking laser frequency of up to 40 GHz offset to a reference with a 10 GHz electro-optic modulator*. Optics Letters **39**, 2998–3001 (2014). doi: 10.1364/OL.39.002998 (see p. 33)
- [81] Anritsu: *RF/Microwave Signal Generators MG3690B Technical Data Sheet* (2011). (see p. 34)
- [82] P. A. Williams, W. C. Swann and N. R. Newbury: *High-stability transfer of an optical frequency over long fiber-optic links*. JOSA B **25**, 1284–1293 (2008). doi: 10.1364/JOSAB.25.001284 (see p. 36)
- [83] m-Labs. URL: <https://m-labs.hk/> (visited on 07/27/2021) (see p. 38)
- [84] R. Bowler, U. Warring, J. W. Britton, B. C. Sawyer and J. Amini: *Arbitrary waveform generator for quantum information processing with trapped ions*. Review of Scientific Instruments **84**, 033108–033108–6 (2013). doi: doi:10.1063/1.4795552 (see p. 39)

- [85] H. G. Dehmelt: *A Single Atomic Particle Forever Floating at Rest in Free Space: New Value for Electron Radius*. *Physica Scripta* **T22**, 102–110 (1988). doi: 10.1088/0031-8949/1988/T22/016 (see p. 41)
- [86] B. C. Sawyer, J. G. Bohnet, J. W. Britton and J. J. Bollinger: *Reversing hydride-ion formation in quantum-information experiments with Be^+* . *Physical Review A* **91**, 011401 (2015). doi: 10.1103/PhysRevA.91.011401 (see pp. 41, 46)
- [87] J. Mielke: *A Frequency Quadrupled Lasersystem for Photoionization of 9Be* . Master's thesis, Leibniz Universität Hannover (2016). (see pp. 42, 74)
- [88] T. Florin: *Monolithischer Verdopplungsresonator zur Photoionisation einzelner 9Be -Atome*. Bachelor's thesis, Leibniz Universität Hannover (2017). (see pp. 42, 74)
- [89] J. F. Goodwin: *Sideband Cooling to the Quantum Ground State in a Penning Trap*. PhD thesis, Imperial College London (2015). (see pp. 43, 74, 76)
- [90] C. Smorra, A. Mooser, K. Franke, H. Nagahama, G. Schneider, T. Higuchi, S. V. Gorp, K. Blaum, Y. Matsuda, W. Quint, J. Walz, Y. Yamazaki and S. Ulmer: *A reservoir trap for antiprotons*. *International Journal of Mass Spectrometry* **389**, 10–13 (2015). doi: 10.1016/j.ijms.2015.08.007 (see p. 44)
- [91] C. D. Marciniak: *Design and operation of a Penning ion trap for quantum simulation*. PhD thesis, The University of Sydney (2020). (see pp. 46, 74, 79)
- [92] M. Kuckein: *Phase-locked magnetron excitation and implementation of a SWIFT-cleaning mechanism at ISOLTRAP*. Diploma thesis, Technische Universität München (2002). (see p. 47)
- [93] G. Gabrielse: *The true cyclotron frequency for particles and ions in a Penning trap*. *International Journal of Mass Spectrometry* **279**, 107–112 (2009). doi: 10.1016/j.ijms.2008.10.015 (see p. 51)
- [94] S. Kraemer: *Towards Laser Cooling of Beryllium Ions at the ALPHATRAP Experiment*. Master's thesis, Universität Heidelberg (2017). (see p. 56)
- [95] S. Mavadia, J. F. Goodwin, G. Stutter, S. Bharadia, D. R. Crick, D. M. Segal and R. C. Thompson: *Control of the conformations of ion Coulomb crystals in a Penning trap*. *Nature Communications* **4**, (2013). doi: 10.1038/ncomms3571 (see pp. 59, 74)
- [96] F. Jacobs: *Axiale Laserkühlung und Detektion für eine kryogene Penning-fallenapparatur*. Master's thesis, Leibniz Universität Hannover (2021). (see p. 74)
- [97] H. F. Powell, S. R. de Echaniz, E. S. Phillips, D. M. Segal and R. C. Thompson: *Improvement of laser cooling of ions in a Penning trap by use of the axialization technique*. *Journal of Physics B: Atomic, Molecular and Optical Physics* **36**, 961–970 (2003). doi: 10.1088/0953-4075/36/5/315 (see p. 75)

-
- [98] M. K. Joshi, P. Hrmo, V. Jarlaud, F. Oehl and R. C. Thompson: *Population dynamics in sideband cooling of trapped ions outside the Lamb-Dicke regime*. Physical Review A **99**, 013423 (2019). doi: 10.1103/PhysRevA.99.013423 (see p. 76)
- [99] M. J. Borchert: *Detektor für ein (Anti-)Proton in einer Penningfalle*. Bachelor's thesis, Leibniz Universität Hannover (2014). (see p. 77)
- [100] F. Mintert and C. Wunderlich: *Ion-Trap Quantum Logic Using Long-Wavelength Radiation*. Physical Review Letters **87**, 257904 (2001). doi: 10.1103/PhysRevLett.87.257904 (see p. 77)
- [101] Y. Colombe, D. H. Slichter, A. C. Wilson, D. Leibfried and D. J. Wineland: *Single-mode optical fiber for high-power, low-loss UV transmission*. Optics Express **22**, 19783–19793 (2014). doi: 10.1364/OE.22.019783 (see p. 85)
- [102] C. D. Marciniak, H. B. Ball, A. T.-H. Hung and M. J. Biercuk: *Towards fully commercial, UV-compatible fiber patch cords*. Optics Express **25**, 15643–15661 (2017). doi: 10.1364/OE.25.015643 (see p. 85)

Acknowledgements

The completion of this thesis would not have been possible without the support of a large number of people, whom I would like to thank at this point.

First and foremost, I would like to express my gratitude to *Christian Ospelkaus*, who supervised this thesis and trusted me to successfully meet this challenge. I appreciate that you gave me the freedom and support to implement many of my ideas and projects inside and outside the lab and that you always had an open ear for questions and problems.

I would like to extend my gratitude to *Carsten Klempt*, who accompanied me as a second supervisor during my PhD, always assisting me with advice and now acting as a referee for this thesis.

Furthermore, I would like to thank *Richard Thompson* for examining this thesis. I would have been happy to visit your research group at Imperial College if this had not been prevented at the last minute by the pandemic.

I would like to thank *Klemens Hammerer* for chairing the examination of my defense.

Stefan Ulmer and *Matthias Borchert* are thanked for their scientific advice from afar. I thank *Christian Marciniak* for showing me that there is someone sitting in a lab on the other side of the world who has the same problems as I do and for sharing his Mathematica notebook for the calculation of the transition frequencies with me.

I thank *Fritz Schulze-Wischeler* and *Oliver Kerker* for keeping the LNQE running and for always being available to help with problems.

I thank *Alexander Vocino* and *Jonas Peter*, representing the precision engineering workshop of the IQ, for producing high-quality parts from my ideas and sketches, sparing neither time nor effort.

Madeleine Miltsch and *Stephanie Kaisik*, representing the IQ secretariat, thank you for handling all my requests and questions with inexhaustible helpfulness and good humor. I would also like to thank *Birgit Ohlendorf* for her always warm and courteous support, especially during the last months of my PhD.

Special thanks go to my QLEDS mates *Teresa*, *Malte* and *Juanma*, without whom this experiment would never have become reality, and to *Julia*, who took it upon herself to lead the experiment together with *Juanma* further on the way towards quantum logic spectroscopy. Also, I would like to take this opportunity to thank all HiWis, Bachelor and Master students for their contributions to the experiment. It is only through the successful collaboration of all these people that the completion of this work was possible.

Further thanks are due to *Teresa, Kai* and *Juanma* for proofreading and commenting on this thesis.

I would also like to thank *Timko, Sebastian, Henning, Giorgio, Amado, Nico* and *Niklas* as well as all the other *Ions, SLOMOs, POMOs* and *Erik* for the many helpful discussions and social hours in the office as well as for the daily dose of insanity.

Great thanks are due to all those friends, felt family and special family members¹ who have accompanied and supported me on my way during the last years. Especially I thank the *Kochstudio* for all the beautiful moments, unforgettable trips and of course the numerous, grueling rounds of Wizard. Also the *Herde* and *Family+* deserve thanks for their mental support from afar.

I thank my parents, *Karin* and *Burkhard*, for their years of support and their firm belief that I will make it this far.

Last but not least, I thank my girlfriend *Silja* for her endless love and support, which gave me a lot of strength especially in the difficult last months of this work. Thank you for staying in the north for me, so now we can look forward together to our new home in the south!

¹ I thank my dog *Malou* for the realization that sometimes all it takes is a tear-proof blanket to tug on to forget all your worries and problems.

List of Publications

- [1] T. Meiners, M. Niemann, A.-G. Paschke, M. J. Borchert, A. Idel, J. Mielke, K. K. Voges, A. Bautista-Salvador, R. Lehnert, S. Ulmer and C. Ospelkaus: *Towards Sympathetic Laser Cooling and Detection of Single (Anti-)Protons*. Proceedings of the Seventh Meeting on CPT and Lorentz Symmetry. CPT and Lorentz Symmetry, 85–88 (2017). doi: [10.1142/9789813148505_0022](https://doi.org/10.1142/9789813148505_0022)
- [2] T. Meiners, M. Niemann, A.-G. Paschke, J. Mielke, A. Idel, M. J. Borchert, K. K. Voges, A. Bautista-Salvador, S. Ulmer and C. Ospelkaus: *Towards Quantum Logic Inspired Cooling and Detection for Single (Anti-)Protons*. Proceedings of the 12th International Conference on Low Energy Antiproton Physics (LEAP2016). JPS Conference Proceedings **18**, 011006 (2017). doi: [10.7566/JPSCP.18.011006](https://doi.org/10.7566/JPSCP.18.011006)
- [3] S. Hannig, J. Mielke, J.-A. Fenske, M. Misera, N. Beev, C. Ospelkaus and P. O. Schmidt: *A highly stable monolithic enhancement cavity for second harmonic generation in the ultraviolet*. Review of Scientific Instruments **89**, 013106 (2018). doi: [10.1063/1.5005515](https://doi.org/10.1063/1.5005515)
- [4] T. Meiners, M. Niemann, J. Mielke, M. J. Borchert, N. Pulido, J. M. Cornejo, S. Ulmer and C. Ospelkaus: *Towards sympathetic cooling of single (anti-)protons*. Proceedings of the 13th International Conference on Low Energy Antiproton Physics (LEAP 2018). Hyperfine Interactions **239**, 26 (2018). doi: [10.1007/s10751-018-1502-6](https://doi.org/10.1007/s10751-018-1502-6)
- [5] M. Niemann, T. Meiners, J. Mielke, M. J. Borchert, J. M. Cornejo, S. Ulmer and C. Ospelkaus: *Cryogenic $^9\text{Be}^+$ Penning trap for precision measurements with (anti-)protons*. Measurement Science and Technology **31**, 035003 (2019). doi: [10.1088/1361-6501/ab5722](https://doi.org/10.1088/1361-6501/ab5722)
- [6] M. Niemann, T. Meiners, J. Mielke, N. Pulido, J. Schaper, M. J. Borchert, J. M. Cornejo, A.-G. Paschke, G. Zarantonello, H. Hahn, T. Lang, C. Manzoni, M. Marangoni, G. Cerullo, U. Morgner, J.-A. Fenske, A. Bautista-Salvador, R. Lehnert, S. Ulmer and C. Ospelkaus: *Cryogenic Penning-Trap Apparatus for Precision Experiments with Sympathetically Cooled (Anti)Protons*. Proceedings of the Eighth Meeting on CPT and Lorentz Symmetry. CPT and Lorentz Symmetry, 114–117 (2020). doi: [10.1142/9789811213984_0029](https://doi.org/10.1142/9789811213984_0029)
- [7] J. M. Cornejo, R. Lehnert, M. Niemann, J. Mielke, T. Meiners, A. Bautista-Salvador, M. Schulte, D. Nitzschke, M. J. Borchert, K. Hammerer, S. Ulmer and C. Ospelkaus: *Quantum logic inspired techniques for spacetime-symmetry tests with (anti-)protons*. New Journal of Physics **23**, 073045 (2021). doi: [10.1088/1367-2630/ac136e](https://doi.org/10.1088/1367-2630/ac136e)

- [8] J. Mielke, J. Pick, J.-A. Coenders, T. Meiners, M. Niemann, J. M. Cornejo, S. Ulmer and C. Ospelkaus: *139 GHz UV phase-locked Raman laser system for thermometry and sideband cooling of ${}^9\text{Be}^+$ ions in a Penning trap*. arXiv:2106.13532v1 (2021).

Curriculum Vitae

Johannes Mielke

born November 20, 1990, in Leverkusen (Germany)

Research

10/2016 - 10/2021 **Doctoral Studies**

Leibniz Universität Hannover

PhD thesis in the group of Prof. Dr. Christian Ospelkaus

University

10/2013 - 08/2016 **Master of Science (Physics)**

Leibniz Universität Hannover

Master's thesis in the group of Prof. Dr. Christian Ospelkaus

10/2010 - 10/2013 **Bachelor of Science (Physics)**

Leibniz Universität Hannover

Bachelor's thesis in the group of Prof. Dr. Ernst M. Rasel

School

2010

Abitur

Schiller-Gymnasium Hameln